Modeling and Design of Lithium-Ion Batteries: Mechanics and Electrochemistry

by

Bin Wu

A dissertation submitted in partial fulfillment
of the requirements for the degree of
Doctor of Philosophy
(Mechanical Engineering)
in the University of Michigan
2019

Doctoral Committee:

Professor Wei Lu, Chair
Professor Jwo Pan
Professor Kang Shin
Associate Professor Donald Siegel

Bin Wu

wubin@umich.edu

ORCID iD: 0000-0002-2614-0736

© Bin Wu 2019

Dedication

To my parents

Acknowledgements

Over the past three and half years, I have received great support and warm encouragement from many individuals to complete my doctoral degree.

First, I am indebted to Professor Wei Lu, my advisor and committee chair. During my PhD study, Professor Wei Lu has given me endless support and great guidance. I really appreciate his time and efforts in teaching me, discussing with me and revising my manuscripts. His dedication to research will be an invaluable source of inspiration in my future career.

Besides my advisor, I would like to thank the rest of my committee members, Professor Kang Shin, Professor Jwo Pan and Professor Donald Siegel, for their valuable time, constructive comments and great advice.

I would like to thank my family and friends. The journey would not be possible without their love and support.

I am grateful to the financial support provided by the National Science Foundation.

Table of Contents

List of Tables

List of Figures

List of Appendices

Abstract

The active materials of lithium-ion batteries exhibit volumetric deformation during lithium intercalation and de-intercalation. Stress stemming from this volume change affects not only the durability of the batteries, but also the electrochemical processes in the electrode. This dissertation focuses on the mechanical and electrochemical modeling and design of lithium-ion batteries, ranging from particle scale to electrode scale.

Many electrode materials for lithium-ion battery applications are composed of secondary particles. Such an active material particle is not a solid particle, but consists of many fine primary particles. A mechanical and electrochemical coupled model is developed to simulate the intercalation-induced stress in a secondary particle with the agglomerate structure. In this model the electrochemical and transport processes are accounted for at both the secondary and primary particle levels. For mechanical analysis the secondary particle is treated as a continuum with stress calculated through lithium concentration and elastic deformation. Several important factors that affect stresses in secondary particles are revealed with this model.

Active particles with a core–shell structure exhibit superior physical, electrochemical, and mechanical properties over their single-component counterparts in electrodes. A physically rigorous model is developed to describe the diffusion and stress inside the core-shell structure based on a generalized chemical potential. Including both chemical and mechanical effects, the generalized chemical potential governs the diffusion in both the shell and the core. The stress is calculated using the lithium concentration profile. As revealed by the simulations, the core–shell interface is prone to debonding for particles with a thick shell, while shell fracture is more likely

to occur for particles with a large core and a relatively thin shell. Based on the simulation results, a design map of the core and shell sizes is generated to avoid both shell fracture and core-shell debonding.

As an inherent multiscale structure, a continuum scale battery electrode is composed of many microscale particles. A multiscale model is developed to couple mechanics and electrochemistry consistently at the microscopic and continuum scales. The microscopic particle stress is treated as a superposition of the intra-particle concentration gradient-induced stress and the particle interaction stress, with the latter being related to the continuum scale stress through a representative volume element. Solid diffusion and charge transfer kinetics are generalized with the mechanical effect. In a parallel effort, a direct three-dimensional particle network model is developed to serve as a standard. Comparison of results from the multiscale model and from the particle network model shows that the multiscale model gives good, satisfying accuracy with dramatically reduced computational cost.

Simulation-based battery design encounters the difficulty of high computational cost. A systematic approach based on the artificial neural network is developed to reduce the computational burden of simulation based battery design. Two neural networks are constructed using the finite element simulation results from a thermo-electrochemical model. The first neural network serves as a classifier to predict whether a set of input variables is physically feasible. The second neural network yields specific energy and specific power. With a global sensitivity analysis using the neural networks, the effects of input variables on specific energy and specific power are quantified, which is computationally prohibitive for finite element simulations. A design map is generated to fulfill the requirements of both specific energy and specific power.

Chapter 1 Introduction

1.1 Overview of Lithium-Ion Batteries

Lithium-ion batteries are widely used in applications ranging from cell phones, laptop computers to electric vehicles. As shown in Figure 1.1, the lithium-ion battery consists of a positive electrode and a negative electrode, which are separated by the separator. The electrodes are comprised of a porous composite active material layer and a metal foil current collector. The composite active material layer contains active particles, additives and binder. The typical active materials of positive electrode are lithium metal oxides, including $LiMn_2O_4$, $LiCoO_2$ and $Li(Ni_{1/3}Co_{1/3}Mn_{1/3})O_2$. For the negative electrode, the most common active material is graphite.

During charging, lithium ions extract from the active particles of the positive electrode, move across the separator and intercalate into the active particles of the negative electrode. The movement direction of lithium ions is reversed during discharging.

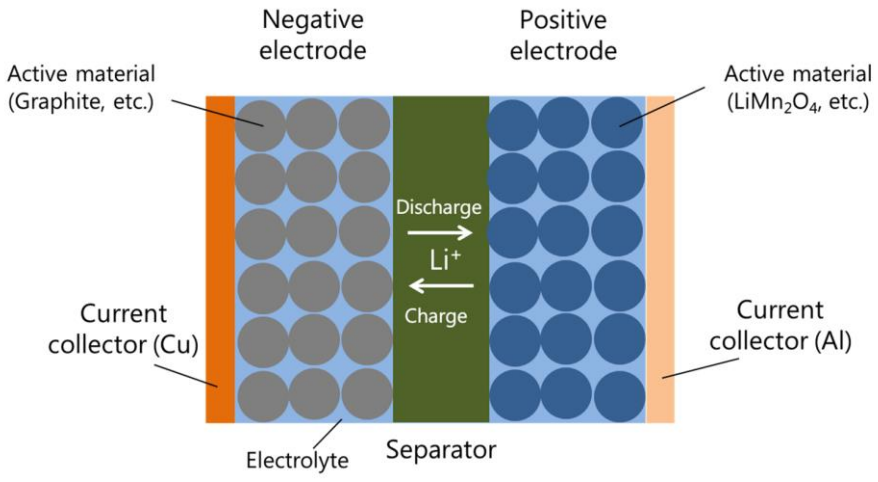

Figure 1.1. Schematic of lithium-ion battery

1.2 Mechanical Issues in Lithium-Ion Batteries

The active materials of lithium-ion battery electrodes exhibit volume change during lithium intercalation or de-intercalation. For example, a 6.5% volume change has been reported for the $LiMn_2O_4$ particle during lithiation. Owing to the relatively slow rate of solid diffusion, lithium concentration gradient develops inside particles, resulting in inhomogeneous expansion or contraction. As a result, mechanical stress develops in the particles, which is termed as diffusion-induced stress (DIS) in many works.

In addition to diffusion-induced stress due to intra-particle concentration gradient, stress also arises from particle interactions. The expansion or contraction of active particles is constrained by neighboring particles, current collectors and the battery case. This constraint can generate stress in a magnitude comparable to diffusion-induced stress [1, 2]. These stresses can lead to cracks and fractures of the electrode, such as cracks inside particles or in-between particles, causing isolation of active materials, disruption of the electrically conductive particle network and exposure of fresh surfaces for side reactions that result in capacity degradation.

Mechanical stress can change the electrochemical potential of a solid and therefore (1) affects the diffusion in the solid, and (2) affects the electrochemical reaction between the solid and the electrolyte.

For the first effect, the coupled stress and diffusion inside a single particle has been modeled by an analogy to thermal stress [3], which showed that the developed stress can enhance the solid diffusion by 35%. This approach has been extended to study many problems, such as the stress inside a nanowire [4]. The effect of active material parameters and morphology on stress has been explored [5, 6]. Researchers have investigated the fracture of a single particle [7-9] and the stress in active particles with plastic deformation [10, 11]. Consideration of stress in a

single isolated particle extends the classic electrochemical model by giving more accurate solid diffusion in a particle and allowing analysis of particle scale mechanical behaviors such as plasticity and fracture in a particle.

Stress can also affect the reaction kinetics. In a silicon particle coated by carbon shell, the lithiation-induced stress inside the silicon can halt the lithiation process [12]. The stress also affects the lithium deposition rate at the lithium metal surface, which suggests a mechanical approach to suppress the dendrite growth [13]. In a recent report [14], two identical Li-alloyed Si electrodes undergoing asymmetric bending-induced stresses create a difference in the chemical potential, and further generate an electrical current.

1.3 Goal and Outline of this Dissertation

The goal of this dissertation is to understand the mechanics, electrochemistry and their interactions in the lithium-ion batteries. The dissertation is organized as follows.

Chapter 2 focuses on a secondary particle with an agglomerate structure, which is a common morphology for many active materials like $LiNi_{0.8}Co_{0.15}Al_{0.05}O_2$ (NCA). The secondary particle, consisting of many fine primary particles, is porous rather than a compact solid, as the electrolyte is found to be soaked into the agglomerate. Therefore, charge transfer reactions are expected to occur between the primary particle surface and the electrolyte inside a secondary particle. In Chapter 2, an electrochemical and mechanical coupled model for a secondary particle is developed. With this model, several important factors that affect stress in secondary particles are revealed.

Active particles with a core-shell structure exhibit superior physical, electrochemical and mechanical properties over their single-component counterparts. For instance, cathode active particles with a $LiNi_{0.8}Co_{0.1}Mn_{0.1}O_2$ core and a $LiNi_{0.5}Mn_{0.5}O_2$ shell structure have been

synthesized, where the Ni-rich core delivers high capacity while the Mn-rich shell improves the thermal and structural stabilities. Chapter 3 develops a physically rigorous model to describe the diffusion and stress inside the core-shell structure based on a generalized chemical potential. A design map of the core and shell sizes is generated to avoid both shell fracture and core-shell debonding.

The focus of Chapter 4 is extended to the battery electrode. A lithium-ion battery electrode is an inherent multiscale structure, which consists of many active material particles together with a small amount of binder and additivity materials. An electrode can be considered a continuum since its length scale is generally one or two orders of magnitude larger than the scale of the particles. Chapter 4 presents a multiscale model that couples mechanics and electrochemistry consistently at the microscopic and continuum scales. The microscopic particle stress is a superposition of the intra-particle concentration gradient-induced stress and the particle interaction stress, with the latter being related to the continuum scale stress through a representative volume element. In a parallel effort, we develop a direct three-dimensional particle network model, which consists of realistic active material particles. Comparison of results from the multiscale model and from the particle network model shows that the multiscale model gives good, satisfying accuracy while reducing the computational cost dramatically in comparison to the three-dimensional particle network model.

Simulation-based battery design encounters the difficulty of high computational cost. Chapter 5 develops a systematic approach based on the artificial neural network to reduce the computational burden of battery design by several orders of magnitude. Two neural networks are constructed using the finite element simulation results from a thermo-electrochemical model. The first neural network serves as a classifier to predict whether a set of input variables is

physically feasible. The second neural network gives specific energy and specific power. Using the neural networks, many computationally expensive analyses can be performed with negligible computational cost.

Chapter 2 Modeling of Agglomerate Particles

2.1 Introduction

Lithium-ion batteries are widely used in applications ranging from cell phones, laptop computers to electric vehicles. Being able to provide a long cycle life is key to the lithium-ion battery technology. Mechanical degradation is one of the most significant mechanisms that affect the cycle life [15]. At the particle level, researchers have observed the formation of cracks and fractures in both cathode and anode active material particles, such as $LiCoO_2$ (LCO) [16], $LiNi_{0.8}Co_{0.15}Al_{0.05}O_2$ (NCA) [17] and graphite [18]. The cracks and fractures lead to isolation of active materials, disruption of the electrically conductive particle network and exposure of fresh surfaces that cause side reactions. These effects significantly reduce the battery capacity and increase the internal resistance. At the electrode level, X-ray computed tomography has shown evident deformation of the wounded electrode in cycled batteries [19]. The deformation increases the distance between anode and cathode, resulting in a loss of contact between the active materials and current collectors. This effect leads to an increase in electrical resistance and degradation of capacity.

Modeling and simulation are essential approaches to study the generation and effects of stress inside batteries. For instance, the volume change and stress of a spherical particle during lithium-ion intercalation has been calculated [20]. Treating the intercalation-induced stress analogously to thermal stress, a coupled mechanical and electrochemical model has been developed to study the stress and concentration inside a particle [21]. This particle level model

has been widely used and extended to study various problems at both particle and cell levels, such as to calculate the thickness change of a pouch cell during discharge [22], to study the stress generation in a LMO and NCA blended electrode [23], and to study stress generation when both intercalation and phase transition happens simultaneously in a particle [24]. Nevertheless, it should be noted that these models are based on the assumption of solid particles. This assumption does not apply for active materials with an agglomerate structure, such as NCA [17]. In these materials, many nanometer-scale primary particles agglomerate to a micrometer-scale secondary particle by the adhesion of binder. The secondary particle is porous rather than a compact solid, as the electrolyte is found to be soaked into the agglomerate [17]. Therefore, charge transfer reactions are expected to occur between the primary particle surface and the electrolyte inside a secondary particle. Active materials composed of secondary particles are becoming more common for new battery materials.

To investigate the characteristic of an agglomerate, researchers have proposed several electrochemical models to account for the effects of its internal structure. The agglomerate of $LiFePO_4$ crystals has been investigated to estimate active material utilization [25]. An electrochemical impedance model has been proposed for a secondary particle [26]. A time-domain model considering particles as agglomerates has been developed [27]. While these efforts have offered important insights into the agglomerate structure and its impact on electrochemical processes, no mechanical model has been developed to study the stress in agglomerates for lithium-ion batteries. Meanwhile, multiple experiments have reported observations of fracture of agglomerates after cycling [17], which is a major mechanism of capacity degradation. This calls for a fully understanding of the mechanical behaviors at the agglomerate level.

The objective of this chapter is to develop an electrochemical and mechanical coupled model for a secondary particle. Instead of considering it as a solid particle, we modelled a porous secondary particle by including the effects of electrochemical reactions inside the agglomerate. Our simulation results revealed that a major concentration gradient exists along the radius of the secondary particle, while the concentration is fairly uniform in each primary particle. Using the effective mechanical properties of the agglomerate, we incorporated mechanics equations into the model to capture the stress generation in the secondary particle. We identified several key factors that affect the stress level, including the primary particle size and the open circuit potential (OCP) profile. We also compared the mechanical behaviors of a porous secondary particle and a solid particle of the same size. The vast difference highlighted the importance of having a coupled electrochemical and mechanical porous model for a secondary particle.

2.2 Model Development

In our model the electrochemical part is built-up by applying the porous electrode theory at the secondary particle level [27]. We further extended the approach and incorporated the diffusion equation for primary particles to capture the holistic concentration distribution in both secondary and primary particles. The mechanical part is incorporated by integrating the concentration distribution and mechanical equations to obtain the intercalation-induced stress and displacement.

2.2.1 Electrochemical model

A secondary particle consists of fine primary particles, binders and pore space between the solids. The pore space is assumed to be filled with electrolyte. This assumption leads to the introduction of equations describing the concentration and potential distributions of electrolyte into the model.

Figure 2.1(a) shows the schematic of the model, where *R* represents the coordinate along the radius of a secondary particle and *r* represents the coordinate along the radius of a primary particle.

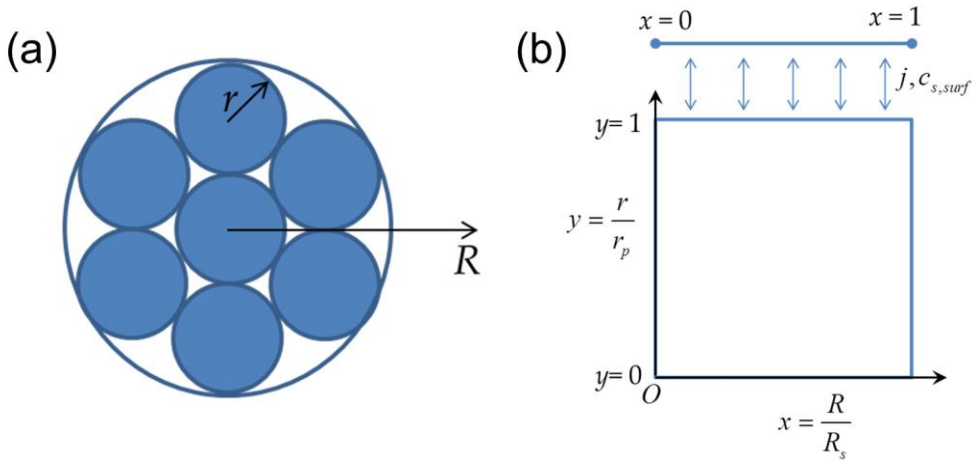

Figure 2.1. Schematic of the agglomerate structure and the dimensionless model (a) Agglomerate structure (not to scale) (b) Dimensionless model

Assumptions used in the model are listed below:

1. The secondary particle is entirely soaked in the electrolyte. The electrolyte concentration at the surface of the secondary particle is given as the boundary condition.

2. Since the size of the primary particle is much smaller than that of the secondary particle, the secondary particle is treated as the superposition of two continua: the electrolyte solution and solid primary particles. This treatment follows the basic assumption of the Newman's model [28, 29], which is widely used for porous electrodes.

3. Primary particles are assumed to be held together by binder rather than to be sintered together [26, 30]. Since lithium ions cannot diffuse across the binder, diffusion would not occur directly between two primary particles through their contacts. Diffusion can occur between two primary particles via the electrolyte.

Following the porous electrode theory, for a spherical secondary particle the electric potential in the electrolyte phase can be expressed by

$$\frac{1}{R^2}\frac{\partial}{\partial R}\left(-R^2\kappa_l\frac{\partial \Phi_l}{\partial R}+R^2\frac{2R_{\mathrm{g}}T\kappa_l}{F}(1-t_+)\frac{\partial(\ln c_l)}{\partial R}\right)=aj, \tag{2-1}$$

where R is the secondary particle coordinate, κ_l is the effective electrolyte conductivity, Φ_l is the electric potential in the electrolyte, R_{g} is the ideal gas constant, T is the absolute temperature, F is the Faraday constant, t_+ is the transference number, c_l is the electrolyte concentration, a is the active surface area per volume of the secondary particle and j is the charge transfer current density between the solid phase and the electrolyte phase. Note that $j>0$ is for lithium ion deintercalating from the solid and $j<0$ is for lithium ion intercalating into the solid.

The electric potential in the solid phase is given by

$$\frac{1}{R^2}\frac{\partial}{\partial R}\left(R^2\sigma_s\frac{\partial \Phi_s}{\partial R}\right)=aj, \tag{2-2}$$

where σ_s is the solid phase conductivity and Φ_s is the electric potential in the solid phase.

The lithium concentration in the electrolyte follows

$$\varepsilon\frac{\partial c_l}{\partial t}=\frac{1}{R^2}\frac{\partial}{\partial R}\left(R^2D_l\frac{\partial c_l}{\partial R}\right)+\frac{aj}{F}(1-t_+), \tag{2-3}$$

where ε is the porosity of the secondary particle and D_l is the effective electrolyte diffusion coefficient. Equations (2-1)~(2-3) describe the electric potential and lithium-ion concentration at the secondary particle level.

The lithium concentration in a primary particle follows the Fick's law,

$$\frac{\partial c_s}{\partial t} = \frac{1}{r^2}\frac{\partial}{\partial r}\left(D_s r^2 \frac{\partial c_s}{\partial r} \right), \tag{2-4}$$

where c_s is the lithium concentration in the solid phase, r is the primary particle coordinate, and D_s is the solid diffusion coefficient.

Now we introduce the over-potential,

$$\eta = \Phi_s - \Phi_l - E_{ref}, \tag{2-5}$$

where E_{ref} is the equilibrium potential of the active material, depending on the lithium concentration in the solid.

Combining Eqs. (2-1), (2-2) and (2-5), we have

$$\frac{\sigma_s \kappa_l}{\sigma_s + \kappa_l}\frac{1}{R^2}\frac{\partial}{\partial R}\left(R^2 \frac{\partial \eta}{\partial R} + R^2 \frac{\partial E_{ref}}{\partial R} + R^2 \frac{2R_g T}{F}(1-t_+)\frac{\partial (\ln c_l)}{\partial R} \right) = aj. \tag{2-6}$$

The charge transfer current density is given by the Butler-Volmer equation,

$$j = i_0 \left(\exp\left(\alpha_a \frac{\eta F}{R_g T} \right) - \exp\left(-\alpha_c \frac{\eta F}{R_g T} \right) \right), \tag{2-7}$$

where i_0 is the exchange current density, α_a is the anodic reaction rate coefficient and α_c is the cathodic reaction rate coefficient. The exchange current density is given by

$$i_0 = kF c_l^{\alpha_a} (c_{s,\max} - c_s)^{\alpha_a} c_s^{\alpha_c}, \tag{2-8}$$

where k is the reaction constant and $c_{s,\max}$ is the maximum lithium concentration in the solid.

The active surface area per volume, a, is related to porosity by

$$a = \frac{3}{r_p}(1-\varepsilon), \tag{2-9}$$

where r_p is the radius of the primary particle.

Dimensionless coordinates are defined as

$$x = \frac{R}{R_s}, \quad y = \frac{r}{r_p}\ , \tag{2-10}$$

where R_s is the radius of the secondary particle.

With dimensionless coordinates Eq. (2-3) is rewritten as

$$\varepsilon \frac{\partial c_l}{\partial t} = \frac{1}{x^2 R_s^2} \frac{\partial}{\partial x}\left(D_l x^2 \frac{\partial c_l}{\partial x} \right) + \frac{aj}{F}(1-t_+)\,. \tag{2-11}$$

Eq. (2-6) is rewritten as

$$\frac{\sigma_s \kappa_l}{\sigma_s + \kappa_l} \frac{1}{R_s} \frac{\partial}{\partial x}\left(\frac{\partial \eta}{\partial x} + \frac{\partial E_{ref}}{\partial x} + \frac{2R_g T}{F}(1-t_+)\frac{\partial (\ln c_l)}{\partial x} \right) = ajR_s x^2\ . \tag{2-12}$$

The gradient of the equilibrium potential is given by

$$\frac{\partial E_{ref}}{\partial x} = \frac{\partial E_{ref}}{\partial c_{s,surf}} \frac{\partial c_{s,surf}}{\partial x} = \frac{1}{c_{s,\max}} \frac{\partial E_{ref}}{\partial z} \frac{\partial c_{s,surf}}{\partial x}\ , \tag{2-13}$$

where $c_{s,surf}$ is the concentration on the surface of the primary particle and z is the stoichiometry in $Li_z MO_2$, such as $Li_z\left(Ni_{1/3}Co_{1/3}Mn_{1/3}\right)O_2$ (NCM). The term $K = \partial E_{ref} / \partial z$, known as the thermodynamic factor in this work, represents the relationship between the equilibrium potential and the lithium concentration in the solid.

The boundary conditions for Eq. (2-12) are defined as

$$\begin{aligned} &x = 0: \quad \frac{\partial c_l}{\partial x} = 0, \frac{\partial \eta}{\partial x} = 0; \\ &x = 1: \quad c_l = c_{l0}, \eta = \eta_0. \end{aligned} \tag{2-14}$$

At $x = 0$, symmetric boundary conditions are used. At $x = 1$, the electrolyte concentration and over-potential are assumed to be c_{l0} and η_0. Note that both the solid and electrolyte phases on the surface of the secondary particle carry current and they can have different potentials. This is

different from the typical constant current boundary condition prescribed on the solid phase in the Newman's porous electrode model, where current collectors exist at the boundary so that only the solid phase carries electric current to the current collector. Prescribing a constant current boundary condition on the surface of the secondary particle is complicated, which requires consideration of current in both the electrolyte and the solid phase. The typical constant potential condition at current collectors for constant potential operation does not apply here since the potential on the surface of the secondary particle is not controlled. A convenient boundary condition for the secondary particle is to prescribe the over-potential on the surface, and the the Dirichlet boundary conditions of c_{l0} and η_0 can be easily linked to a higher electrode-level model, in a way similar as the Newman's model. In the following section, the effect of η_0 on stress generation will be investigated.

With the dimensionless coordinate, diffusion in the solid primary particle is given by

$$y^2 \frac{\partial c_s}{\partial t} = \frac{1}{r_p^2} \frac{\partial}{\partial y}\left(y^2 D_s \frac{\partial c_s}{\partial y} \right). \tag{2-15}$$

The boundary conditions for Eq. (2-15) are given by

$$\begin{aligned} y=0: &\quad \frac{\partial c_s}{\partial y} = 0 \\ y=1: &\quad \frac{D_s}{r_p} \frac{\partial c_s}{\partial y} = -\frac{j}{F} \end{aligned} \tag{2-16}$$

Figure 2.1(b) shows the schematic of the dimensionless model. Equations at the primary particle level (Eqs. (2-15) and (2-16)) and at the secondary particle level (Eqs. (2-7), (2-11), (2-12) and (2-14)) are coupled through the charge transfer current density j and surface solid concentration $c_{s,surf}$. The concentration and electric potential fields are obtained by solving the coupled equations with their boundary conditions.

Figure 2.2 shows a representative result that gives the lithium concentration inside each primary particle along the radial direction of the secondary particle. The *x* axis represents the location of a primary particle inside the secondary particle, while the *y* axis represents the location of a spatial point inside the primary particle. As shown in Figure 2.2, the primary particle shows a fairly uniform concentration. A major concentration gradient exists along the radius of the secondary particle, which is attributed to the spatial variation of the charge transfer current density to be discussed in Section 0.

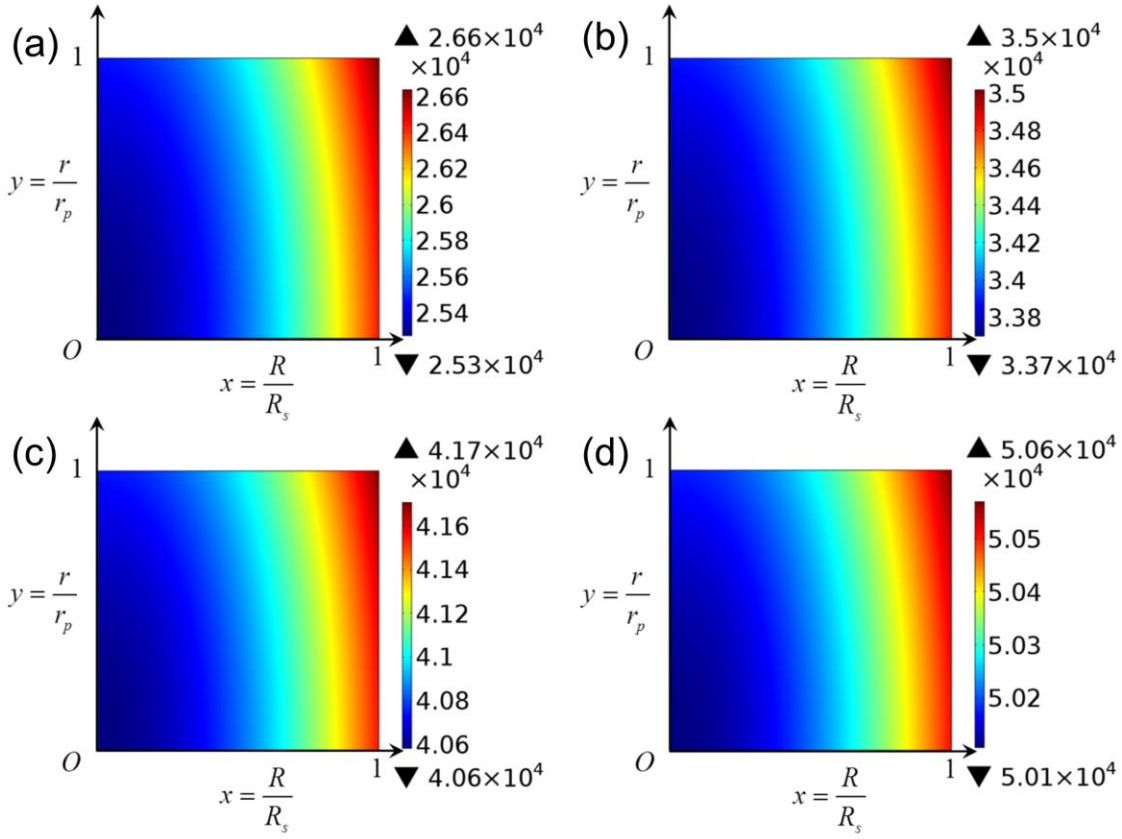

Figure 2.2. Lithium concentration distribution in primary particles at four selected times: (a) 27 s, (b) 54 s, (c) 82 s and (d) 135 s. The unit of concentration is mol/m^3. For all these simulation results, $\eta_0 = -10\,\text{mV}$ and $K = -0.5\,\text{V}$.

2.2.2 Mechanical model

Simulation results from the electrochemical model revealed concentration gradient along the radius of the secondary particle. A mechanical model is developed to evaluate the stress. Assumptions used in the mechanical model are listed below:

1. The secondary particle is assumed to be mechanically homogeneous with effective properties, which can be calculated from the porosity and properties of bulk materials.

2. Because the primary particle is much smaller than the secondary particle, the secondary particle is regarded as a continuum. Each spatial point in the secondary particle is composed of many primary particles at that location. Therefore the stress at each spatial point represents the loading stress exerted on the primary particles at that location. This loading stress is important to know since it is the cause of separation of primary particles, i.e. fracture in the secondary particle.

The effective Young's modulus, E, and Poisson's ratio, ν, of a porous microstructure can be expressed as [31]

$$\frac{E}{E_b}=\left(1-\frac{\varepsilon}{\varepsilon_0}\right)^n, \nu=\nu_0+\left(1-\frac{\varepsilon}{\varepsilon_1}\right)^m(\nu_b-\nu_0), \tag{2-17}$$

where E_b and ν_b are bulk Young's modulus and Poisson's ratio of the solid, $\varepsilon_0, \varepsilon_1, n, m$ and ν_0 are fitted parameters obtained from the finite element simulation results of porous microstructures. The suggested values are $\varepsilon_0=0.652$, $n=2.23$, $\varepsilon_1=0.500$, $m=1.22$ and $\nu_0=0.140$ for the porous structure consisting of overlapping solid spheres [31].

The equilibrium equation in the secondary particle is given by

$$\frac{d\sigma_r}{dR}+\frac{2}{R}(\sigma_r-\sigma_t)=0, \tag{2-18}$$

where σ_r is the radial stress and σ_t is the tangential stress. The stress-strain relations are

$$\varepsilon_r = \frac{1}{E}(\sigma_r - 2\nu\sigma_t) + \frac{\Omega}{3}\tilde{c}, \tag{2-19}$$

$$\varepsilon_t = \frac{1}{E}\left[\sigma_t - \nu(\sigma_r + \sigma_t)\right] + \frac{\Omega}{3}\tilde{c} \tag{2-20}$$

where Ω is the partial molar volume of lithium ion and $\tilde{c}(R) = c_{s,surf}(R) - c_{s0}$ is the change of surface concentration of the primary particle located at position *R* in the secondary particle. c_{s0}, the initial lithium concentration, is defined in Table I.

Take u as the radial displacement. The strains can be expressed by

$$\varepsilon_r = \frac{du}{dR},\ \varepsilon_t = \frac{u}{R}. \tag{2-21}$$

Equations (2-18)-(2-21) can be solved by combining them into a displacement equation [21]. With the boundary condition of $\sigma_r(R = R_s) = 0$, the stress and displacement in the secondary particle are given by

$$\sigma_r = \frac{2\Omega E}{3(1-\nu)}\left(\frac{1}{R_s^3}\int_0^{R_s}\tilde{c}r^2 dr - \frac{1}{R^3}\int_0^{R}\tilde{c}r^2 dr\right), \tag{2-22}$$

$$\sigma_t = \frac{\Omega E}{3(1-\nu)}\left(\frac{2}{R_s^3}\int_0^{R_s}\tilde{c}r^2 dr + \frac{1}{R^3}\int_0^{R}\tilde{c}r^2 dr - \tilde{c}\right), \tag{2-23}$$

$$u = \frac{R\Omega}{3}\left[\frac{2(1-2\nu)}{(1-\nu)}\frac{1}{R_s^3}\int_0^{R_s}\tilde{c}r^2 dr + \frac{(1+\nu)}{(1-\nu)}\frac{1}{R^3}\int_0^{R}\tilde{c}r^2 dr\right], \tag{2-24}$$

In Eqs. (2-22) and (2-23) tensile stress is positive while compressive stress is negative.

Special attention should be given at $R=0$ for Eqs. (2-22)-(2-24) as they include the term $\frac{1}{R^3}\int_0^R \tilde{c}r^2 dr$,where *R* appears in the denominator. We shall use L'Hôpital's rule at $R=0$, which gives

$$\lim_{R\to 0}\frac{1}{R^3}\int_0^R \tilde{c}r^2 dr = \frac{\tilde{c}(R=0)}{3} \quad . \tag{2-25}$$

The calculated stress in the secondary particle can be comparted to the continuum material properties of the secondary particle to determine fracturing which is related to separation between primary particles, or yielding which is related to sliding between primary particles. It should be noted that the stress concentration occurs at the contact points between particles [1], while our model gives the homogenized stress at any spatial point. To capture the local contact stress between primary particles, one can explicitly model an ensemble of primary particles and their geometries using finite element, and apply Eqs. (2-22) and (2-23) as the boundary conditions of the ensemble. This bridging of scales allows analyzing various local mechanical behaviors between primary particles.

2.2.3 Parameters

Table 2.1 lists the parameters used in the model, which are applicable to an agglomerate of NCM. The mechanical properties of NCM are rarely given in the literature, so the values of LMO are used which are in the similar range.

Two concentration dependent parameters, κ_l and D_l , are assumed as constant for simplicity. This assumption is acceptable considering the small scale of agglomerate and therefore small variation in electrolyte lithium concentration. In addition, κ_l and D_l listed in

Table 2.1 are calculated from the intrinsic values of electrolyte and porosity of the secondary particle using the Bruggeman correlation, where the tortuosity τ is assumed as $\varepsilon^{-0.5}$.

Table 2.1. Parameters used in the model.

Parameter	**Symbol**	**Value**	**Reference**
Primary particle radius	r_p	0.2 μm	[17]
Secondary particle radius	R_s	10 μm	[17]
Porosity of the secondary particle	ε	25%	[32]
Solid conductivity	σ_s	0.12 S/m	[27]
Solid diffusion coefficient	D_s	1×10^{-14} m^2/s	[27]
Electrolyte conductivity	κ_l	0.0975 S/m	[27]
Electrolyte diffusion coefficient	D_l	1.85×10^{-11} m^2/s	[27]
Initial electrolyte concentration	c_{l0}	1000 mol/m^3	[27]
Maximum solid concentration	$c_{s,max}$	51830 mol/m^3	[33]
Initial solid concentration	c_{s0}	$0.36c_{s,max}$	[33]
Reaction constant	k	6.15×10^{-11} $m^{2.5}$ $mol^{0.5}$ s^{-1}	[34]
Transference number	t_+	0.38	[27]
Temperature	T	298 K	[27]
Anodic reaction rate coefficient	α_a	0.5	[35]
Cathodic reaction rate coefficient	α_c	0.5	[35]
Bulk Young's modulus	E_b	100 GPa	[36]
Bulk Poisson's ratio	ν_b	0.24	[37]
Partial molar volume	Ω	3.497×10^{-6} m^3/mol	[21]

Although the electrical conductivity of the electrode can be found in the literature [38], the conductivity of the agglomerate itself is still not clear. As the conductive additive mainly enhances the electrical conductivity at the electrode level rather than at the agglomerate level, it has been suggested that the electrical conductivity of the NCM agglomerate accounts for only

0.1% of that of the cathode [27]. We adopted this suggested value of electrical conductivity for the agglomerate.

The model was implemented using the finite element software package COMSOL Multiphysics.

2.3 Results and Discussions

Figure 2.3(a) and (b) show the radial and tangential stresses in the secondary particle at five selected times. With the intercalation of lithium ions, the expansion of the particle results in tensile radial stress. Due to the strain differential between the outer and inner regions of the particle, the tangential stress is compressive at the surface while tensile at the center. As indicated in Eqs. (2-22) and (2-23), a larger concentration gradient in the secondary particle leads to a large stress. In Figure 2.3(a) and (b), both stresses increase during the period of 0 s to 27 s and then decrease, suggesting that the concentration gradient reaches its maximum at around 27 s. This is supported by the concentration distribution shown in Figure 2.2. As lithium ions cannot diffuse directly across primary particles, the current density at the primary particle surface is the predominant factor that determines the concentration inside the primary particle. Hence, the lithium concentration gradient in the solid phase of the secondary particle stems from the variation in surface current density of primary particles. Figure 2.3(c) shows that the originally non-uniform current density becomes uniform after 27 s, which is consistent with the evolution of concentration gradient. Another note taken from Figure 2.3(c) is that the rate of lithium intercalation, $|j|$, decreases after 27 s. Therefore, the concentration gradient inside a primary particle built up before 27 s has an opportunity to be gradually smoothened. The shape of current density curves can be explained by the exchange current density and the over-potential, as shown in Figure 2.3(d) and (e).

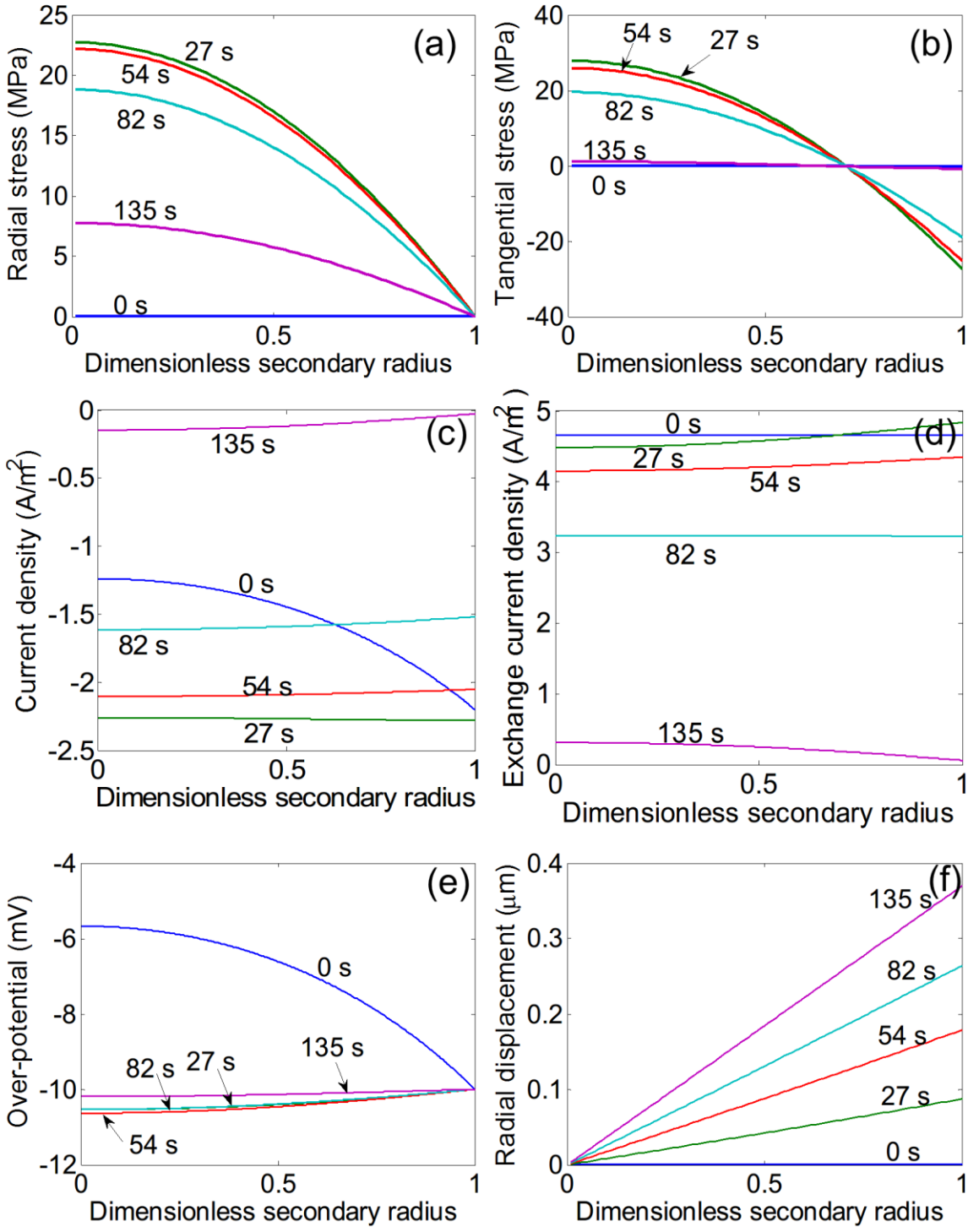

Figure 2.3. Stress, current density, over-potential and radial displacement along the radius of the secondary particle at five selected time. (a) Radial stress. (b) Tangential stress. (c) Current density. (d) Exchange current density. (e) Over-potential. (f) Radial displacement. For all these simulation results, $\eta_0 = -10\ \mathrm{mV}$ and $K = -0.5\ \mathrm{V}$.

The exchange current density at the surface of the secondary particle is slightly larger than that at the center in the beginning, because the electrolyte concentration keeps constant at the surface while the lithium ions in electrolyte is consumed at the center of the secondary particle. As the primary particles at the outer region gradually become saturated with intercalated lithium ions, the exchange current at the center slightly surpasses the exchange current at the surface after 82 s. In addition, Figure 2.3(d) shows that the exchange current density pronouncedly decreases with time, as the primary particles are gradually intercalated to full. This trend explains the decrease in the intercalation rate $|j|$, as shown in Figure 2.3(c).

Initially, the spatial variation of exchange current is much smaller than that of current density, implying that over-potential plays a significant role in determining the distribution of current density. Figure 2.3(e) shows that the distribution of over-potential is non-uniform at 0 s but approaches uniform at later times. The transition of over-potential distribution can be elaborated through two negative feedback mechanisms. Note that the over-potential is fixed at the surface of the secondary particle.

In the first mechanism, a decrease of η (meaning an increase of $|\eta|$ since $\eta<0$) leads to an increase of the lithium intercalation rate $|j|$, which further results in a faster increase of c_s and thus a faster decrease of E_{ref}. As E_{ref} is always positive and appears as an additive term next to η in Eq.(2-12), the faster decrease of E_{ref} finally leads to an increase of η. We regard this negative feedback as the thermodynamic feedback due to the role played by E_{ref}. A strong dependence of E_{ref} on c_s causes significant contribution of the thermodynamic feedback, which will be discussed in the following section.

In the second mechanism, a decrease of η results in a faster increase of c_s, consequently leading to a decrease of i_0 and $|j|$. As the intercalation current is the source term in Eq.(2-12), the decrease of $|j|$ (meaning an increase of j since $j<0$) finally contributes to the increase of η. We regard this negative feedback as the kinetic feedback owing to the interplay between η and $|j|$.

Figure 2.3(f) shows the radial displacement in the secondary particle at five selected times. The displacement is almost linear along the radius of the secondary particle, and the displacement at the surface is the largest. It should be noted that the maximum radial displacement is nearly 0.36 μm, which only accounts for 3.6% of the radius of the second particle. The calculated radial displacement at the secondary particle surface can serve as an input to an electrode-level model to calculate the electrode thickness change during discharge.

Maximum stresses are important to evaluate the mechanical integrity of the secondary particle. The maximum radial stress and the maximum tensile tangential stress are equal and are located at the center of the secondary particle,

$$\sigma_{r,\max}=\sigma_{t,\max}=\frac{2\Omega E}{3(1-\nu)}\left(\frac{1}{R_s^3}\int_0^{R_s}\tilde{c}r^2dr-\frac{\tilde{c}(R=0)}{3}\right). \tag{2-26}$$

The maximum compressive tangential stress is located at the surface,

$$\sigma_{t,\min}=\frac{\Omega E}{3(1-\nu)}\left(\frac{3}{R_s^3}\int_0^{R_s}\tilde{c}r^2dr-\tilde{c}(R=R_s)\right), \tag{2-27}$$

where the subscript "min" is used since the compressive stress is negative.

Figure 2.4 shows that the peaks of $\sigma_{r,\max}$, $\sigma_{t,\max}$ and $|\sigma_{t,\min}|$ are reached at around 27 s, a time when the spatial distribution of current density along the secondary particle radius becomes

uniform. . Literature has shown that in a solid particle $|\sigma_{t,\min}|$ should be greater than $\sigma_{r,\max}$ and $\sigma_{t,\max}$ under a constant rate of lithium ion intercalation [23]. In contrast, the results in Figure 2.4 show that $|\sigma_{t,\min}|$ is not always larger than $\sigma_{r,\max}$ and $\sigma_{t,\max}$ for a porous secondary particle. This difference in the characteristics of maximum stress can be explained by the differences in governing equations and boundary conditions. Previous literature is based on the governing equation of diffusion in a solid particle with a constant Neamann boundary condition at the surface [23]. This work modeled the electrolyte phase in a porous secondary particle and adopted the Dirichlet boundary condition at the surface of the secondary particle.

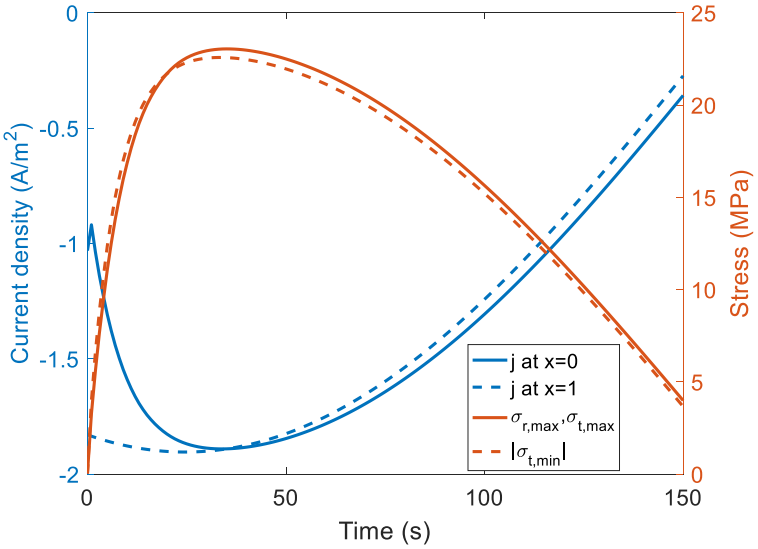

Figure 2.4. Maximum tensile stress, maximum compressive stress and current density with respect to time. As the compressive stress is negative, the absolute value of the compressive tangential stress is plotted. The maximum radial stress always equals to the maximum tangential tensile stress.

2.3.1 Thermodynamic factor

In this section, we examine the effect of thermodynamic factor *K* on the stress generation behavior. The thermodynamic factor is defined as the dependence of OCP on the stoichiometry of the active material in Section 2.2.1. Figure 2.5 shows the stress and concentration distributions

for K = -1 V and K = 0 V at the instant when the maximum radial stress peaks. A larger magnitude of K represents a stronger effect of the thermodynamic feedback mechanism, leading to more uniform concentration distribution and smaller stresses. This is supported by the comparison of the two cases shown in Figure 2.5.

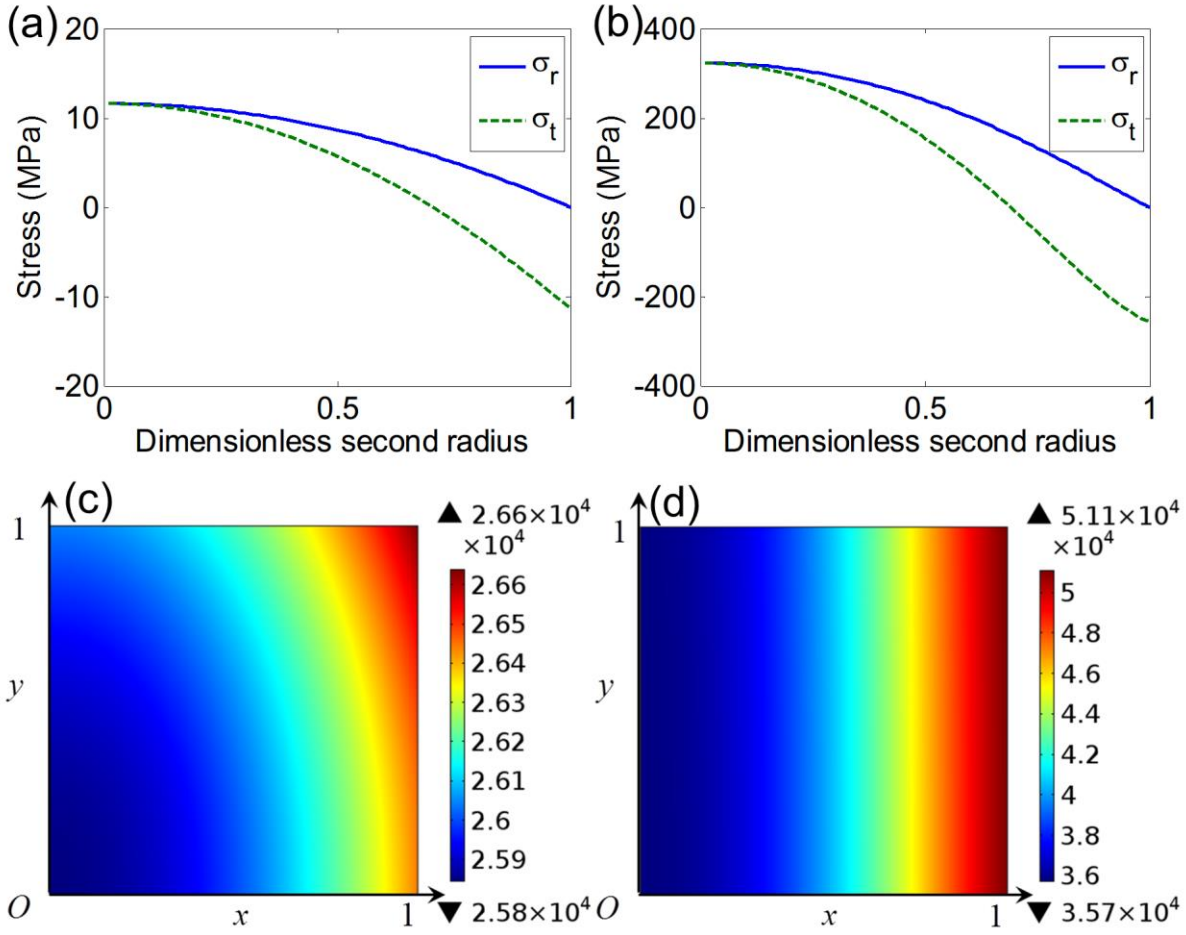

Figure 2.5. Stress and concentration distributions for different thermodynamic factors. For (a) and (c), K = -1 V. For (b) and (d), K = 0 V. The presented time is at the instant when the radial stress at the center reaches its maximum. The unit of concentration is mol/m^3 in (c) and (d).

Figure 2.6 shows the distribution of current density and over-potential for K = 0 V at the same selected times as those in Figure 2.3. As K = 0 V represents the special case of no thermodynamic negative feedback, both the current density and over-potential show large variation along the radius of the second particle at 135 s. The large spatial variation in current

density directly results in a large concentration gradient along the radius of the secondary particle, as shown in Figure 2.5(d). The magnitude of current density at the center surpasses the current density at the surface at 135 s, which is a result of heavy depletion of available lithium intercalation sites at the surface during 0~82 s. The reverse in the current density distribution is ascribed to the kinetic negative feedback. However, this reverse occurs near the end of discharge, leaving a still large concentration gradient.

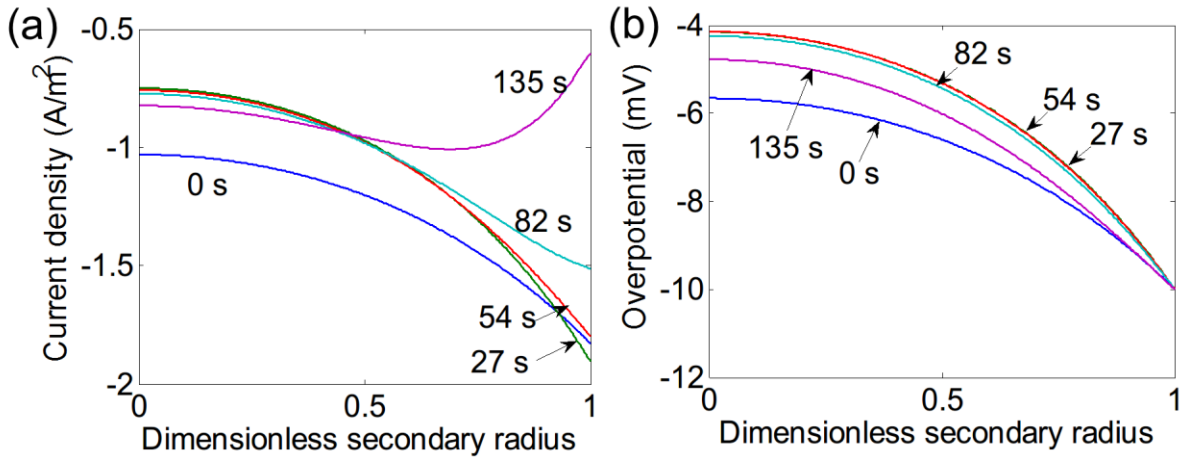

Figure 2.6. The distribution of (a) current density and (b) over-potential at five selected times. For the simulation results, $\eta_0 = -10\ \mathrm{mV}$ and $K = 0\ \mathrm{V}$.

The value of *K* can be determined from the OCP-*z* profile, which is shown in Figure 2.7(a). Figure 2.7(b) illustrates the temporal evolution of $\sigma_{r,\max}$, $\sigma_{t,\max}$ and $\left|\sigma_{t,\min}\right|$ using the OCP-z profile shown in Figure 2.7(a). Previous discussion concludes that small magnitude of *K* results in non-uniform current density and thus large stress. This is further shown in Figure 2.7(b), where the stresses and thermodynamic factor demonstrate similar trends with respect to time. The different values of *K* at different regimes of state of charge result in the change of stress over the course of intercalation or deintercalation, which may result in fatigue and reduced strength of the secondary particle.

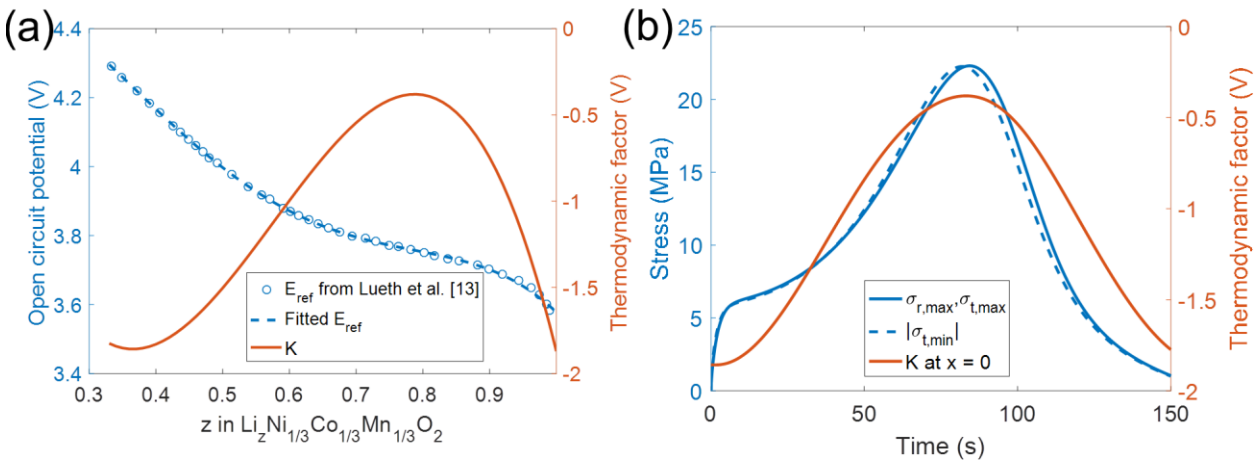

Figure 2.7. (a) Open circuit potential (E_{ref}) and thermodynamic factor (K) with respect to the stoichiometry in $\mathrm{Li}_z\left(\mathrm{Ni}_{1/3}\mathrm{Co}_{1/3}\mathrm{Mn}_{1/3}\right)\mathrm{O}_2$. (b) Simulated stress using the open circuit potential profile in (a). For the simulation results, $\eta_0 = -10\ \mathrm{mV}$

2.3.2 Over-potential

The electrochemical model uses a given over-potential η_0 at the surface of the secondary particle. This treatment can be easily linked to an electrode-level model, where the over-potential at any spatial point across the electrode thickness can be calculated and coupled to the particle level model. Figure 2.8 shows that the maximum radial stress increases almost linearly with the magnitude of η_0. A larger $|\eta_0|$ not only causes a larger intercalation rate $|j|$, but also a non-uniform distribution of intercalation rate along the radius of the secondary particle. It is this non-uniform intercalation rate that results significant stress, as discussed previously.

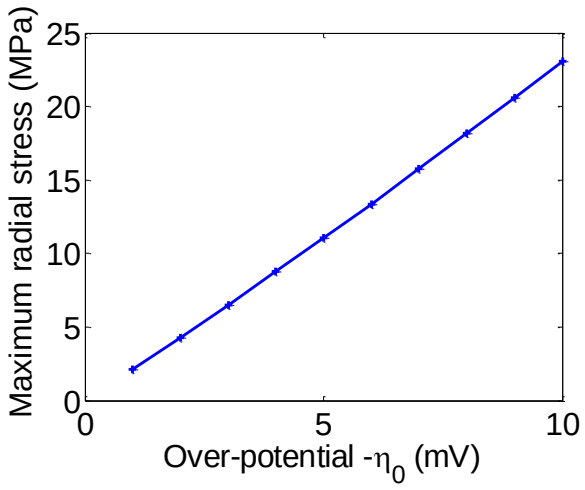

Figure 2.8. Maximum radial stress increases with the magnitude of over-potential

Previous studies have investigated the maximum radial stress for a solid particle under different discharge rates. [20, 21] These results showed that the maximum radial stress firstly increases but then decreases with the current density. The latter decrease in stress results from the fact that the concentration gradient is still undeveloped at the end of discharge under a large discharge current. In contrast, Figure 2.8 shows only an increase of the maximum stress with the magnitude of over-potential, which is positively correlated with the current density. This feature comes from the characteristic of the porous secondary particle model. The distribution of current density determines the concentration gradient along the radius of the secondary particle. The current density gradient is established immediately at the beginning of discharge, as there is no time-derivative term in Eq. (2-12). Hence, a large concentration gradient can still develop before the end of discharge even when a large magnitude of over-potential is used as the boundary condition.

2.3.3 Primary particle size

Figure 2.9 shows the effect of primary particle size on the maximum radial stress during intercalation. Interestingly, a smaller primary particle size leads to a larger maximum radial

stress. This is understandable when considering the role of the active surface area per volume. As defined in Eq. (2-9), the active surface area per volume decreases with the radius of the primary particle. This variable appears before the current density j as the source term in Eq. (2-6). A large active surface area per volume amplifies the spatial variation in current density, leading to larger concentration gradient and stress. Thus, the peak of maximum radial stress decreases with the increase of the primary particle size.

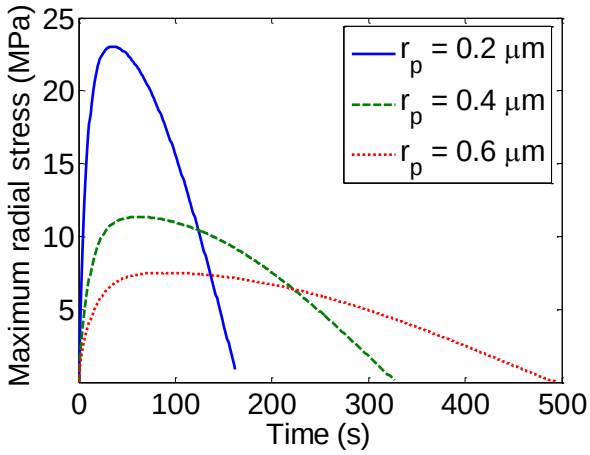

Figure 2.9. Maximum radial stress as a function of time for three different primary particle radii

Figure 2.10 compares the current density at the center (x = 0) and at the surface (x = 1) of the secondary particle with different size of primary particles. The current density difference between the center and the surface in Figure 2.10(a) is larger than that in Figure 2.10(b), demonstrating the effect of the active surface area per volume.

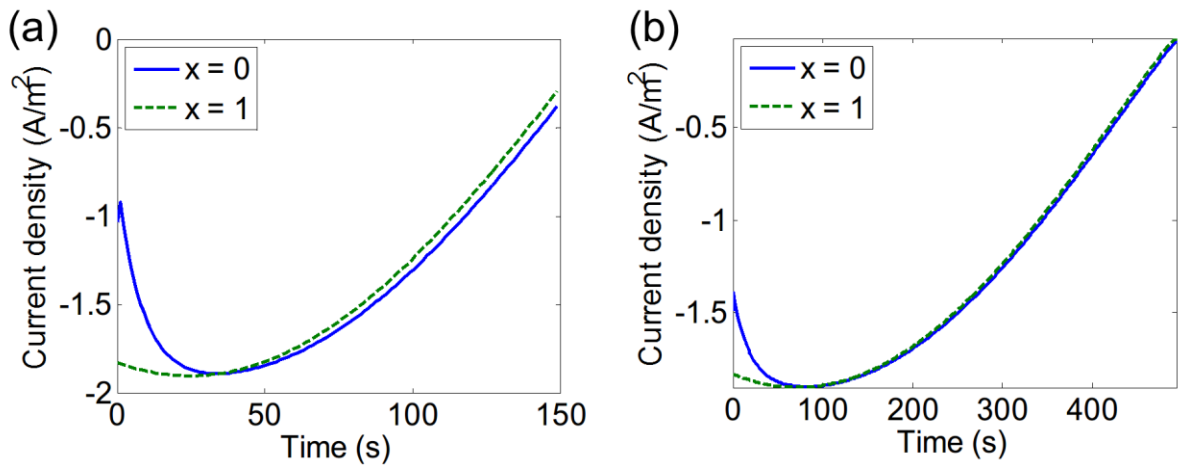

Figure 2.10. Current density evolution at the center ($x=0$) and surface ($x=1$) of the secondary particle for (a) $r_p=0.2\ \mu\text{m}$ and (b) $r_p=0.6\ \mu\text{m}$.

The effect of diffusion inside the primary particle becomes more important with the increase of the primary particle size. Figure 2.11 demonstrates the concentration distribution of the agglomerate at the time when the maximum radial stress reaches its peak. With larger primary particle sizes, the concentrations in the primary particles become more non-uniform. This concentration gradient in a primary particle can induce an additional stress inside the primary particle. As shown in Figure 2.11(b), the assumption that the stress inside the primary particles is negligible becomes invalid as the particle radius turns to 0.6 μm. However, it should be noted that this additional stress has little effect on the interaction between particles since it is internal, while the calculated stress at the secondary particle level affects the interaction between primary particles significantly. Fracture often happens between primary particles due to their weak bonding. The stress at the secondary particle level is important in determining the fracture of an agglomerate.

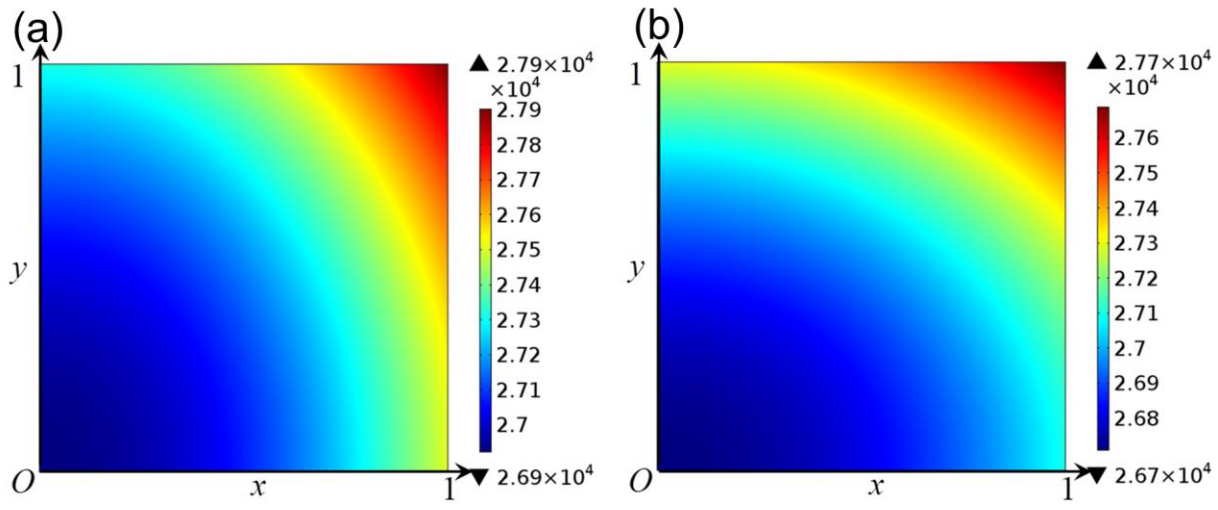

Figure 2.11. Concentration distribution at the time when maximum radial stress reaches its peak for (a) $r_p = 0.4\ \mu\text{m}$ and (b) $r_p = 0.6\ \mu\text{m}$. The unit of concentration is mol/m^3.

2.3.4 Comparison with a solid particle of the same size

The stresses in a porous secondary particle and in a solid particle of the same size are compared in Figure 2.12. The stress in a solid particle is much larger than that in a porous secondary particle, which can be attributed to two reasons. First, the Young's modulus of the solid particle (100 GPa) is nearly three times as large as that of a porous secondary particle (34 GPa). As shown in Eqs. (2-22) and (2-23), the stress is proportional to the Young's modulus, leading to three times larger stress in the solid particle. Second, and more importantly, the concentration gradient in the porous secondary particle is much smaller than that in the solid particle. The electrolyte inside the porous secondary particle provides a fast diffusion path for lithium ions, which greatly reduces the concentration gradient. Note that the current density at the surface of the solid particle shown in Figure 2.13 is close to the current density at the surface of the primary particle surface shown in Figure 2.3(c), suggesting that the pronounced difference in stress is not from the difference in current density.

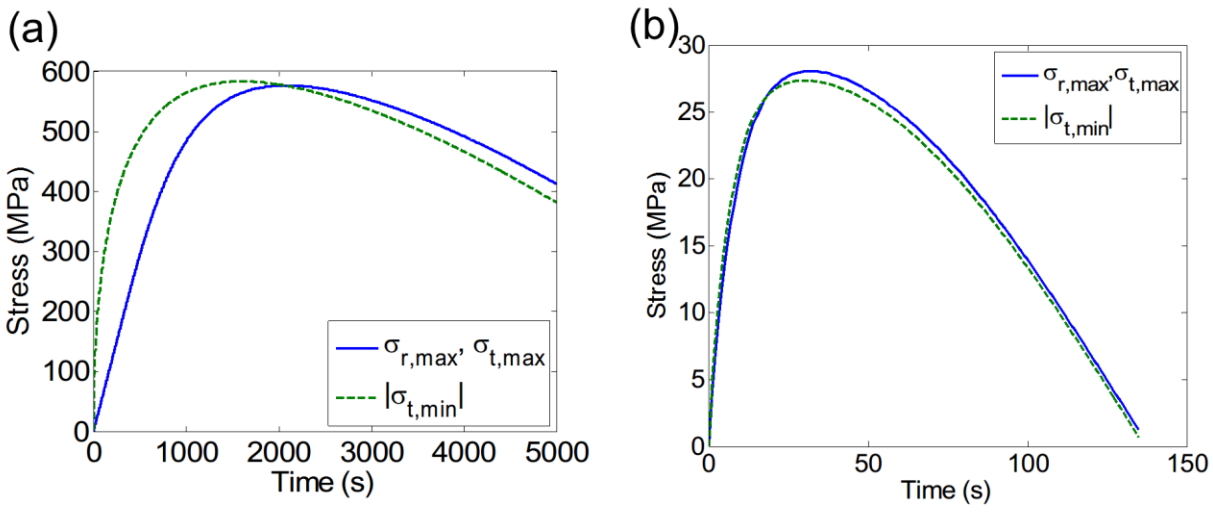

Figure 2.12. Maximum stresses of (a) a solid particle and (b) a porous secondary particle. For these simulation results, $\eta_0 = -10\ \mathrm{mV}$.

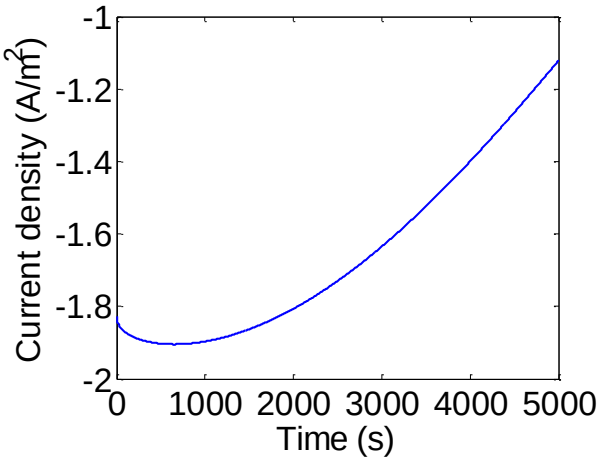

Figure 2.13. Current density at the surface of the solid particle

2.4 Conclusion

In this chapter, an electrochemical and mechanical coupled model is developed to calculate the stress generation in a secondary particle consisting of many primary particles. As the electrolyte fills the pore between primary particles, charge transfer reactions are assumed to take place inside the secondary particle, leading to the introduction of governing equations for electrolyte concentration and electrolyte potential. Simulation results reveal that a major concentration gradient exists along the radius of the secondary particle, while the concentration

distribution in each primary particle is fairly uniform. Based on this finding, the mechanical model focused on the stress generation at the secondary particle level. Assuming the secondary particle a continuum, the intercalation-induced stress is calculated using elastic equations.

We have applied the developed model to investigate factors affecting the stress generation behaviors. The results are summarized as follows: 1) A strong dependence of OCP on the solid lithium concentration leads to a more uniform current density in the secondary particle, which reduces the stress level. 2) A large magnitude of over-potential at the secondary particle surface causes severely non-uniform current density, and thus larger stresses. 3) The primary particle size shows a significant effect on the current density, concentration and stress profiles. A larger primary particle size results in a smaller active surface area per volume, which reduces the impact of non-uniform current density and thus reduces the stress level in the secondary particle. However, the concentration gradient inside the primary particle becomes pronounced with the increase of the primary particle size, which may generate stress inside the primary particle. 4) The comparison between a porous secondary particle and a solid particle of the same size shows that the stress is greatly alleviated in the porous secondary particle. This is attributed to the lower Young's modulus of the porous particle, and more importantly, to the smaller concentration gradient in the porous secondary particle.

In this chapter we treat the secondary particle as a continuum in the stress calculation. The stress at each spatial point represents the loading stress exerted on the primary particles at that location. This loading stress can lead to fracture in the secondary particle in terms of separation of primary particles. We plan to study this fracture behavior in future work by applying the stress predicted by this model as the loading boundary conditions on a representative volume of the particle network. In addition, the model proposed in this work can

be incorporated into a cell level mechanical model to provide valuable insights into the overall battery degradation.

Chapter 3 Modeling of Particles with Active Core-Shell Structure

3.1 Introduction

The growing demand for higher energy density and power density, longer cycle life and lower cost of lithium ion batteries has driven significant progress in battery materials research. Besides searching for new materials, engineering of material structure is equally important to fully exploit the potential of existing or new materials. Core-shell structure is an effective strategy to combine the advantages and avoid the disadvantages of two materials [39]. For example, cathode active particles with a $LiNi_{0.8}Co_{0.1}Mn_{0.1}O_2$ core and a $LiNi_{0.5}Mn_{0.5}O_2$ shell structure have been synthesized [40, 41], where the Ni-rich core delivers high capacity while the Mn-rich shell improves the thermal and structural stabilities. The core-shell structure has also been used for anode materials. The silicon particle, which has a high theoretical capacity, suffers from dramatic volume change during lithiation/de-lithiation processes. Researchers have proposed to coat a layer of carbon[42] or silicon oxide[43] to restrict the volume change of silicon, thus to improve the cycle life. In addition to these purposely designed core-shell structures, passively formed core-shell structures can also be found in battery materials, such as the solid electrolyte interface (SEI) film forming at the surface of an active particle. Overall, in a core-shell structure the shell can (1) protect the core from environmental corrosion or side reactions, such as the SEI film on the surface of a graphite particle [44], (2) enhance physical or chemical properties, such as the carbon shell outside a Mn_2O_4 core to improve the conductivity

[45], or (3) restrict the volume change of the core to maintain structural integrity, such as the carbon shell outside a silicon core [46].

Stress generation associated with solid diffusion has been widely discussed in the literature. Researchers have investigated the mechanical and electrochemical behaviors of a single particle with a three-dimensional morphology [21] and a secondary particle with an agglomerate structure [47]. The developed stress inside the particle brings two effects. The first effect is the influence of stress on degradation in the core-shell structure. For the core-shell structure, the resulting stress from the lithium diffusion may lead to fracture of the shell or debonding between the core and the shell. For instance, a large void has been observed to form at the interface of the $LiNi_{0.8}Co_{0.1}Mn_{0.1}O_2$ core and the $LiNi_{0.5}Mn_{0.5}O_2$ shell after long-term cycling, owing to the structural mismatch and the difference in volume change between the core and the shell [48]. Similarly, the expansion of lithiated graphite core can lead to fracture of the SEI film, which further causes solvent de-composition and capacity degradation [49].

The second effect is the influence of stress on electrochemistry in the core-shell structure. Mechanical stress can change the electrochemical potential of solids, and therefore affects the diffusion [21] or lithiation processes [12, 50] inside the particle. For example, the developed stress gradient inside a $LiMn_2O_4$ particle is predicted to increase the effective solid diffusivity by up to 35% [21]. Calculations have shown that the pressure generated from the shell can halt the lithiation process inside the core [12]. The plastic deformation of amorphous silicon accounts for a significant percentage of the energy dissipated during the cycling at low C-rates [51].

Modeling the core-shell structure has attracted significant attention recently [12, 44, 45, 49, 50, 52]. However, current models typically treat the shell as mechanical constraint only without any electrochemical activity [12, 49, 52]. In this treatment, the lithium ions directly

insert into or extract from the core without moving across the shell, which is not consistent with physical reality. In one work [45], although the diffusion through the carbon shell is modeled, the associated expansion inside the shell is neglected. Moreover, the assumption that the lithium concentration is continuous through the core-shell interface often cannot be satisfied, since the core and shell are two phases with distinct affinity for the lithium. Physically, a more natural way to tackle the diffusion in multiple phases is to use the chemical potential instead of the concentration. As mechanical stress resulting from concentration gradient can affect the chemical potential, modeling the core-shell structure requires fully coupling mechanics and electrochemistry.

In this work, we develop a physically rigorous model to describe lithium diffusion and the resulting stress generation inside a particle with a core-shell structure. The generated stress and its effect on debonding between the core and the shell or shell fracture are correlated to the design parameters of the core-shell structure. Using the energy release rate, a design map is developed to guide the synthesis and application of the core-shell structure.

3.2 Model Development

Figure 3.1 shows the schematic of the model, where phase 1 denotes the core with a radius of a and phase 2 denotes the shell with an outer radius of b. Both the core and the shell are electrochemically active for lithiation and de-lithation, and both undergo volume change.

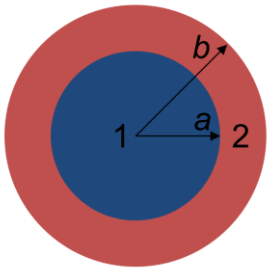

Figure 3.1. A schematic of the core-shell structure

3.2.1 Electrochemistry

The lithium concentration in the particle, *c*, either in the core or in the shell, is governed by

$$\frac{\partial c}{\partial t} + \nabla \cdot \mathbf{J} = 0. \tag{3-1}$$

The flux of lithium ions, $\mathbf{J}$, is given by [53]

$$\mathbf{J} = -Mc\nabla\mu, \tag{3-2}$$

where M is the lithium mobility in the solid, and μ is the chemical potential of lithium in the active particle. A rigid definition of $\mathbf{J}$ and μ can be found in the Appendix A.

Taking into account the effect of mechanical stress, the chemical potential of lithium ion in the active particle is given by

$$\mu = \mu_c + \mu_m, \tag{3-3}$$

where μ_c denotes the chemical potential at the stress-free state and μ_m denotes the effect of mechanical stress on the chemical potential.

The expression of μ_m has been discussed in several works [54-57]. Under the assumption of small linear elastic deformation and no dependence of mechanical properties on lithium fraction, Eq. (3-3) can be written as [21]

$$\mu = \mu_c - \Omega\sigma_h, \tag{3-4}$$

where Ω is the partial molar volume of lithium ion in the active particle and σ_h is the hydrostatic stress in the particle.

Explicit expressions of μ_c can be found in the literature [21, 53]. However, since it is the gradient of the chemical potential, rather than the chemical potential itself, that drives diffusion,

the explicit expression of the chemical potential is not crucial for the diffusion equation. Substituting Eq. (3-4) into Eq. (3-2), the flux is given by

$$\mathbf{J} = -Mc\left(\frac{\partial \mu_c}{\partial c} \nabla c - \Omega \nabla \sigma_h \right). \tag{3-5}$$

The open circuit potential (with respect to lithium metal) of the active particle, E_{ref}, depends on the difference in chemical potential between a lithium metal (μ^{θ}) and the active particle (μ),

$$E_{ref} = \frac{\mu^{\theta} - \mu_c}{F}, \tag{3-6}$$

where F is Faraday constant. Then the term $\partial \mu_c / \partial c$ can be determined through the profile of the open circuit potential as

$$\frac{\partial \mu_c}{\partial c} = -F \frac{\partial E_{ref}}{\partial c} = -\frac{F}{c_{\max}} \frac{\partial E_{ref}}{\partial x_{Li}} = -\frac{FK}{c_{\max}}, \tag{3-7}$$

where $c_{\max}$ is the maximum lithium concentration in the solid, x_{Li} is the lithium fraction inside the active material, and $K = \partial E_{ref} / \partial x_{Li}$ is called thermodynamic factor in this work.

Given that the lithium ion diffusion in the active material occurs by a vacancy mechanism, the mobility decreases with the increase of lithium concentration. With this consideration, the mobility can be expressed by [53]

$$M = M_0 \left(1 - \frac{c}{c_{\max}} \right), \tag{3-8}$$

where $M_0 = D_0 / RT$ is the lithium ion mobility in the solid, D_0 is diffusivity, *R* is gas constant, and *T* is absolute temperature.

Combining Eqs. (3-2)–(3-8) and considering the symmetry of a spherical particle, we can obtain that the flux of lithium ions is along the radial direction, *r*, of the particle, which is given by

$$J = \frac{D_{eff}}{RT}\left(FK\frac{\partial c}{\partial r} + \Omega c_{\max}\frac{\partial \sigma_h}{\partial r} \right) = J_c + J_m \ , \tag{3-9}$$

where $D_{eff} = D_0\left(1-\frac{c}{c_{\max}}\right)\left(\frac{c}{c_{\max}}\right)$ is the effective diffusivity, $J_c = \frac{D_{eff}FK}{RT}\frac{\partial c}{\partial r}$ is the chemically driven flux, and $J_m = \frac{D_{eff}\Omega c_{\max}}{RT}\frac{\partial \sigma_h}{\partial r}$ is the mechanically driven flux.

Equation (3-1) takes the form of $\partial c/\partial t + (1/r^2)\partial(r^2 J)/\partial r = 0$ in the spherical coordinate. Solving this equation together with Eq. (3-9) gives the concentration field in the core and in the shell. In the following we use the subscript 1 and 2 to denote the field in the core and in the shell, respectively.

Prior models assume that the lithium concentration is continuous across the phase interface, i.e. $c_1(r=a) = c_2(r=a)$ [45]. However, as the core and the shell have different affinity for the lithium, a more rigorous expression to bridge the two regions is using the chemical potential,

$$\mu_1(r=a) = \mu_2(r=a). \tag{3-10}$$

The continuous chemical potential at the core-shell interface, $\mu_1(r=a) = \mu_2(r=a)$, can be transformed to

$$\mu_{c,1}(c_1) - \Omega_1\sigma_{h,1} = \mu_{c,2}(c_2) - \Omega_2\sigma_{h,2} \ . \tag{3-11}$$

As $E_{ref} = \frac{\mu^\theta - \mu_c}{F}$, the interface condition can further be derived as

$$-FE_{ref,1}(c_1)-\Omega_1\sigma_{h,1}=-FE_{ref,2}(c_2)-\Omega_2\sigma_{h,2}. \tag{3-12}$$

Thus, the lithium concentration of the shell at the interface is

$$c_2=E_{ref,2}^{-1}\left[\frac{\Omega_1\sigma_{h,1}-\Omega_2\sigma_{h,2}}{F}+E_{ref,1}(c_1)\right], \tag{3-13}$$

where $E_{ref,2}^{-1}$ is the inverse function of the open circuit potential of the shell.

The lithium flux is continuous across the phase interface,

$$J_1(r=a)=J_2(r=a). \tag{3-14}$$

The boundary conditions are given by

$$\begin{aligned} &r=0:\frac{\partial c_1}{\partial r}=0;\\ &r=b:J_2=\frac{i_{app}}{Fa_sL}, \end{aligned} \tag{3-15}$$

where i_{app} is the applied current density on the electrode in the unit of A m^{-2}, $a_s=3\varepsilon_s/b$ is the active surface area per unit electrode volume, ε_s is the volume fraction of active solid particles in the electrode, and L is the electrode thickness. Note that we define $i_{app}<0$ for intercalation (discharging when the studied particle is used as cathode) and $i_{app}>0$ for de-intercalation (charging when the studied particle is used as cathode).

The initial conditions are given by

$$t=0:c_1=c_{1,0},c_2=c_{2,0}\ . \tag{3-16}$$

The initial concentration of the two phases should satisfy equal chemical potential, i.e. $t=0:\mu_1=\mu_2$.

The solid diffusion inside the particle can be coupled with the electrode level behavior using the single particle model [58]. The cell voltage with respect to a lithium reference electrode is given by

$$V = E_{ref,2}\left(c_2(r=b)\right) + \frac{2RT}{F}\ln\left(\frac{\sqrt{m^2+4}+m}{2}\right) + i_{app}R_{sol}\ , \tag{3-17}$$

where $m = \dfrac{i_{app}}{Fa_s Lkc_e^{0.5}\left(c_2(r=b)\right)^{0.5}\left(c_{2,\max} - c_2(r=b)\right)^{0.5}}$, k is the reaction rate constant of the shell material, c_e is the lithium ion concentration in the electrolyte, R_{sol} is the electrolyte resistance in the unit of Ω m^2.

3.2.2 Mechanics

Stress equilibrium, either in the core or in the shell, is given by

$$\frac{\partial \sigma_{rr}}{\partial r} + 2\frac{\sigma_{rr} - \sigma_{\theta\theta}}{r} = 0\ , \tag{3-18}$$

where σ_{rr} is the radial stress and $\sigma_{\theta\theta}$ is the tangential stress.

The strain components are written as functions of the displacement,

$$\varepsilon_{rr} = \frac{du}{dr}, \varepsilon_{\theta\theta} = \frac{u}{r}\ , \tag{3-19}$$

where ε_{rr} is the radial strain, $\varepsilon_{\theta\theta}$ is the tangential strain and u is the radial displacement.

The relations between stress and strain are given by

$$\begin{aligned}
\sigma_{rr} &= \frac{E}{(1+\nu)(1-2\nu)}\left[(1-\nu)\varepsilon_{rr} + 2\nu\varepsilon_{\theta\theta} - (1+\nu)\frac{\Omega\tilde{c}}{3}\right], \\
\sigma_{\theta\theta} &= \frac{E}{(1+\nu)(1-2\nu)}\left[\nu\varepsilon_{rr} + \varepsilon_{\theta\theta} - (1+\nu)\frac{\Omega\tilde{c}}{3}\right],
\end{aligned} \tag{3-20}$$

where E is Young's modulus, ν is Poisson's ratio, Ω is the partial molar volume of lithium ion in the active particle, $\tilde{c} = c - c_0$ is the difference between lithium concentration at the current state, c, and the initial stress-free state, c_0.

Substituting Eqs. (3-19) and (3-20) into Eq. (3-18), the radial displacement is governed by

$$\frac{d}{dr}\left(\frac{1}{r^2}\frac{d}{dr}\left(r^2 u\right)\right) = \frac{1+\nu}{1-\nu}\frac{\Omega}{3}\frac{d\tilde{c}}{dr} \ , \tag{3-21}$$

We use the subscript 1 and 2 to denote the field in the core and in the shell, respectively. The solutions of Eq. (18) in the core and in the shell take the forms of

$$\text{In the core } (0 \le r \le a): \ u_1 = A_1 r + \frac{B_1}{r^2} + \frac{(1+\nu_1)}{3(1-\nu_1)}\frac{\Omega_1}{r^2}\int_0^r \tilde{c}_1 r^2 dr \, , \tag{3-22}$$

$$\text{In the shell } (a \le r \le b): \ u_2 = A_2 r + \frac{B_2}{r^2} + \frac{(1+\nu_2)}{3(1-\nu_2)}\frac{\Omega_2}{r^2}\int_a^r \tilde{c}_2 r^2 dr \, , \tag{3-23}$$

where A_1, B_1, A_2, and B_2 are constants to be determined by the continuity conditions and the boundary conditions. The continuity of displacement and radial stress at the interface between the core and the shell is given by

$$\begin{aligned} &u_1(r=a) = u_2(r=a), \\ &\sigma_{rr,1}(r=a) = \sigma_{rr,2}(r=a). \end{aligned} \tag{3-24}$$

The boundary conditions are given by

$$\begin{aligned} &u_1(r=0) = 0, \\ &\sigma_{rr,2}(r=b) = 0. \end{aligned} \tag{3-25}$$

Substituting Eqs. (3-22) and (3-23) into Eqs. (3-19) and (3-20), and further into Eqs. (3-24) and (3-25), we can solve for A_1, B_1, A_2, and B_2, and obtain the stress and displacement fields in the core and in the shell as below:

The radial stress at the core-shell interface, σ_{rr}^{cs}

$$\sigma_{rr}^{cs}=\frac{2E_1E_2}{a^3}\frac{\Omega_2\int_a^b\tilde{c}_2r^2dr-\left[\left(\frac{b}{a}\right)^3-1\right]\Omega_1\int_0^a\tilde{c}_1r^2dr}{\left(\frac{b}{a}\right)^3\left[E_1(1+\nu_2)+2E_2(1-2\nu_1)\right]+2\left[E_1(1-2\nu_2)-E_2(1-2\nu_1)\right]} \tag{3-26}$$

In the core ($0\le r\le a$):

$$\sigma_{rr,1}=\sigma_{rr}^{cs}+\frac{2\Omega_1E_1}{3(1-\nu_1)}\left(\frac{1}{a^3}\int_0^a\tilde{c}_1r^2dr-\frac{1}{r^3}\int_0^r\tilde{c}_1r^2dr\right), \tag{3-27}$$

$$\sigma_{\theta\theta,1}=\sigma_{rr}^{cs}+\frac{\Omega_1E_1}{3(1-\nu_1)}\left(\frac{2}{a^3}\int_0^a\tilde{c}_1r^2dr+\frac{1}{r^3}\int_0^r\tilde{c}_1r^2dr-\tilde{c}_1\right), \tag{3-28}$$

$$u_1=\frac{r(1-2\nu_1)\sigma_{rr}^{cs}}{E_1}+\frac{r\Omega_1}{3}\left[\frac{2(1-2\nu_1)}{1-\nu_1}\frac{1}{a^3}\int_0^a\tilde{c}_1r^2dr+\frac{1+\nu_1}{1-\nu_1}\frac{1}{r^3}\int_0^r\tilde{c}_1r^2dr\right]. \tag{3-29}$$

In the shell ($a\le r\le b$):

$$\sigma_{rr,2}=\frac{a^3}{b^3-a^3}\left[\left(\frac{b}{r}\right)^3-1\right]\sigma_{rr}^{cs}+\frac{2\Omega_2E_2}{3(1-\nu_2)}\left[\frac{1}{b^3-a^3}\left(1-\left(\frac{a}{r}\right)^3\right)\int_a^b\tilde{c}_2r^2dr-\frac{1}{r^3}\int_a^r\tilde{c}_2r^2dr\right] \tag{3-30}$$

$$\begin{aligned}\sigma_{\theta\theta,2}=&-\frac{a^3}{b^3-a^3}\left[1+\frac{1}{2}\left(\frac{b}{r}\right)^3\right]\sigma_{rr}^{cs}\\&+\frac{\Omega_2E_2}{3(1-\nu_2)}\left[\frac{1}{b^3-a^3}\left(2+\left(\frac{a}{r}\right)^3\right)\int_a^b\tilde{c}_2r^2dr+\frac{1}{r^3}\int_a^r\tilde{c}_2r^2dr-\tilde{c}_2\right]\end{aligned} \tag{3-31}$$

$$u_2 = -\frac{ra^3}{(b^3-a^3)E_2}\left[(1-2\nu_2)+\frac{1}{2}\left(\frac{b}{r}\right)^3(1+\nu_2)\right]\sigma_{rr}^{cs} + \frac{r\Omega_2}{3}\left[\frac{1}{b^3-a^3}\left(\frac{2(1-2\nu_2)}{1-\nu_2}+\frac{1+\nu_2}{1-\nu_2}\left(\frac{a}{r}\right)^3\right)\int_a^b \tilde{c}_2 r^2 dr + \frac{1+\nu_2}{1-\nu_2}\frac{1}{r^3}\int_a^r \tilde{c}_2 r^2 dr\right] \quad (3\text{-}32)$$

3.2.3 Parameters

In this work, the core is assumed to be $LiNi_{0.8}Mn_{0.1}Co_{0.1}O_2$ (NMC 811) while the shell is assumed to be $LiNi_{0.4}Mn_{0.4}Co_{0.2}O_2$ (NMC 442). The Ni-rich core is designed to provide high energy density while the Mn-rich shell is used to improve the stability.

The open circuit potential and thermodynamic factor of the core (NMC 811) [59] and shell (NMC 442) [60] are shown in Figure 3.2.

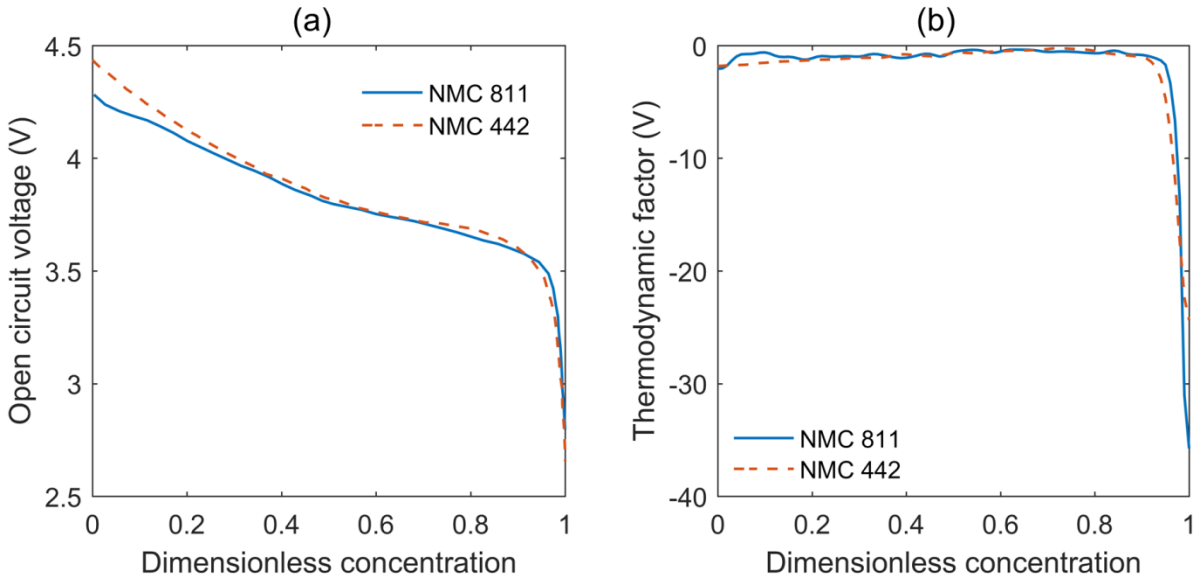

Figure 3.2. Open circuit potential and thermodynamic factor profiles of the core (NMC 811) and shell (NMC 442)

The maximum lithium concentration inside the active particle can be approximated as

$$c_{max} = \frac{Q\rho}{F}, \quad (3\text{-}33)$$

where Q is the specific capacity, ρ is the density and F is Faraday constant. The theoretical capacity of NMC 811 is given as 202 mAh g^{-1}, and the theoretical capacity of NMC 442 is given as 160 mAh g^{-1}. Assuming the density of NMC particle is 4210 kg m^{-3}, the maximum concentration of NMC 811 is 31730 mol m^{-3} and the maximum concentration of NMC 442 is 25133 mol m^{-3}.

The partial molar volume of lithium inside the solid is given as

$$\Omega = \frac{3\varepsilon}{\Delta c} = \frac{3}{\Delta c}\left[\left(1+\frac{\Delta V}{V_0}\right)^{\frac{1}{3}} - 1\right], \tag{3-34}$$

where $\varepsilon = \left(1+\frac{\Delta V}{V_0}\right)^{\frac{1}{3}} - 1$ is the strain corresponding to a concentration change of Δc, $\frac{\Delta V}{V_0}$ is the volume change rate corresponding to a concentration change of Δc.

As reported in Ref. [61], the volume change rate of NMC 811 lattice is 5.1% from $Li_0Ni_{0.8}Mn_{0.1}Co_{0.1}O_2$ to $LiNi_{0.8}Mn_{0.1}Co_{0.1}O_2$. Thus, the partial molar volume of lithium in NMC 811 is 1.6×10^{-6} m^3 mol^{-1}.

As reported in Ref. [62], the volume change rate of NMC 442 lattice is 2.37% from $Li_{0.05}Ni_{0.4}Mn_{0.4}Co_{0.2}O_2$ to $LiNi_{0.4}Mn_{0.4}Co_{0.2}O_2$. Thus, the partial molar volume of lithium in NMC 442 is 1.01×10^{-6} m^3 mol^{-1}.

As shown in Ref. [63], the lithium diffusivity increases with the Ni content. In this work, we set the diffusivity of NMC 811 as 5.5×10^{-14} m^2 s^{-1} and the diffusivity of NMC 442 as 4×10^{-14} m^2 s^{-1}.

The mechanical properties of $LiNi_xMn_yCo_zO_2$ (NMC) have been predicted using first principle calculations [64]. The calculation results show that the composition has a small effect

on the Young's modulus and Poisson's ratio of the active materials. In this work, the Young's modulus is assumed to be 175 GPa, and the Poisson's ratio is assumed to be 0.3 [64].

The parameters used in the model are summarized in Table 3.1.

Table 3.1. Parameters used in the model

Parameter	Symbol	Value	
Electrode Level			
Electrolyte resistance	R_{sol}	3.245×10^{-4} Ω m^2	
Cathode thickness	L	50 μm	
Cathode solid phase ratio	ε_s	0.55	
Electrolyte concentration	c_e	1000 mol m^{-3}	
Upper voltage		4.3 V	
Lower voltage		3.0 V	
Particle Level		Core (NMC 811)	Shell (NMC 442)
Maximum lithium concentration	c_{max}	31730 mol m^{-3}	25133 mol m^{-3}
Partial molar volume of lithium	Ω	1.6×10^{-6} m^3 mol^{-1}	1.01×10^{-6} m^3 mol^{-1}
Diffusivity	$D_0(=M_0RT)$	5.5×10^{-14} m^2 s^{-1}	4×10^{-14} m^2 s^{-1}
Young's modulus	E	175 GPa	175 GPa
Poisson's ratio	ν	0.3	0.3
Reaction constant	k	-	5×10^{-10} $m^{2.5}$ $mol^{-0.5}$ s^{-1}
Initial concentration for lithiation	c_0	$0.02c_{max}$	Calculated from $\mu_1=\mu_2$
Initial concentration for de-lithiation	c_0	$0.98c_{max}$	Calculated from $\mu_1=\mu_2$

3.3 Results and Discussion

Simulation results of lithium intercalation are shown in Figure 3.3. Figure 3.3(a) shows the lithium concentration along the particle radius. A concentration jump can be observed at the core-shell interface, which results from the material difference (i.e. maximum lithium concentration and OCP) between the core and the shell. Initially, the lithium concentration of the shell is much higher than the core as required by the equilibrium of chemical potential between the core and the shell. As lithiation proceeds, the concentration jump evolves to ensure a

continuous chemical potential across the interface, as shown in Figure 3.3(b). Note that the chemical potential here includes both the chemical and mechanical effects. Figure 3.3(c) shows the dimensionless concentration normalized by the maximum concentration of the core and of the shell, respectively. The dimensionless concentration jump gradually vanishes since the OCV difference between the core and the shell decreases as the dimensionless concentration approaches to 1.

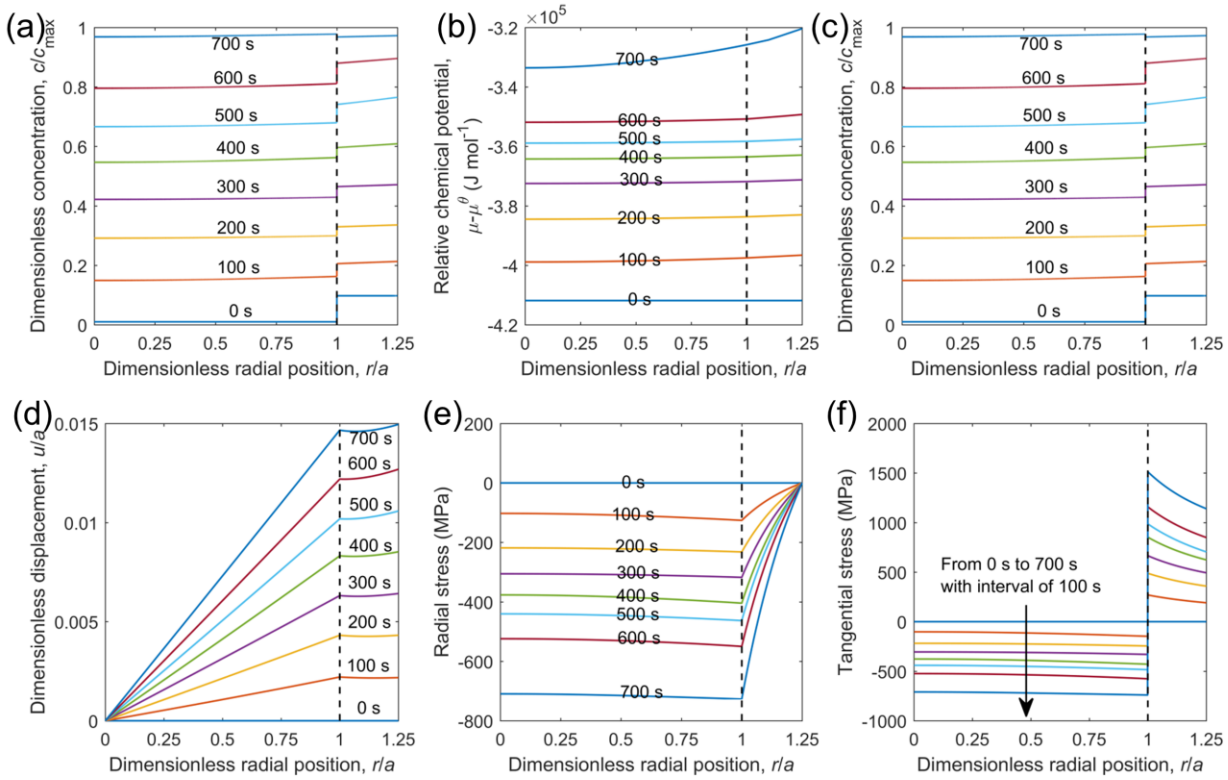

Figure 3.3. Radial distribution of (a) concentration, (b) relative chemical potential, (c) dimensionless concentration, (d) dimensionless displacement, (e) radial stress and (f) tangential stress at eight times during lithium intercalation. The dimensionless concentration is defined with respect to the maximum concentration of the core and of the shell, respectively. The relative chemical potential is defined as $\mu-\mu^{\theta}$, where μ^{θ} is the chemical potential of lithium in lithium metal. The vertical dash line represents the core-shell interface. In this simulation, a = 4 μm, b = 5 μm and i_{app} = -100 A m^{-2}.

The radial displacement associated with lithiation is shown in Figure 3.3(d). The shell has smaller radial expansion than the core because: 1) the shell has a smaller partial molar volume than the core, as listed in Table 3.1; and 2) the lithium concentration change of the shell is smaller than the core, as shown in Figure 3.3(a). Thus, the shell restricts the expansion of the core to certain extent. Also, note that the dimensionless displacement is small, showing that the elastic assumption is acceptable.

The effect of the shell restriction is illustrated by the compressive radial stress shown in Figure 3.3(e). Generally, the particle with a single component undergoes tensile radial stress during lithiation. However, the core-shell structure exhibits a compressive radial stress. This opposite mechanical behavior is understandable considering the constraining effect by the shell. To balance the radial stress, the tangential stress has a distribution as shown in Figure 3.3(f). Note that the tangential stress is discontinuous across the core-shell interface. The tensile tangential stress in the shell may lead to shell fracture.

Simulation results of lithium deintercalation are shown in Figure 3.4. Similar to lithium intercalation, a larger concentration change occurs in the core than that in the shell. Consequently, the shell hampers the contraction of the core, resulting in a large radial stress at the core-shell interface. This radial stress may cause debonding between the core and the shell.

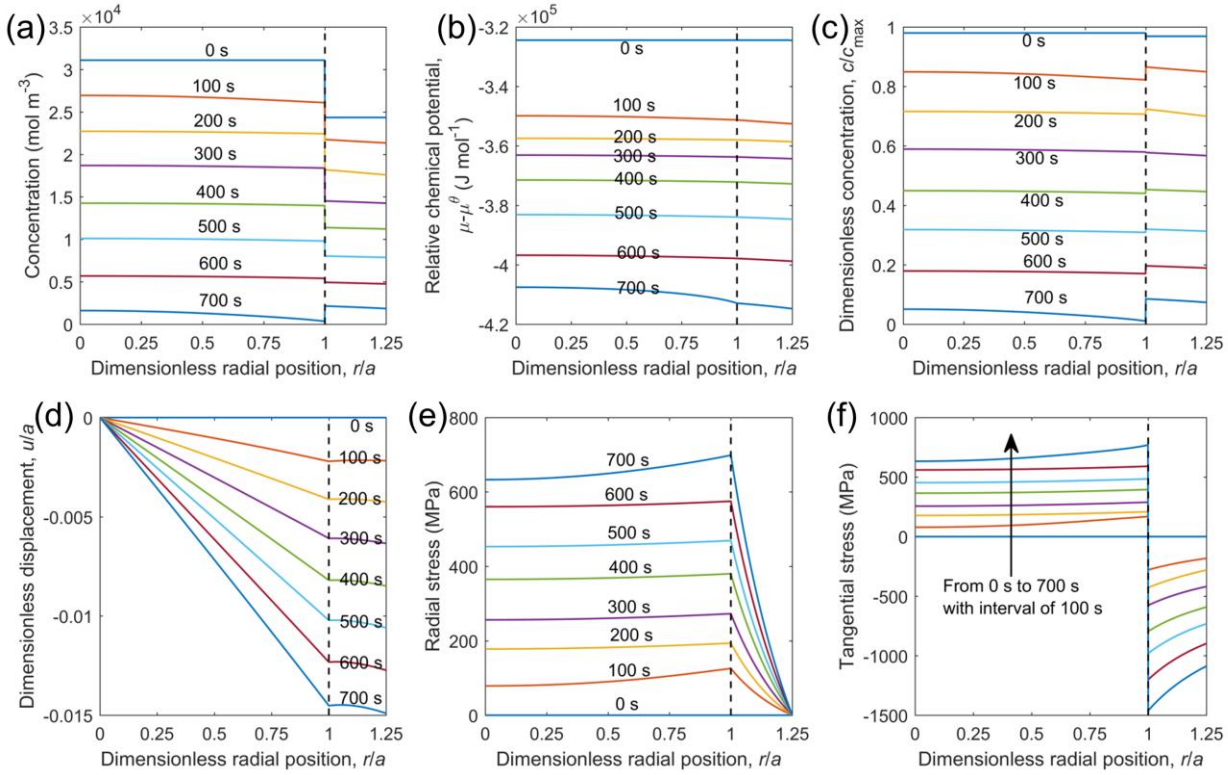

Figure 3.4. Radial distribution of (a) concentration, (b) relative chemical potential, (c) dimensionless concentration, (d) dimensionless displacement, (e) radial stress and (f) tangential stress at eight times during lithium deintercalation. The dimensionless concentration is defined with respect to the maximum concentration of the core and of the shell, respectively. The relative chemical potential is defined as $\mu-\mu^{\theta}$, where μ^{θ} is the chemical potential of lithium in lithium metal. The vertical dash line represents the core-shell interface. In this simulation, a = 4 μm, b = 5 μm and i_{app} = 100 A m^{-2}.

As discussed above, two possible failure modes exist in the core-shell structure. To quantify the relation between stress and failure modes, we use the energy release rate defined in fracture mechanics. The energy release rate of shell fracture is given by[50]

$$G_f = Z\frac{\left(\bar{\sigma}_{\theta\theta,2}\right)^2}{E_2}(b-a), \tag{3-35}$$

where $\bar{\sigma}_{\theta\theta,2} = \left(2\int_a^b \sigma_{\theta\theta,2} r dr\right) \Big/ \left(b^2-a^2\right)$ is the average tangential stress in the shell, Z = 2 is a dimensionless parameter for a channel crack in a spherical shell.

The energy release rate of core-shell debonding is given by [50]

$$G_d = \pi \frac{\left(\sigma_{rr}^{cs}\right)^2}{E_e}(b-a), \tag{3-36}$$

where the effective Young's modulus, E_e, is calculated by $1/E_e = \left(1/E_1 + 1/E_2\right)/2$. The energy release rate is a quadratic function of the radial stress at the core-shell interface, σ_{rr}^{cs}.

With the developed model and energy release rates, we have investigated the effect of design and operational parameters on the mechanics of core-shell structures. While a thicker shell helps reduce the stress in the core more, the shell itself can fail by fracture or debonding if it is too thick. When this happens, all the benefit from the shell would be lost. Therefore it is important to identify the parameter windows to avoid shell failure. Figure 3.5(a) shows the effect of core radius on the stress and energy release rate under constant outer shell radius and magnitude of current density. With an increase in the core radius, the tensile tangential stress in the shell grows rapidly, because the shell confining the core expansion becomes thinner. The fracture energy release rate, G_f, depends on both the tangential stress and the shell thickness. It increases and then decreases with the core radius, reaching a maximum at around a = 4 μm. In contrast, the debonding energy release rate, G_d, which depends on both the radial stress and the shell thickness, decreases with the core radius.

Figure 3.5(b) shows that the tangential stress decreases with the outer shell radius, while the radial stress increases with outer shell radius, when all other parameters are kept the same. G_f reaches a maximum at around b = 5 μm, while G_d grows rapidly with b.

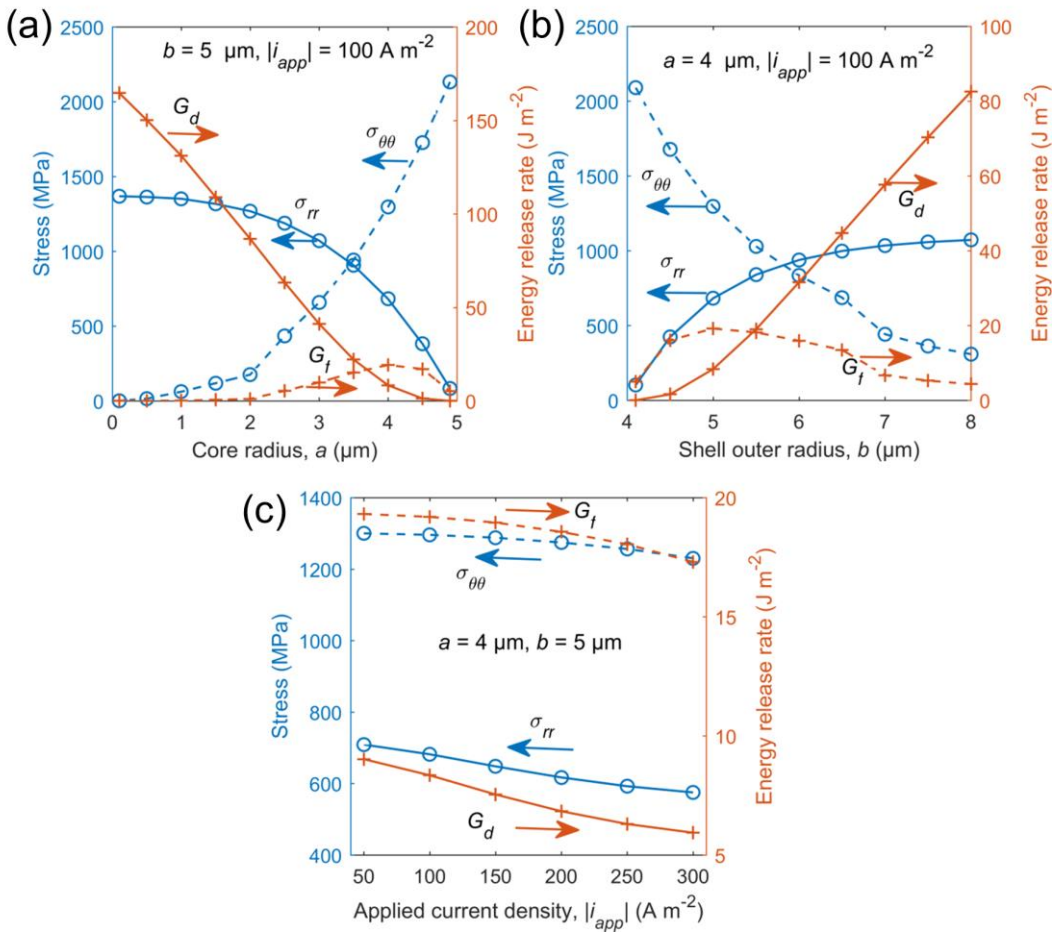

Figure 3.5. (a) Effect of core radius on stress and energy release rate under constant outer shell radius and magnitude of current density. (b) Effect of outer shell radius on stress and energy release rate under constant core radius and magnitude of current density. (c) Effect of the magnitude of current density on stress and energy release rate under constant core radius and outer shell radius. For all results, $\sigma_{\theta\theta}$ denotes the maximum average tangential stress of the shell during lithium intercalation and G_f denotes the fracture energy release rate at the time when $\sigma_{\theta\theta}$ reaches maximum, σ_{rr} denotes the maximum radial stress at the core-shell interface during lithium deintercalation and G_d denotes the debonding energy release rate at the time when σ_{rr} reaches maximum

For a particle of single component, high current density results in a large concentration gradient and therefore a large stress associated with the large concentration gradient. In contrast, the stress in the shell slightly decreases with the current density for a core-shell structure, as shown in Figure 3.5(c). The reason is the following. The stress inside the shell develops primarily from the difference between the concentration in the core and that in the shell.

Comparing with the large concentration jump across the interface of the core and the shell, the concentration within the core and the shell are relatively uniform, as shown in Figure 3.5(a) and Figure 3.5(a). Under a higher current density, less lithium ions intercalate into or de-intercalate from the particle, when discharging or charging terminates with the voltage hitting the lower or upper threshold. Thus, the volume change of the core and the resulted shell stress decrease with the current density.

Using this model, we have systematically investigated the effect of core and shell sizes on failure. As shown in Figure 3.6(a), large G_f occurs for a particle with a large core and a moderately thin shell. However, G_d mainly depends on the shell thickness, and slightly decreases with the core radius. We can also find that G_d is generally much larger than G_f. This observation suggests that core-shell debonding may be the major failure mode for the core-shell structure.

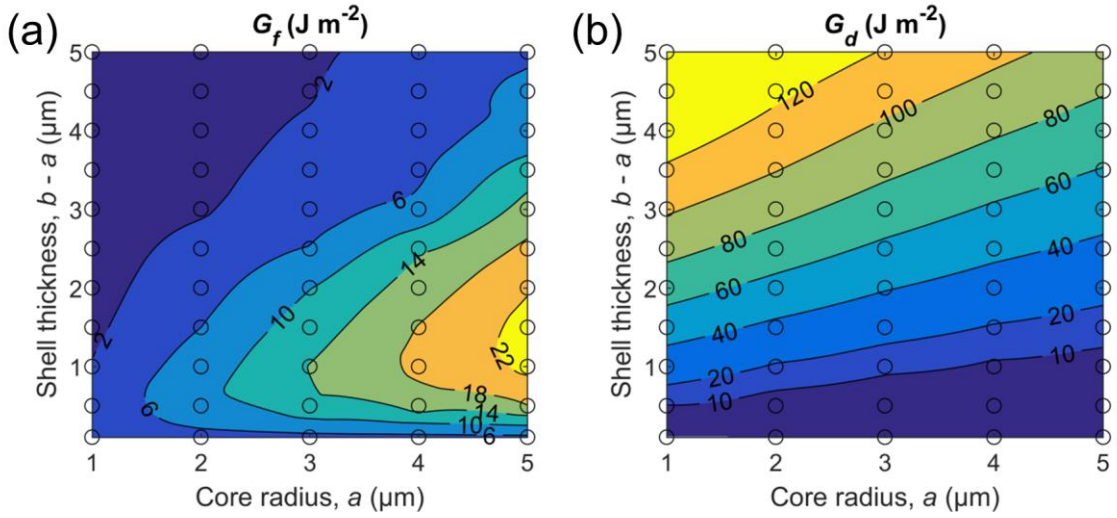

Figure 3.6. (a) Effect of core radius and shell thickness on fracture energy release rate. (b) Effect of core radius and shell thickness on debonding energy release rate. For all simulation results, the magnitude of current density is 100 A m^{-2}. The black dots represent the sampling points for simulations. The contour is generated based on the results of sampling points using natural neighbor interpolation method. The smallest shell thickness calculated is 0.1 μm.

One application of the contours in Figure 3.6 is to guide the particle design. To demonstrate the idea, we assume that the critical energy release rates for shell fracture and shell debonding are both 10 J m^{-2}. Then a feasible design map as shown in Figure 3.7 can be obtained. The green area denotes the feasible design region of core radius and shell thickness to avoid any shell failure. We can observe that the region defines an upper bound of the shell thickness as a function of the core radius. With the parameters used, the maximum shell thickness that can be used is less than ~ 0.7 μm. A shell thickness smaller than ~ 0.18 μm is able to avoid shell failure for the entire range of core radius from 1 μm to 5 μm.

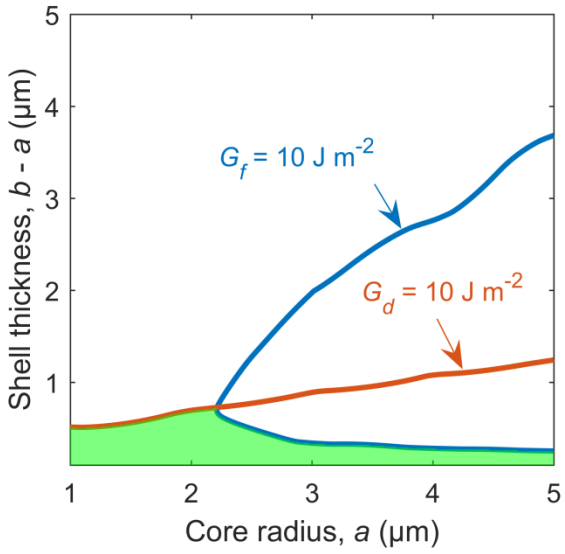

Figure 3.7. Application of the model for particle design. The green area denotes the feasible design region for the core-shell structure. The smallest shell thickness calculated is 0.1 μm.

3.4 Conclusion

In this work, we have developed a model to calculate the lithium concentration and stress inside a particle with the core-shell structure. The diffusion of lithium inside the particle is governed by the gradient of chemical potential, which includes both chemical and mechanical effects. The thermodynamic factor extracted from the open circuit voltage is used to characterize the chemical effect. For the mechanical part, the stress developed in the core-shell structure is

calculated using an analogy to thermal stress. As the core and shell are two phases with distinct affinity for lithium, we employ the continuous chemical potential, rather than the continuous lithium concentration, to bridge the core and the shell.

Using this model, we have simulated the mechanical behavior for a particle with a $LiNi_{0.8}Mn_{0.1}Co_{0.1}O_2$ core and a $LiNi_{0.4}Mn_{0.4}Co_{0.2}O_2$ shell. Simulation results reveal that a large tensile tangential stress is generated in the shell during lithiation, while a large tensile radial stress is generated at the core-shell interface during de-lithiation. These stress states are significantly different from the stress inside a particle of a single component. Using the energy release rate defined in fracture mechanics, we have quantified the effect of core radius, shell thickness and applied current density on the two failure modes of shell fracture and shell debonding, and constructed a design map. These results can be used to guide the design of core-shell structures.

Chapter 4 Modeling of Electrode

4.1 Introduction

A lithium-ion battery electrode is an inherent multiscale structure, which consists of many active material particles together with a small amount of binder and conductive additives. An electrode can be considered a continuum since its length scale is generally one or two orders of magnitude larger than the scale of the particles. Therefore, instead of resolving detailed electrode microstructures, the classic pseudo two-dimensional (P2D) electrochemical model [65] makes a separation between the electrode scale and the particle scale. The electrode scale is usually one dimensional along the electrode thickness direction, which accounts for solid potential, electrolyte potential and electrolyte concentration. The particle scale provides an additional dimension along the particle radius, which only resolves the solid concentration in the particle. The name of "pseudo two-dimensional" comes from the electrode dimension and the particle dimension, which are spatially separated. The two scales are coupled through the electrochemical kinetics at the particle surface. The P2D porous electrode model is widely used in the field of electrochemistry since it delivers good, satisfying accuracy with acceptable computational cost.

The active materials of lithium-ion battery electrodes exhibit volume change during lithium intercalation or de-intercalation. Owing to the relatively slow rate of solid diffusion, lithium concentration gradient develops inside particles, resulting in inhomogeneous expansion or contraction [66]. As a result, mechanical stress develops in the particles. The developed stress

further affects solid diffusion. The coupled stress and diffusion inside a single particle has been modeled by an analogy to thermal stress [3], which showed that the developed stress can enhance the solid diffusion by 35%. This approach has been extended to study many problems, such as the stress inside a nanowire [4], a secondary particle consisting of many primary particles [47], or a particle with an active shell [67]. The effect of active material parameters and morphology on stress has been explored [5, 6]. Researchers have investigated the fracture of a single particle [7-9] and the stress in active particles with plastic deformation [10, 11]. Consideration of stress in a single isolated particle extends the classic P2D electrochemical model by giving more accurate solid diffusion in a particle and allowing analysis of particle scale mechanical behaviors such as plasticity and fracture in a particle.

Stress can also affect the reaction kinetics. In a silicon particle coated by carbon shell, the lithiation-induced stress inside the silicon can halt the lithiation process [12]. The stress also affects the lithium deposition rate at the lithium metal surface, which suggests a mechanical approach to suppress the dendrite growth [13]. In a recent report [14], two identical Li-alloyed Si electrodes undergoing asymmetric bending-induced stresses create a difference in the chemical potential, and further generate an electrical current. However, this effect of stress on reaction kinetics has been omitted in most single-particle mechanical models, probably because those models adopt a constant intercalation rate as the boundary condition at the particle surface. Another limitation of the single-particle models is that the stress arising from particle interaction has not been addressed. The expansion or contraction of active particles is constrained by neighboring particles, current collectors and the battery case. This constraint can generate stress in a magnitude comparable to concentration gradient-induced stress [1, 2]. The lack of mechanical interaction between particles and effect of stress on the electrochemical reaction rate

makes mechanics and electrochemistry uncoupled at the continuum scale: an applied continuum scale stress in the electrode has no effect on the spatial distribution of electrochemical reaction in the electrode and vice versa.

The significance of particle interaction is also highlighted by the mechanical failure in the continuum scale, which brings battery degradation. Cracking in-between particles has been well observed in experiments [68], which can lead to disruption of electronic network, isolation of active materials, and exposure of fresh surface causing side reactions. In order to consider the cracks in-between particles, a model must include the particle interaction effect. Meanwhile, the intercalation rate at each particle surface is affected by the stress states of different particles. Thus, a model should incorporate the coupling of mechanics and electrochemistry at the continuum electrode scale in addition to the microscopic particle scale.

In this work, we develop two models using different approaches, i.e. a multi-scale model and a direct three-dimensional particle network model. Particle interaction and stress effect on the electrochemical reaction rate are incorporated in both models. We also use a general chemical potential that can capture the effects of both mechanical stress and phase transition on lithium diffusion. The first model couples mechanics and electrochemistry consistently at the microscopic and continuum scales through scale separation and local homogenization. The stress in each microscopic particle is a superposition of the intra-particle concentration gradient-induced stress and the particle interaction stress, and the latter is related to the continuum scale macroscopic stress through a representative volume element (RVE). The second model treats all particles explicitly with fully coupled three-dimensional mechanical-electrochemical equations. The particles and their network structures are simulated directly and accurately without any scale separation or homogenization. By comparing the two models, we demonstrate the unique

strength of each model and also use the accurate particle network model to validate the multi-scale model. Comparison of results shows that the multiscale model gives good, satisfying accuracy in simulating coupled mechanical and electrochemical behaviors while reducing the computational cost dramatically in comparison to the particle network model. The limitations of the multi-scale model are also pointed out through the comparison.

By incorporating particle interaction and fully coupling mechanics and electrochemistry consistently from particle to continuum scales, the multi-scale model has provided new physical insights and also serves as a powerful tool to address various coupled problems beyond what can be done currently. For instance, the continuum scale stress at a spatial point is found to directly reflect the average interaction stress for a particle at that point. The inter-particle interaction locally influences lithium intercalation and reaction rate. The continuum scale stress affects the lithium flux distribution in an electrode. As a tool, the multi-scale model enables quantitative investigation of various electrode-level behaviors, such as crack initiation and growth in an electrode, which is a critical problem for battery design. These cracks occur in-between particles and a model that incorporates particle interaction is essential. The multi-scale model can be further used to investigate how inter-particle cracks lead to the exposure of fresh surface resulting in side reactions, isolation of active particles, and disruption of electronic network. These effects cause capacity fade and an increase of internal resistance. With the multiscale model, the battery electrode is treated as a continuum solid so that existing method for fracture mechanics analysis can be directly applied. It is known that extending fracture mechanics to piezoelectric materials has generated lots of new understanding and interesting results. Similarly, the multiscale model in this work allows extending fracture mechanics to study electrochemical materials. We expect that exciting new findings and results can be generated. The model can be

used to study coupled mechanical-electrochemical degradation behaviors and provide design guidance for increasing the cycle life of a battery. The model will enable the study of new mechanisms and problems not addressed before. For example, imagine a small 'dead' region in an electrode which is electronically isolated from the rest due to poor electronic connection. This region is mechanically the same as the rest, so it is not a crack. This dead region does not participate in lithium intercalation while its surrounding neighbor region does. The expansion of the neighbor region causes stress concentration, reduction of electronic connection, and further growth of the dead region. Such a new type of non-crack damage can be captured only with the proposed fully coupled multiscale model. As another example, the model can be used to study the interesting electrochemical reaction behaviors associated with the stress concentration around a crack tip, or be used to study the self-generated stress and deformation in an electrode for possible actuation applications. As a tool for battery electrode design, the proposed model can be used to design material or electrode patterns to reduce electrode fracture for long battery cycle life, or to design the stress field to facilitate electrochemical reaction and transport for fast charging and other applications beyond what can be done with existing models.

4.2 Multi-Scale Model

4.2.1 Scale Separation and Coupling

In the electrochemical part, consistent with the porous electrode theory, we separate the microscopic particle scale and the continuum electrode scale. The continuum scale resolves the spatial distribution of solid potential, electrolyte potential and electrolyte lithium concentration in the electrode, while the particle scale resolves the lithium concentration distribution in a particle located at any spatial point in the electrode. Following the widely accepted and validated assumption in electrochemical modeling, we assume spherical particle shape and locally uniform

particle size. The condition of locally uniform particle size allows one particle to represent all the particles in its small local region, which corresponds to a spatial point in the continuum scale. Note that in the continuum scale the particle size can be a function of spatial position, so that a distribution of particle sizes can be considered by the model. An example is varying particle sizes along the electrode thickness direction. The essence of multi-scale modeling is that the detail of microstructures becomes insignificant after homogenization, which has been widely used in the mechanical modeling of composites. It should be noted that here our focus is to lay down a framework, which can be extended to consider more general cases such as locally mixed particle sizes or material properties. For instance, if there are two different particle sizes in a local region, we need to consider two representative particles to represent a local region, which corresponds to a spatial point in the continuum scale. This can be done by extending the work.

In the mechanical part, to address particle interaction, consider a particle in the electrode surrounded by other particles as shown in Figure 4.1(a). The stress in particle 1 can be divided into two components. The first component is the intra-particle concentration gradient-induced stress, denoted as σ_{ij}^{c}. The second component, denoted as σ_{ij}^{i}, stems from the particle interaction loading, $\mathbf{t}$. Note that $\mathbf{t}$ includes both normal and tangential effects. It should be noted that σ_{ij}^{c} and σ_{ij}^{i} affect each other. For instance, particle interaction will regulate the Li concentration in a particle and therefore alter the stress field within the particle. However, such interaction does not mean the two fields are not separable. As will be shown later, the two fields have clear definitions and are uniquely determined without any ambiguity. For instance, σ_{ij}^{i} is uniquely determined by the force exerted on the particle surface, $\mathbf{t}$. σ_{ij}^{i} is uniquely determined by the concentration field in the particle. Another way to look at the separation of these two fields is to consider it as an approach to facilitate the analytical derivation, since the total stress

in a particle is eventually calculated for the electrochemical-mechanical coupling. In this point of view, we do not even require the field separation to be unique, though the two fields are indeed unique and have clear physical meanings.

For a linear elastic problem, the total stress in the particle is a superposition of σ_{ij}^{c} and σ_{ij}^{i}. σ_{ij}^{c} can be easily determined using the intra-particle concentration profile given in the electrochemical part. However, the determination of σ_{ij}^{i} is more complex because solving the exact **t** exerted on each particle by neighboring particles could be cumbersome. Generally, **t** depends on not only the magnitude of neighboring particle deformation, but also the local morphology of particle network. Our approach is to consider a RVE that consists of many particles as shown in Figure 4.1(b), and relate the particle interaction stress to the continuum scale stress, Σ_{ij}, which can be viewed as a far-field load on the RVE.

Based on volume average, the continuum scale stress is given by

$$\Sigma_{ij} = f_s \left\langle \sigma_{ij}^{c} + \sigma_{ij}^{i} \right\rangle_s , \tag{4-1}$$

where $\left\langle \sigma_{ij}^{c} + \sigma_{ij}^{i} \right\rangle_s$ is the volume average of stress in the solid and ε_s is the volume fraction of the solid. Note that $\left\langle \sigma_{ij}^{c} \right\rangle_s = 0$ since the concentration-induced stress field in the particle is self-equilibrium. Thus we have $\Sigma_{ij} = f_s \left\langle \sigma_{ij}^{i} \right\rangle_s$. This equation provides an important insight that the continuum scale stress at a spatial point directly reflects the average interaction stress for a particle at that point. The hydrostatic component of the interaction stress is then given by

$$\left\langle \sigma_{h}^{i} \right\rangle_s = \frac{\Sigma_{xx} + \Sigma_{yy} + \Sigma_{zz}}{3 f_s} . \tag{4-2}$$

Figure 4.1(c) shows a schematic of the multi-scale model, illustrating the coupling between electrochemistry and mechanics and the coupling between scales. At the microscopic particle scale electrochemistry and mechanics are coupled through (1) the solid lithium concentration in the particle, c_s, which affects the particle stress; and (2) the hydrostatic stress in the particle, σ_h, which affects the solid diffusion. At the continuum scale, the coupling between electrochemistry and mechanics are reflected by the relation between the potential in the solid, Φ_s, the potential in the electrolyte, Φ_e, the lithium ion concentration in the electrolyte, c_e, and the continuum scale stress, Σ_{ij}. The electrochemistry fields Φ_s, Φ_e, c_e and the mechanics fields Σ_{ij} are coupled at the continuum scale in consistency with the microscale coupling through (1) the intercalation reaction current density, i, which at any spatial point in the electrode depends on the concentration, $c_{s,surf}$, and stress, $\sigma_{h,surf}$, on the surface of a particle located at that point; and (2) the particle interaction stress σ_{ij}^{i} which depends on the average lithium concentration in the particle, $c_{s,avg}$.

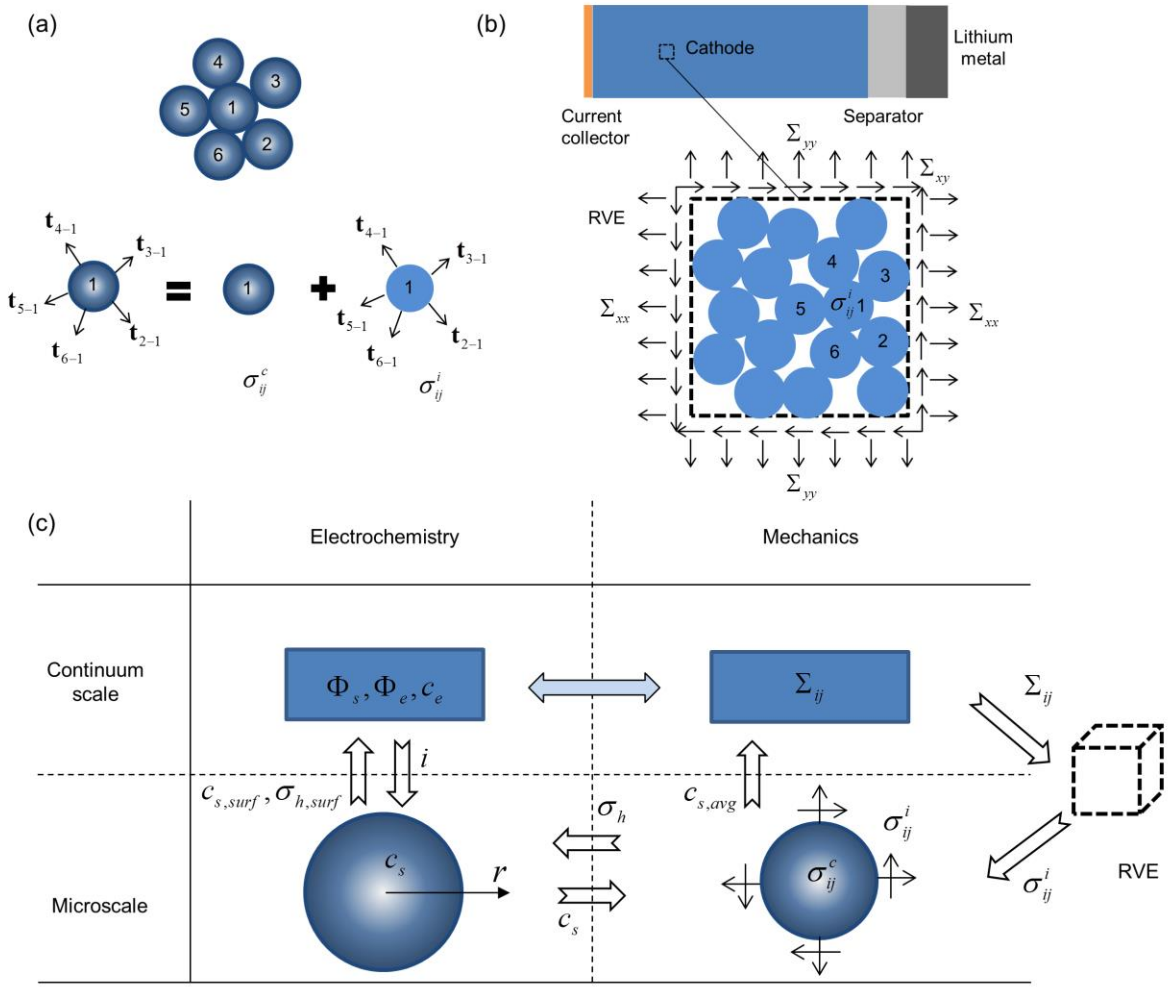

Figure 4.1. (a) The stress in a particle is the superposition of the concentration gradient-induced stress, σ_{ij}^{c}, and the stress from particle interaction, σ_{ij}^{i}. (b) The particle interaction stress is related to the continuum scale stress, Σ_{ij}. c) Schematic of the multi-scale model illustrating the coupling between electrochemistry and mechanics and the coupling between continuum and microscopic scales. Electrochemistry and mechanics are coupled at the microscopic scale through the lithium concentration, c_s, and the hydrostatic stress, σ_h, in the particle, and consistently at the continuum scale through the intercalation reaction current density, i, which depends on the concentration, $c_{s,surf}$, and stress, $\sigma_{h,surf}$, on the particle surface, and the particle interaction stress, σ_{ij}^{i}, which depends on the average lithium concentration in the particle, $c_{s,avg}$.

4.2.2 Electrochemistry

Continuum Scale

The current density in the electrolyte, $\mathbf{i}_e^H$, the lithium flux density in the electrolyte, $\mathbf{N}_e^H$, and the lithium flux in the solid, $\mathbf{i}_s^H$, are given by

$$\mathbf{i}_e^H = -\kappa_e^H \left[\nabla \Phi_e - \frac{2RT}{F} \left(1 + \frac{d \ln f_{\pm}}{d \ln c_e} \right) (1 - t_+) \nabla \ln c_e \right], \tag{4-3}$$

$$\mathbf{N}_e^H = -D_e^H \nabla c_e + \frac{\mathbf{i}_e^H t_+}{F}, \tag{4-4}$$

$$\mathbf{i}_s^H = -\kappa_s^H \nabla \Phi_s, \tag{4-5}$$

where the superscript '*H*' denotes continuum locally homogenized quantities. In other words, each spatial point of the electrode represents a local volume containing both the solid phase and the electrolyte solution phase. The flux density per area at a spatial point in the electrode is an average over a local cross-sectional area of the electrode at that spatial point. Take $\mathbf{N}_e^H$ as an example. For a plane with a normal unit vector of $\mathbf{n}$, $\mathbf{n} \cdot \mathbf{N}_e^H$ represents the amount of lithium crossing a unit area of this plane through the solution phase. Note that this density is defined on the unit area referring to the whole cross-sectional area rather than the pore area occupied by the solution phase. This definition is required by the continuum porous electrode theory. In contrast, we define the flux density on the area of each phase in the particle network model in section 3, where the particles and the electrolyte are modeled explicitly so that they always occupy difference spaces. In that definition the superscript '*H*' is removed. In these equations R is ideal gas constant, T is temperature, F is Faraday constant, $f_{\pm}$ is the electrolyte activity coefficient, and t_+ is the lithium ion transference number.

The homogenized electrolyte conductivity, κ_e^H, solid conductivity, κ_s^H, and electrolyte diffusivity, D_e^H, are given by the Bruggemen relation,

$$\kappa_e^H = \kappa_e f_e^{1.5}, \kappa_s^H = \kappa_s f_s^{1.5}, D_e^H = D_e f_e^{1.5}, \tag{4-6}$$

where κ_e is the bulk electrolyte conductivity, ε_e is the volume fraction of electrolyte, σ_s is the bulk solid conductivity, ε_s is the volume fraction of solid, and D_e is the bulk electrolyte diffusivity.

The conservation of charge and mass gives relations to the intercalation reaction current density, i, by

$$\nabla \cdot \mathbf{i}_e^H = a_s i, \tag{4-7}$$

$$\nabla \cdot \mathbf{i}_s^H = -a_s i, \tag{4-8}$$

$$f_e \frac{\partial c_e}{\partial t} = -\nabla \cdot \mathbf{N}_e^H + \frac{a_s i}{F}, \tag{4-9}$$

where the active surface area per unit electrode volume, a_s, is given by

$$a_s = \frac{3 f_s}{r_p}, \tag{4-10}$$

where r_p is the particle radius. The intercalation current density i is given later.

Microscale

The lithium diffusional flux in a solid particle is governed by the gradient of chemical potential [53],

$$\mathbf{N}_s = -M c_s \nabla \mu, \tag{4-11}$$

where M is the mobility and μ is the chemical potential of lithium in the solid particles. The diffusion of lithium is associated with the replacement of vacancy with lithium. A rigorous definition of $\mathbf{N}_s$ and μ is given in Appendix A, which has been shown equivalent to this expression.

Under the assumptions of small linear elastic deformation and no dependence of mechanical properties on lithium fraction [56], the chemical potential of lithium in the active particle is given by

$$\mu = \mu_c(c_s) - \Omega\sigma_h, \tag{4-12}$$

where $\mu_c(c_s)$ denotes the chemical potential at the stress-free state, Ω is the partial molar volume of lithium in the particle, and σ_h is the hydrostatic stress in the particle. Substituting Eq. (4-12) into Eq. (4-11), we have

$$\mathbf{N}_s = -Mc_s\left(\frac{\partial\mu_c}{\partial c_s}\nabla c_s - \Omega\nabla\sigma_h\right). \tag{4-13}$$

The dependence of chemical potential on concentration, $\partial\mu_c/\partial c_s$, can be obtained from the open circuit potential (OCP) curve. The OCP (with respect to lithium metal) of the active particle, E_{ref}, depends on the difference in chemical potential between a lithium metal (μ_{Li}^0) and the active particle (μ). In the OCP state the battery is in equilibrium, the lithium concentration in the particle is uniform, and there is no applied external force. Therefore, the OCP state is stress-free with $\mu = \mu_c(c_s)$. The OCP is given by

$$E_{ref} = \frac{\mu_{\mathrm{Li}}^0 - \mu_c}{F}. \tag{4-14}$$

The term $\partial\mu_c/\partial c_s$ can be determined by the OCP as

$$\frac{\partial \mu_c}{\partial c_s} = -F\frac{\partial E_{ref}}{\partial c_s} = -\frac{F}{c_{s,max}}\frac{\partial E_{ref}}{\partial x_{Li}} = -\frac{FK}{c_{s,max}}, \tag{4-15}$$

where $c_{s,max}$ is the maximum lithium concentration in the solid, x_{Li} is the lithium fraction inside the active material, and $K = \partial E_{ref} / \partial x_{Li}$ is called thermodynamic factor in this work. Note that the thermodynamic factor gives the value corresponding to the stress-free state.

Lithium diffusion in some classic active materials (such as graphite and lithium manganese oxide) occurs by a vacancy mechanism. The mobility decreases with the increase of lithium concentration, which can be written as [53]

$$M = M_0\left(1-\frac{c_s}{c_{s,max}}\right), \tag{4-16}$$

where M_0 is the lithium mobility in the solid under the condition of dilute lithium concentration, which relates to the diffusion coefficient by $D_0 = M_0 RT$. The diffusion flux in a spherical solid particle is along the radial *r* direction due to symmetry. With Eqs. (4-12)-(4-16), the diffusion flux $N_s(r)$ is given by

$$N_s = \frac{D_0}{RT}\left(\frac{c_s}{c_{s,max}}\right)\left(1-\frac{c_s}{c_{s,max}}\right)\left(FK\frac{\partial c_s}{\partial r} + \Omega c_{s,max}\frac{\partial \sigma_h}{\partial r}\right). \tag{4-17}$$

The expression of σ_h is given later.

The diffusion equation is

$$\frac{\partial c_s}{\partial t} + \frac{1}{r^2}\frac{\partial (r^2 N_s)}{\partial r} = 0. \tag{4-18}$$

The boundary and initial conditions for the solid diffusion are

$$\begin{aligned} &\frac{\partial c_s}{\partial r} = 0 \text{ at } r = 0, \\ &N_s = \frac{i}{F} \text{ at } r = r_p, \\ &c_s(r) = c_{s0} \text{ at } t = 0. \end{aligned} \tag{4-19}$$

Charge Transfer Kinetics

Traditionally, the charge transfer kinetics at the solid and electrolyte interface is described using the Bulter-Volmer equation,

$$i = i_0 \left[\exp\left(\frac{(1-\beta)F\eta}{RT} \right) - \exp\left(-\frac{\beta F \eta}{RT} \right) \right], \tag{4-20}$$

where i_0 is the exchange current density given by

$$i_0 = Fkc_{s,surf}^{\beta} c_e^{1-\beta} (c_{s,max} - c_{s,surf})^{1-\beta}, \tag{4-21}$$

where β is the cathodic symmetry factor and η is overpotential given by

$$\eta = \Phi_s - \Phi_e - E_{ref}(c_{s,surf}). \tag{4-22}$$

In this work, the charge transfer kinetics is generalized to include the effect of stress. The detailed derivation can be found in Appendix B. The generalized charge transfer kinetics is given by

$$i = i_0 \exp\left[\frac{\Omega \sigma_{h,surf} (\beta_m - \beta)}{RT} \right] \left[\exp\left(\frac{(1-\beta)F\eta_m}{RT} \right) - \exp\left(-\frac{\beta F \eta_m}{RT} \right) \right], \tag{4-23}$$

where $\sigma_{h,surf} = \sigma_h(r_p)$ is the hydrostatic stress on the particle surface, β_m is the mechanical cathodic symmetry factor, and η_m is the overpotential including the mechanical effect given by

$$\eta_m = \Phi_s - \Phi_e - E_{ref}(c_{s,surf}) - \frac{\Omega \sigma_{h,surf}}{F}. \tag{4-24}$$

The inclusion of mechanical stress brings two effects: the scaling of exchange current density and the shift of equilibrium potential.

4.2.3 Mechanics

Continuum Scale

The effective elastic modulus of the porous electrode can be determined from those of solid particles using several methods, such as self-consistent method [69], Mori-Tanaka method [70, 71] and finite element method [72]. In this work, we use the asymptotic homogenization method [73, 74]. The details and results of calculation can be found in Appendix C.

The macroscopic stress in the electrode scale, Σ_{ij}, is given by

$$\Sigma_{ij} = C^{H}_{ijkl}(e_{kl} - e_0\delta_{kl}), \tag{4-25}$$

where C^{H}_{ijkl} is the effective elastic modulus and e_{kl} is the strain. The eigenstrain of a RVE, $e_0\delta_{kl}$, comes from its volumetric change associated with the lithium intercalation/deintercalation of its particles. Here δ_{ij} is the Kronecker delta. e_0 is determined by the average concentration of the particle, $c_{s,avg}$, and the initial concentration, c_{s0}, giving

$$e_0 = \frac{\Omega^H}{3}(c_{s,avg} - c_{s0}), \tag{4-26}$$

where the "effective" partial molar volume of RVE, Ω^H, may differ from the Ω in Eq.(4-12) since only the active particles in the porous RVE are associated with the intercalation-induced strain. The relation between Ω^H and Ω is analogously to the relation between the thermal expansion coefficient of a porous solid and a bulk solid. In this work the "effective" Ω^H is

calculated using the asymptotic homogenization method shown in Appendix C, which yields $\Omega^H = \Omega$.

The equilibrium of macroscopic stress gives

$$\nabla \cdot \boldsymbol{\Sigma} = \mathbf{0}. \tag{4-27}$$

Microscale

In this section, we focus on the calculation of σ_h in the particle. Here we consider the average interaction stress of a particle because of interaction with all its neighbors. The hydrostatic stress on the particle surface is given by $\sigma_{h,surf} = \sigma_h^c\left(r_p\right) + \left\langle \sigma_h^i \right\rangle_s$. Eq. (4-2) has already related $\left\langle \sigma_h^i \right\rangle_s$ to the macroscopic stress. So here we focus on σ_h^c, the concentration-induced stress in an isolated particle.

The radial strain, ε_{rr}^c, and the tangential strain, $\varepsilon_{\theta\theta}^c$, are given by the radial displacement, u,

$$\varepsilon_{rr}^c = \frac{du}{dr}, \quad \varepsilon_{\theta\theta}^c = \frac{u}{r}. \tag{4-28}$$

The strains include an elastic part and a lithiation-induced part that is analogous to thermal strain,

$$\begin{aligned} \varepsilon_{rr}^c &= \frac{1}{E_p}\left(\sigma_{rr}^c - 2\nu_p \sigma_{\theta\theta}^c\right) + \frac{\Omega}{3}\tilde{c}, \\ \varepsilon_{\theta\theta}^c &= \frac{1}{E_p}\left(\sigma_{\theta\theta}^c - \nu_p\left(\sigma_{\theta\theta}^c + \sigma_{rr}^c\right)\right) + \frac{\Omega}{3}\tilde{c}, \end{aligned} \tag{4-29}$$

where $\tilde{c} = c_s - c_{s0}$ is the difference between lithium concentration at the current state, c_s, and the initial stress-free state, c_{s0}. E_p is the Young's modulus of the particle, ν_p is the Poisson's ratio of the particle, σ_{rr} is the radial stress, and $\sigma_{\theta\theta}$ is the tangential stress.

The equilibrium equation is given by

$$\frac{d\sigma_{rr}^c}{dr}+\frac{2}{r}\left(\sigma_{rr}^c-\sigma_{\theta\theta}^c\right)=0. \tag{4-30}$$

The boundary conditions are

$$\begin{aligned} &u=0 \text{ at } r=0, \\ &\sigma_{rr}^c=0 \text{ at } r=r_p. \end{aligned} \tag{4-31}$$

Solving Eqs. (4-28)-(4-31), we get

$$\sigma_{rr}^c(r)=\frac{2\Omega E_p}{3(1-\nu_p)}\left(\frac{1}{r_p^3}\int_0^{r_p}\tilde{c}r^2dr-\frac{1}{r^3}\int_0^{r}\tilde{c}r^2dr\right), \tag{4-32}$$

$$\sigma_{\theta\theta}^c(r)=\frac{\Omega E_p}{3(1-\nu_p)}\left(\frac{2}{r_p^3}\int_0^{r_p}\tilde{c}r^2dr+\frac{1}{r^3}\int_0^{r}\tilde{c}r^2dr-\tilde{c}\right). \tag{4-33}$$

$$\sigma_h^c(r)=\frac{\sigma_{rr}^c+2\sigma_{\theta\theta}^c}{3}=\frac{2\Omega E_p}{3(1-\nu_p)}\left(\frac{1}{r_p^3}\int_0^{r_p}\tilde{c}r^2dr-\frac{\tilde{c}}{3}\right). \tag{4-34}$$

Eq. (4-34) shows that σ_h^c is determined by the concertation profile in the particle and can be obtained by an integration. We can also get the radial displacement at the particle surface,

$$u^c(r_p)=\frac{\Omega}{r_p^2}\int_0^{r_p}\tilde{c}r^2dr=\frac{\Omega r_p}{3}\left(c_{s,avg}-c_{s0}\right), \tag{4-35}$$

where $c_{s,avg}=(3/r_p^3)\int_0^{r_p}c_s(r)r^2dr$ is the average lithium concentration inside the particle. Eq. (4-35) shows that the overall expansion or contraction of a particle, $u(r_p)/r_p=(\Omega/3)(c_{s,avg}-c_{s0})$, only depends on the average concentration regardless of the concentration profile. This result provides the basis of using the average concentration in Eq. (4-26).

4.3 Direct Three-dimensional Particle Network Model

In this model we consider all particles and their network structure explicitly with fully coupled three-dimensional mechanical-electrochemical equations.

The ionic current inside the electrolyte is described by

$$\mathbf{i}_e = -\kappa_e \left[\nabla \Phi_e - \frac{2RT}{F} \left(1 + \frac{d \ln f_{\pm}}{d \ln c_e} \right) (1 - t_+) \nabla \ln c_e \right], \tag{4-36}$$

where κ_e is the electrolyte conductivity. Note that although the form of Eq. (4-36) appears similar as Eq. (4-3), a major difference is that here the current density per area, $\mathbf{i}_e$, is defined on the cross-sectional area of a single phase instead of on the cross-sectional area of local phase mixtures, so κ_e instead of κ_e^H appears in the equation. Also note that in giving Eq. (4-36), Φ_e is defined as the potential of a lithium metal reference electrode at the point of interest in the electrolyte with respect to another lithium metal reference electrode at a fixed point (see more discussion on the definition of electrolyte potential in section 12.4 of [75]).

The lithium ion flux inside the electrolyte is driven by diffusion and migration,

$$\mathbf{N}_e = -D_e \nabla c_e + \frac{\mathbf{i}_e t_+}{F}, \tag{4-37}$$

where D_e is lithium ion diffusivity in the electrolyte.

The current in the solid particle matrix is given by

$$\mathbf{i}_s = -\kappa_s \nabla \Phi_s, \tag{4-38}$$

where κ_s is solid conductivity.

Similar as Eq. (4-17) but using the general gradient operator, the lithium flux in solid is given by

$$\mathbf{N}_s = \frac{D_0}{RT}\left(\frac{c_s}{c_{s,max}}\right)\left(1-\frac{c_s}{c_{s,max}}\right)\left(FK\nabla c_s + \Omega c_{s,max}\nabla\sigma_h\right). \tag{4-39}$$

Note that a particle is no longer spherically symmetric with explicit modeling of the particle network, therefore a general gradient operator is used.

The conservation of mass requires

$$\frac{\partial c_e}{\partial t} + \nabla\cdot\mathbf{N}_e = 0, \tag{4-40}$$

$$\frac{\partial c_s}{\partial t} + \nabla\cdot\mathbf{N}_s = 0. \tag{4-41}$$

The conservation of charge requires

$$\nabla\cdot\mathbf{i}_e = 0, \tag{4-42}$$

$$\nabla\cdot\mathbf{i}_s = 0. \tag{4-43}$$

The charge transfer kinetics at the particle surface follows Eq. (4-23), with the exchange current density given by Eq. (4-21) and the generalized overpotential given by Eq. (4-24).

Using the charge transfer current at the electrolyte-particle interface, the boundary conditions for $\mathbf{N}_e$, $\mathbf{N}_s$, $\mathbf{i}_e$ and $\mathbf{i}_s$ are

$$\begin{aligned}
&\mathbf{n}\cdot\mathbf{N}_e = \frac{i}{F},\\
&\mathbf{n}\cdot\mathbf{N}_s = \frac{i}{F},\\
&\mathbf{n}\cdot\mathbf{i}_e = i,\\
&\mathbf{n}\cdot\mathbf{i}_s = i.
\end{aligned} \tag{4-44}$$

where $\mathbf{n}$ is the unit normal vector pointing from the solid particle to the electrolyte.

The particle network forms a continuum solid of complicated geometry. The stress is the solid is given by

$$\sigma_{ij} = C_{ijkl}(e_{kl} - e_0\delta_{kl}), \tag{4-45}$$

where $C_{ijkl} = \lambda\delta_{ij}\delta_{kl} + \mu(\delta_{ik}\delta_{jl} + \delta_{il}\delta_{jk})$ is the elastic modulus, $\lambda = E\nu/\left[(1+\nu)(1-2\nu)\right]$ and $\mu = E/\left[2(1+\nu)\right]$. The eigenstrain at each spatial point in the solid is

$$e_0 = \frac{\Omega}{3}(c_s - c_{s0}), \tag{4-46}$$

where c_{s0} is the initial lithium concentration of the solid at the stress-free state.

The equilibrium of stress is given by

$$\nabla \cdot \boldsymbol{\sigma} = \mathbf{0}. \tag{4-47}$$

4.4 Examples

In the following we layout the detailed boundary and initial conditions using specific examples. For comparison, we will calculate the same setup using both the multiscale model and the particle network model. To introduce the setup we start with the particle network model since it provides more microstructure details.

4.4.1 Direct Simulation with Three-dimensional Particle Network Model

Figure 4.2 shows the schematic of the three-dimensional particle network model. The overlapping active particles constitute the backbone of the electrode, while the porous volume in-between the particles is occupied by the electrolyte. Binder, carbon black and other additives are omitted in the geometry. Lithium metal serves as the counter electrode. In application, there is a separator sandwiched between the electrode and lithium metal to avoid internal short-circuit. With a focus on modeling the electrode and the separator is very compliant, here we use a space to represent the separator.

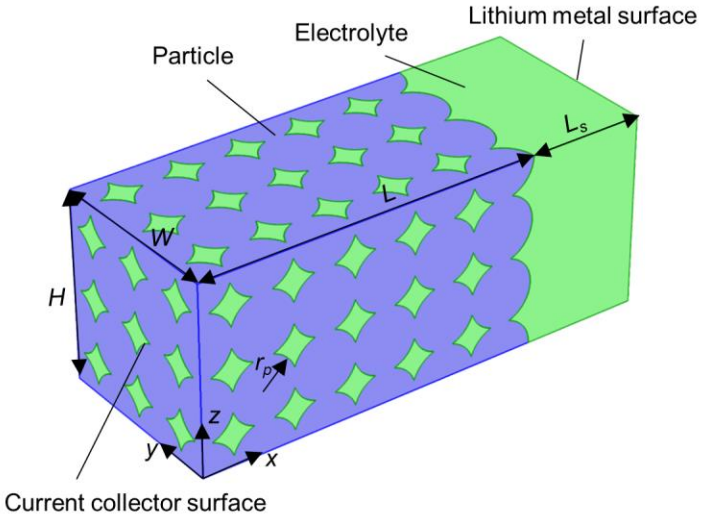

Figure 4.2. Schematic of the three-dimensional particle network model. r_p denotes the particle radius, L denotes the electrode thickness, H denotes the electrode height, W denotes the electrode width and L_s denotes the separator thickness. The distance between the centers of two neighboring particles is $1.9r_p$.

The symmetrical boundary conditions hold for $\mathbf{N}_e$, $\mathbf{N}_s$, $\mathbf{i}_e$ and $\mathbf{i}_s$ at the boundaries of $y=0$, $y=W$, $z=0$ and $z=H$, which are given by

$$\begin{aligned} &\mathbf{n}\cdot\mathbf{N}_e=0,\ \mathbf{n}\cdot\mathbf{N}_s=0,\\ &\mathbf{n}\cdot\mathbf{i}_e=0,\ \mathbf{n}\cdot\mathbf{i}_s=0. \end{aligned} \tag{4-48}$$

where **n** is the unit normal vector pointing outside from the model domain.

At $x=0$, where particles or electrolyte meet the current collector, we have

$$\begin{aligned} &\mathbf{n}\cdot\mathbf{N}_e=0,\ \mathbf{n}\cdot\mathbf{N}_s=0,\\ &\mathbf{n}\cdot\mathbf{i}_e=0,\ \mathbf{n}\cdot\mathbf{i}_s=-i_{app}. \end{aligned} \tag{4-49}$$

where **n** is the unit normal vector pointing from the current collector to the electrode, i_{app} is the applied current density and $i_{app}>0$ for discharge.

The boundary conditions at the lithium metal surface, $x=L+L_s$, are given by

$$\mathbf{n}\cdot\mathbf{N}_e = -\frac{i_{app}}{F},\ \mathbf{n}\cdot\mathbf{i}_e = -i_{app}. \tag{4-50}$$

where **n** is the unit normal vector pointing from the electrode to lithium metal.

The initial conditions are given by

$$c_e = c_{e0},\ c_s = c_{s0} \text{ at } t = 0. \tag{4-51}$$

The mechanical boundary conditions are given by

$$\begin{aligned} &\mathbf{u} = \mathbf{0} \text{ at } x = 0, \\ &\mathbf{n}\cdot\mathbf{u} = 0 \text{ at } y = 0, y = W, z = 0, z = H, \\ &\mathbf{n}\cdot\boldsymbol{\sigma} = \mathbf{0} \text{ at particle electrolyte interface.} \end{aligned} \tag{4-52}$$

where **u** is displacement, **n** is the unit normal vector pointing outside from the model domain in the expression of $\mathbf{n}\cdot\mathbf{u} = 0$, and **n** is the unit normal vector pointing from the particle to the electrolyte at the particle electrolyte interface in the expression of $\mathbf{n}\cdot\boldsymbol{\sigma} = \mathbf{0}$.

4.4.2 Multi-Scale Model

Now we solve the same setup in Figure 4.2 using the multi-scale model. Note that at the continuum scale the problem is essentially one dimensional in the *x* axis because of symmetry in the *y* and *z* axes. The fluxes $\mathbf{i}_e^H$, $\mathbf{N}_e^H$, and $\mathbf{i}_s^H$ are all along the *x* axis, or the electrode thickness direction. Therefore, in the following we remove the vector form for conciseness. The boundary and initial conditions are given by

$$\begin{aligned} &i_s^H = -i_{app}, i_e^H = 0, N_e^H = 0 \text{ at } x = 0, \\ &i_s^H = 0, i_e^H = -i_{app} \text{ at } x = L, \\ &\Phi_s = 0, i_e^H = -i_{app}, N_e^H = -\frac{i_{app}}{F} \text{ at } x = L + L_s, \\ &c_e(x) = c_{e0} \text{ at } t = 0. \end{aligned} \tag{4-53}$$

The mechanical boundary conditions are given by

$$
\begin{aligned}
&u_x = u_y = u_z = 0 \text{ at } x = 0, \\
&\Sigma_{xx} = \Sigma_{xy} = \Sigma_{xz} = 0 \text{ at } x = L, \\
&u_y = 0 \text{ at } y = 0 \text{ and } y = W, \\
&u_z = 0 \text{ at } z = 0 \text{ and } z = H.
\end{aligned}
\tag{4-54}
$$

4.4.3 Parameters

In this work we choose $Li_xMn_2O_4$ as the cathode for two reasons. First, as a well studied material, the chemical and mechanical properties of $Li_xMn_2O_4$ are available in the literature. Second, the lithiation of $Li_xMn_2O_4$ is associated with phase transition, which can demonstrate the capability of the generalized solid diffusion equation to capture this phase transition effect. The open circuit potential and the thermodynamic factor of $Li_xMn_2O_4$ are given in Figure 4.3.

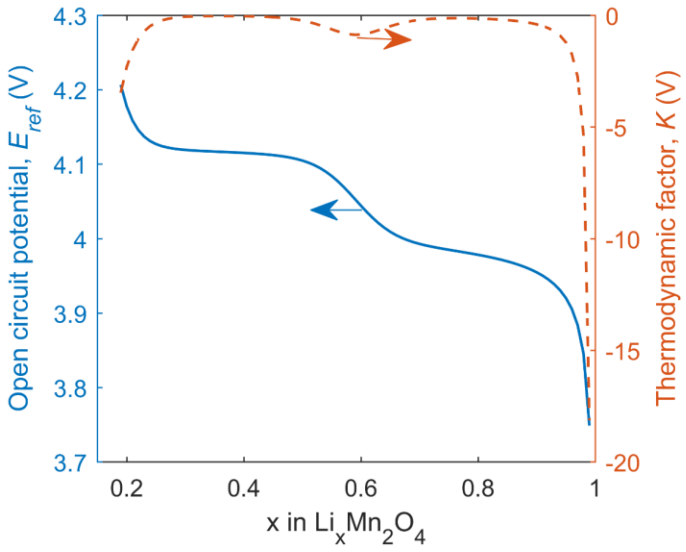

Figure 4.3. Open circuit potential and thermodynamic factor profiles of $LiMn_2O_4$.

Table 4.1 lists the input parameters for the two models. Note that different literatures may give quite different values of material parameters depending on the measurement techniques they used. Our focus is to demonstrate how the framework works so the discrepancy among measured material parameters in the literature is not of concern. Here we choose values of material

parameters that have been widely used before. With the same inputs, we compare the predictions from the two models.

Table 4.1. Input parameters for the two models

Parameter	Symbol	Value
Microscale		
Particle radius	r_p	5 μm
Diffusivity of lithium ions in solid	D_0	1×10^{-14} m^2 s^{-1}
Reaction rate constant [76]	k	5×10^{-10} $m^{2.5}$ $mol^{-0.5}$ s^{-1}
Maximum lithium concentration in solid [76]	$c_{s,max}$	24161 mol m^{-3}
Initial lithium concentration in solid [76]	c_{s0}	$0.19\,c_{s,max}$
Young's modulus of the solid particle [3]	E_p	10 GPa
Poisson's ratio of the solid particle [3]	ν_p	0.3
Lithium ion partial molar volume [3]	Ω	3.497×10^{-6} m^3 mol^{-1}
Continuum Scale		
Cathode thickness	L	52.5 μm
Cathode width	W	28.5 μm
Cathode height	H	28.5 μm
Separator thickness	L_s	17.5 μm
Initial lithium ion concentration in electrolyte	c_{e0}	1000 mol m^{-3}
Cathode porosity	ε_e	0.40
Volume fraction of active material	ε_s	0.60
Lithium ion transference number	t_+	0.38
Solid electronic conductivity [76]	κ_{s0}	10 S m^{-1}
Electrolyte conductivity [76]	κ_{e0}	1 S m^{-1}
Diffusivity of lithium ions in bulk electrolyte [76]	D_{e0}	3.23×10^{-10} m^2 s^{-1}
Temperature	T	298 K
Activity coefficient term	$1+\frac{d\ln f_{\pm}}{d\ln c_e}$	2.83
Cathodic symmetry factor	β	0.5
Mechanical cathodic symmetry factor	β_m	0.5

For the direct three-dimensional particle network model the applied current density is i_{app} =64 A m^{-2}. Note that this current density is defined based on the cross-sectional area of the solid

phase, i.e. the total cross-sectional area of all the particles that meet the current collector (the blue area in the *y*-*z* plane at *x*=0 in Figure 4.2). For the multiscale model, we keep the same amount of current passing through the electrode so that the results are comparable. Since the current density of the multiscale model is defined on the apparent cross-sectional area of the electrode, the corresponding applied current density is smaller, and the calculation gives i_{app} = 54.2 A m^{-2} for the multiscale model.

The direct multiscale model and the three-dimensional particle network model are both solved using finite element software package COMSOL Multiphysics. In terms of computational cost, the three-dimensional model takes more than 9 hour on a workstation while the multiscale model takes less than 1 hour on the same workstation.

4.5 Results and Discussion

4.5.1 Simulation Results from Multi-Scale Model

Figure 4.4(a) shows the distribution of lithium concentration inside particles at different positions along the electrode thickness. The phase transition induced concentration jump vanishes in particles closer to the separator ($x/L=1$), while still exists in particles closer to the current collector ($x/L=0$). The concentration gradient-induced stresses are shown in Figure 4.4(b) and (c). The particles with concentration jump exhibit significantly larger radial and tangential stresses. This result highlights the importance to include the phase transition effect into solid diffusion, otherwise the calculated stress will be significantly underestimated. Figure 4.4(d) shows the macroscopic stress in the electrode. Note that $\Sigma_{xx}=0$ since the electrode is free to expand in the *x* direction. Particles near the separator shows larger compression stresses of Σ_{yy} and Σ_{zz} because more lithium ions intercalate into those particles.

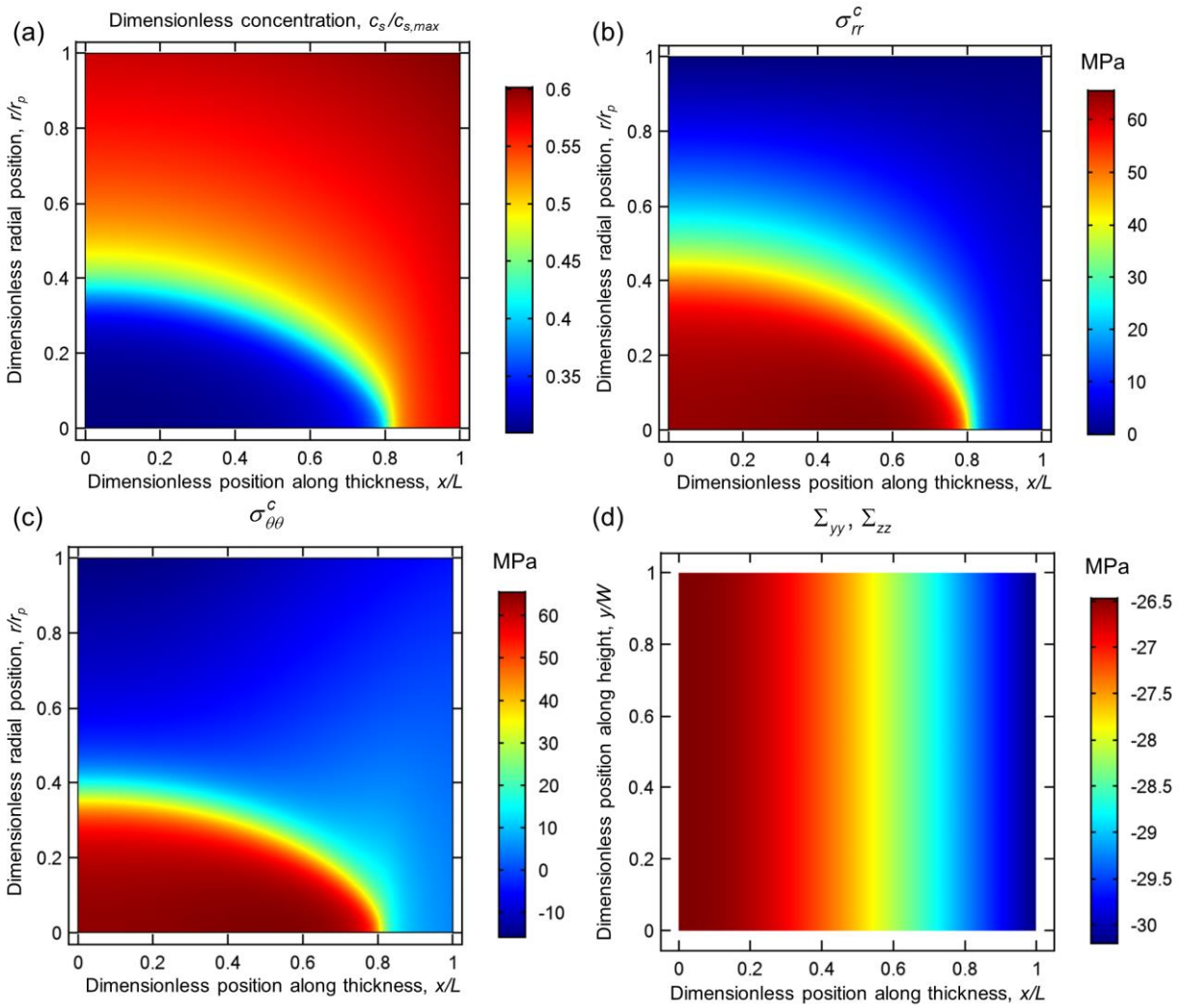

Figure 4.4. Distribution of (a) lithium concentration, (b) radial stress, and (c) tangential stress along particle radius inside all particles. In (a) – (c), the horizontal axis represents particle location along the electrode thickness direction and the vertical axis represents a point in the particle. (d) Distribution of macroscopic stress inside the electrode, where the horizontal axis represents the location along the thickness direction and the vertical axis represents the location along the width direction. All results shown are at the instant of 500 s.

In terms of temporal profiles, we choose one particle at the location of $x/L = 0.36$. As shown in Figure 4.5(a), the radial and tangential stress at the particle center ($\sigma_{rr}(r=0), \sigma_{\theta\theta}(r=0)$) peak at the time of about 500 s, while the tangential stress at the particle surface ($\sigma_{\theta\theta}(r=r_p)$) reaches its maximum magnitude at about 200 s. This time lag corresponds to the radial inward movement of the concentration jump. In contrast, Figure 4.5(b) shows that

the continuum scale stress is compressive and its magnitude gradually increases with time, as the increasing lithium concentration in the solid results in larger and larger expansion.

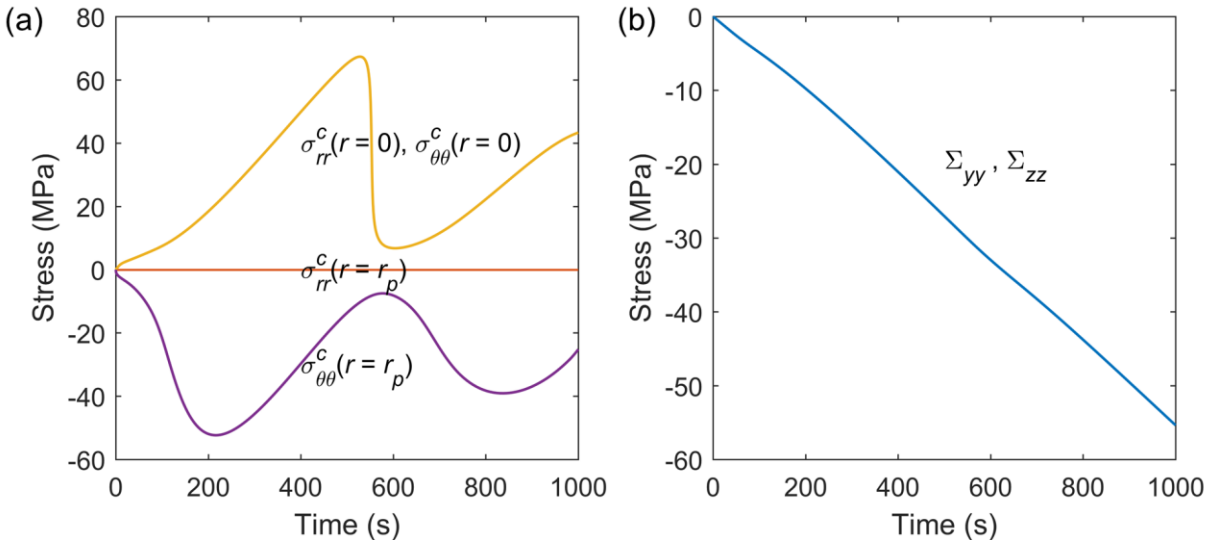

Figure 4.5. Temporal profiles of (a) concentration gradient-induced stress in a microscale particle and (b) continuum electrode scale stress at the location of $x/L=0.36$.

Figure 4.6 shows the distribution of interaction stress inside a RVE. This is obtained by modeling the local detailed particle structure in the RVE with finite element and applying the solved continuum scale stress as boundary loads. Large stress concentration shows up naturally at the contact between particles. This indicates that the detailed contact-induced local inhomogeneous stress distribution at any spatial point of interest in the electrode, if needed, can be recovered by using the solved continuum scale stress and a RVE.

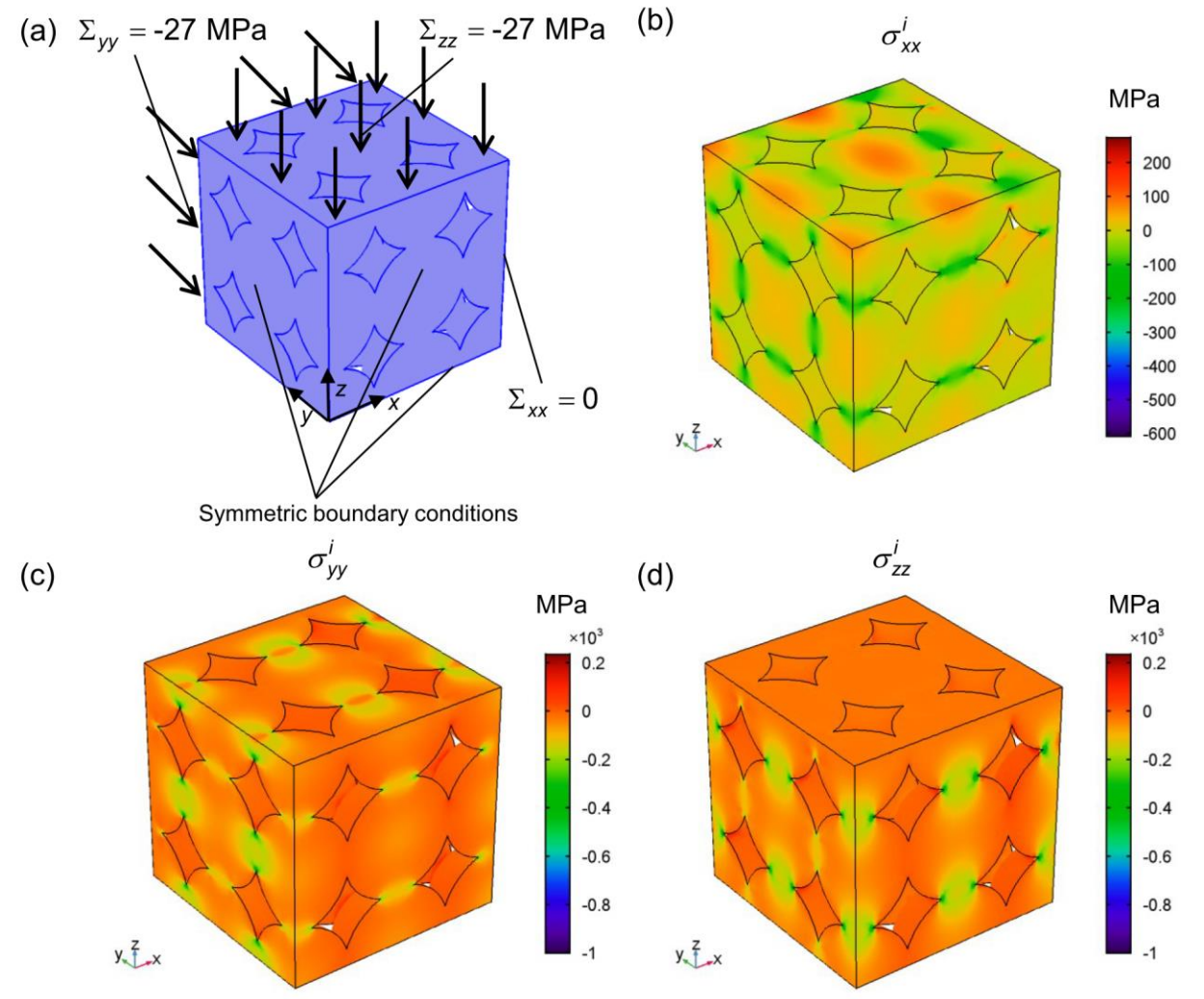

Figure 4.6. (a) Schematic of the RVE and the boundary conditions. Distribution of (b) σ^i_{xx}, (c) σ^i_{yy} and (d) σ^i_{zz} inside a RVE.

4.5.2 Simulation Results from Direct Particle Network Model

Figure 4.7(a) shows the lithium concentration distribution at the instant of 500 s. A sharp concentration jump is observed to form inside most particles, except for those near the separator. This concentration jump results from the phase transition of $Li_xMn_2O_4$ during $0.25 < x < 0.5$, which correspond to the OCP plateau of 4.15 V shown in Figure 4.3. With lithium intercalation, the concentration jump gradually moves towards particle center until vanishes. The radial locations of concentration jump at different particles thus represent the history of intercalation

current: the particles near the separator with a larger intercalation rate has finished the phase transition, while the particles near the current collector still have a moving concentration jump. Another observation is that the concentration is almost spherically symmetrical, thus the assumption of radial diffusion in the multi-scale model is reasonable.

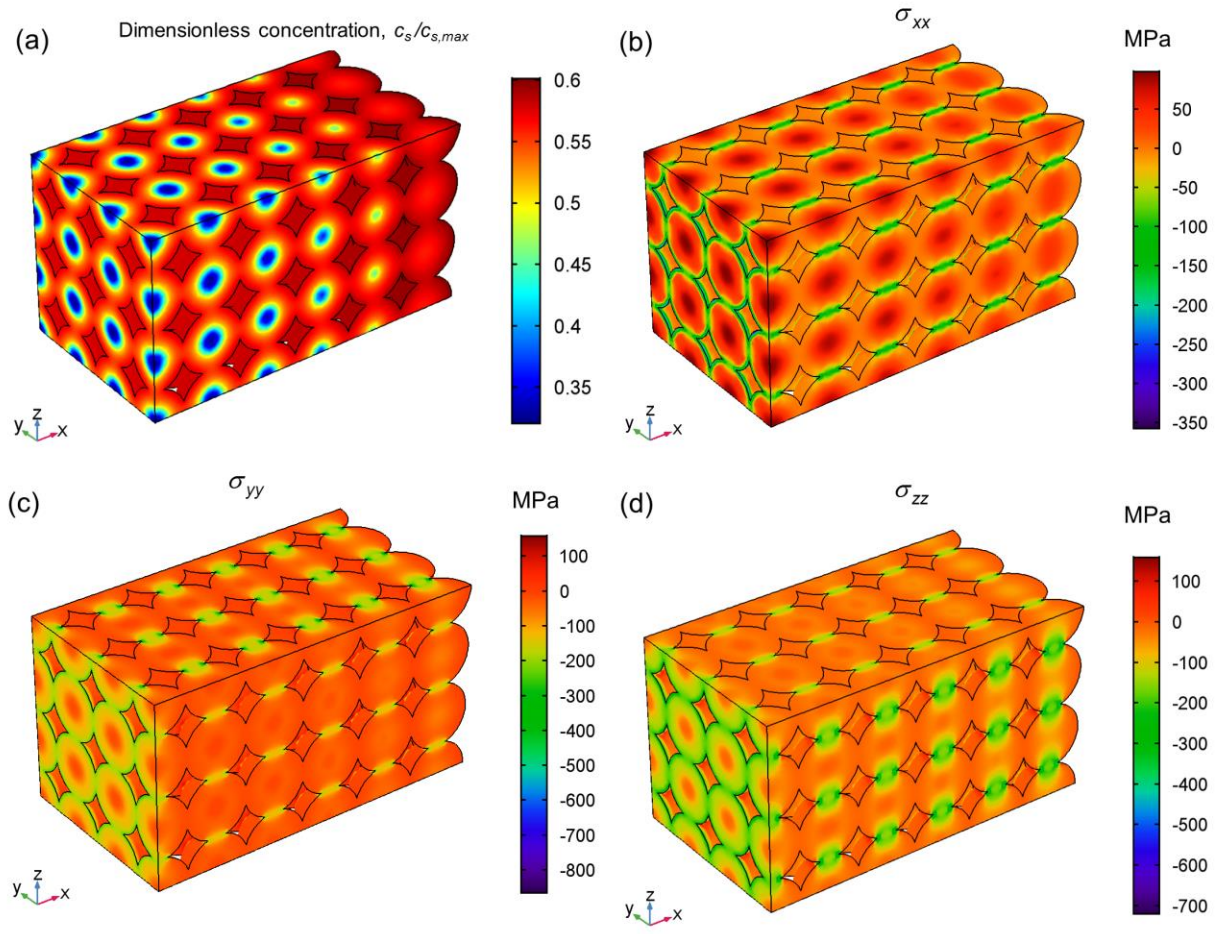

Figure 4.7. Distribution of (a) dimensionless concentration, (b) σ_{xx} (c) σ_{yy} and (d) σ_{zz} at the time instant of 500 s.

Note that the stresses in Figure 4.7(b) – (d) result from both concentration gradient in the particles and from particle interactions. At the particle center, the large tensile σ_{xx} mainly results from the effect of concentration gradient. However, σ_{yy} and σ_{zz} at the particle center turn out to

be compressive due to the constraints imposed by other particles. Large stresses appear at the particle contact regions due to stress concentration.

4.5.3 Comparison between Two Models

The direct three-dimensional particle network model can serve as the benchmark for validation of the multiscale model. This is especially valuable since it is challenging to conduct direct experimental validation against the multiscale model at present: although experimental works focusing on the measurement of deformation or strain of the electrode are available in the literature [77, 78], the direct measurement of stress distribution inside the particles remains prohibitively difficult. Comparison between the two models demonstrates that the multi-scale model can achieve good satisfying accuracy.

As the first validation, Figure 4.8 compares the simulated voltages from the two models. The comparison demonstrates the capability of the multi-scale model to predict the voltage precisely.

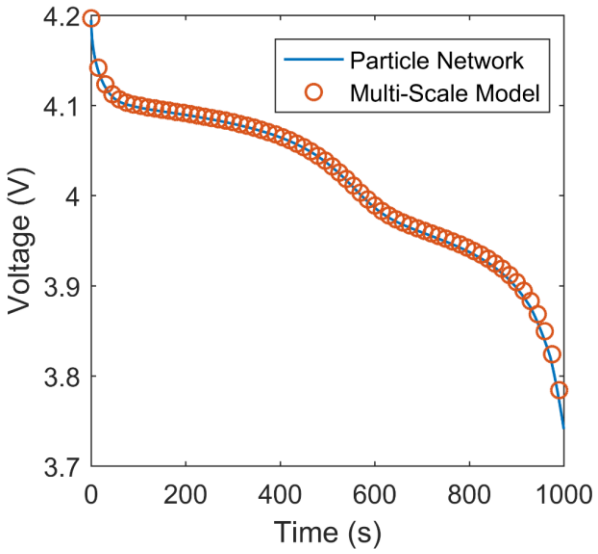

Figure 4.8. Comparison of voltages from the direct three-dimensional particle network model (shown in lines) and from the multi-scale model (shown in dots)

Figure 4.9 shows the concentration evolution inside a particle at the location of $x/L=1$. The two models agree well with each other.

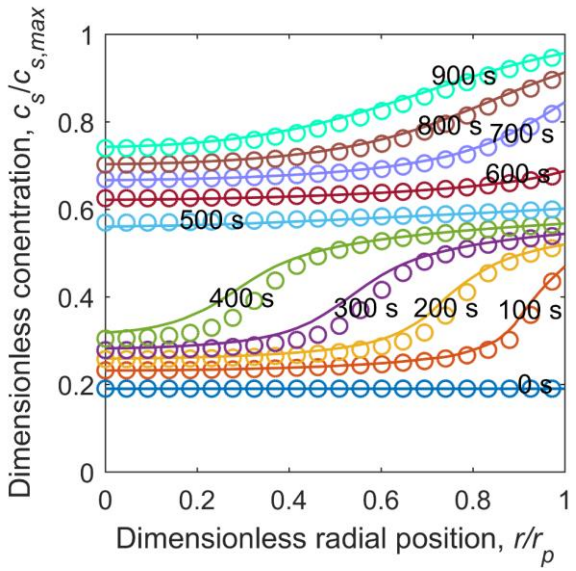

Figure 4.9. Comparison of solid dimensionless concentration from the direct three-dimensional particle network model (shown in lines) and from the multi-scale model (shown in dots).

In order to compare the stress from the direct three-dimensional particle network model and from the multi-scale model, six points are selected as listed in Table 4.2.

Table 4.2. Coordinates of points selected for stress comparison.

Point	Coordinates in direct 3D particle network model	Coordinates in multi-scale model	Coordinates in RVE model
A	$x=0.36L, y=0.33W, z=0.66H$	$x=0.36L, r=0$	$x=0, y=0, z=0$
B	$x=0.36L+0.5r_p, y=0.33W, z=0.66H$	$x=0.36L, r=0.5r_p$	$x=0.5r_p, y=0, z=0$
C	$x=0.36L, y=0.33W+0.5r_p, z=0.66H$	$x=0.36L, r=0.5r_p$	$x=0, y=0.5r_p, z=0$
D	$x=0.36L, y=0.33W, z=0.66H+0.5r_p$	$x=0.36L, r=0.5r_p$	$x=0, y=0, z=0.5r_p$
E	$x=0.36L+r_p, y=0.33W, z=0.66H$	$x=0.36L, r=r_p$	$x=r_p, y=0, z=0$
F	$x=0.36L, y=0.33W, z=0.66H+r_p$	$x=0.36L, r=r_p$	$x=0, y=0, z=r_p$

Four points are inside a particle at the location of $x/L=0.36$. Point A is at the particle center, Points B, C, D are $0.5r_p$ away from Point A along the *x*, *y* and *z* axes, respectively. Points E and F are at r_p away from Point A along the *x* and *z* axes, respectively.

The stress from the direct three-dimensional particle network model is shown in solid line in Fig. 10. To compare these results with the results from the multi-scale model, we first transform the radial and tangential stress (σ_{rr}^c and $\sigma_{\theta\theta}^c$) obtained from the multi-scale model to σ_{xx}^c, σ_{yy}^c and σ_{zz}^c. The coordinate relation is shown in Table 4.3.

Table 4.3. The coordinate relation between σ_{xx}^c, σ_{yy}^c, σ_{zz}^c and σ_{rr}^c, $\sigma_{\theta\theta}^c$ for concentration gradient-induced stress in a particle from the multiscale model.

	σ_{xx}^c	σ_{yy}^c	σ_{zz}^c
Point A	$\sigma_{rr}^c(r=0)$	$\sigma_{rr}^c(r=0)$	$\sigma_{rr}^c(r=0)$
Point B	$\sigma_{rr}^c(r=0.5r_p)$	$\sigma_{\theta\theta}^c(r=0.5r_p)$	$\sigma_{\theta\theta}^c(r=0.5r_p)$
Point C	$\sigma_{\theta\theta}^c(r=0.5r_p)$	$\sigma_{rr}^c(r=0.5r_p)$	$\sigma_{\theta\theta}^c(r=0.5r_p)$
Point D	$\sigma_{\theta\theta}^c(r=0.5r_p)$	$\sigma_{\theta\theta}^c(r=0.5r_p)$	$\sigma_{rr}^c(r=0.5r_p)$
Point E	$\sigma_{rr}^c(r=r_p)=0$	$\sigma_{\theta\theta}^c(r=r_p)$	$\sigma_{\theta\theta}^c(r=r_p)$
Point F	$\sigma_{\theta\theta}^c(r=r_p)$	$\sigma_{\theta\theta}^c(r=r_p)$	$\sigma_{rr}^c(r=r_p)=0$

Next, we use the calculated inhomogeneous σ_{ij}^i in the RVE shown in Figure 4.6, which has been listed in Table 4.4, to account for the particle interaction effect. Our purpose is to see whether the stress distribution recovered with RVE can correctly capture the local inhomogeneous stress state. For a given RVE, σ_{ij}^i linearly depends on the loads Σ_{yy} and Σ_{zz}. Thus, the temporal profile of σ_{ij}^i at any point in the particle can be determined by scaling linearly with the temporal profile of Σ_{yy} and Σ_{zz} as shown in Figure 4.5(b).

Table 4.4. Interaction stress in the RVE under the boundary loads of $\Sigma_{xx}=0$, $\Sigma_{yy}=\Sigma_{zz}=-27$ MPa

	σ^i_{xx}	σ^i_{yy}	σ^i_{zz}
Point A	31.9 MPa	-55.2 MPa	-55.4 MPa
Point B	14.1 MPa	-26.3 MPa	-27.0 MPa
Point C	21.3 MPa	-111.2 MPa	-34.2 MPa
Point D	21.5 MPa	-33.4 MPa	-111.1 MPa
Point E	1.8 MPa	3.3 MPa	3.4 MPa
Point F	-73.9 MPa	-102.6 MPa	-143.1 MPa

The total stress based on the multi-scale model is given as $\sigma^c_{ij}+\sigma^i_{ij}$. Figure 4.10 compares the results from the direct three-dimensional particle network model and from the multi-scale model, which shows good agreement at all points.

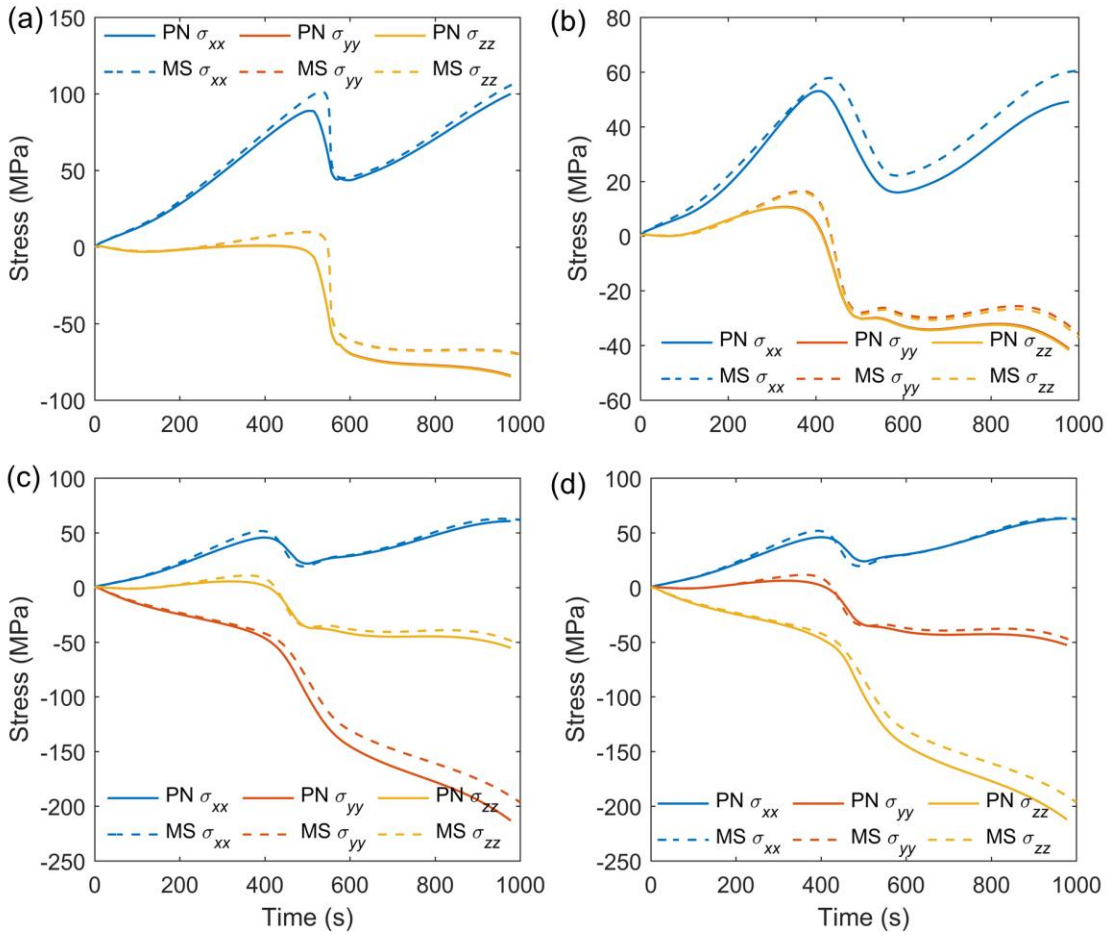

Figure 4.10. Comparison of stress from the direct three-dimensional particle network model (shown in solid lines, PN) and from the multi-scale model (shown in dash lines, MS) at (a) Point A, (b) Point B, (c) Point C and (d) Point D.

4.5.4 Limitations of the Multi-Scale Model

An important assumption of the multi-scale model is the spherically symmetrical concentration distribution at the microscopic particle scale. This assumption is generally justified by the direct three-dimensional particle network simulation results shown in Figure 4.7(a). However, a closer investigation shows that this assumption may not be valid in the particle contact regions. As shown in Figure 4.11(a), the concentration at the Points E and F differ from that at the solid electrolyte interface. At 300 s, the phase transition induced concentration jump starts to emerge on the particle surface. Without exposure to the electrolyte, the particle overlapping region does now allow direct intercalation of lithium ions from the electrolyte at Points E and F: it has to wait for the relatively slow solid diffusion to become lithiated. However, the solid diffusion is associated with a rather sharp concentration jump, thus Points E and F exhibit significantly different concentration than other particle surface points. When the concentration jump moves inside the particles at 500 s, the electrode shows a spherically symmetrical distribution of concentration surrounding each particle as in Figure 4.11(b). This mechanism cannot be captured by the multi-scale model which does not consider detailed particle structure: all surface points of particles, including Points E and F, are considered to be directly exposed to the electrolyte.

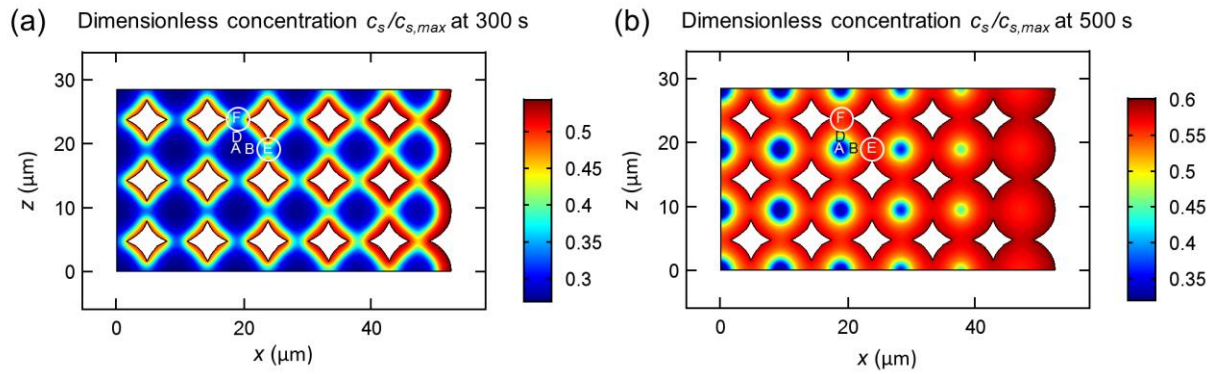

Figure 4.11. Distribution of lithium concentration in particles at (a) 300 s and (b) 500 s from the direct three-dimensional particle network simulation. The two-dimensional slice is at y=0.33W in Fig. 2.

The asymmetrical concentration distribution shown in Figure 4.11(a) leads to a difference of stress predicted with the two models, as shown in Figure 4.12. To understand the mechanical effect of large local concentration gradient at Points E and F, we can treat these two points as if they are at the centers of two small virtual "particles" noted by the white circles in Figure 4.11. At 300 s, Points E and F undergo tensile stress because the outer parts of "particles" have much larger lithium concentration. This explains why the solid lines are higher than their dash line counterparts at 300 s in Figure 4.12. In addition, the gap between two corresponding lines for each stress component is similar at 300 s, because the stress due to local concentration gradient at the "particle" center is almost hydrostatic. The two models agree well with each other at 500 s, as shown in Figure 4.11(b), because by now the inhomogeneous concentration distribution on a particle surface between the particle contact regions and no contact regions has vanished.

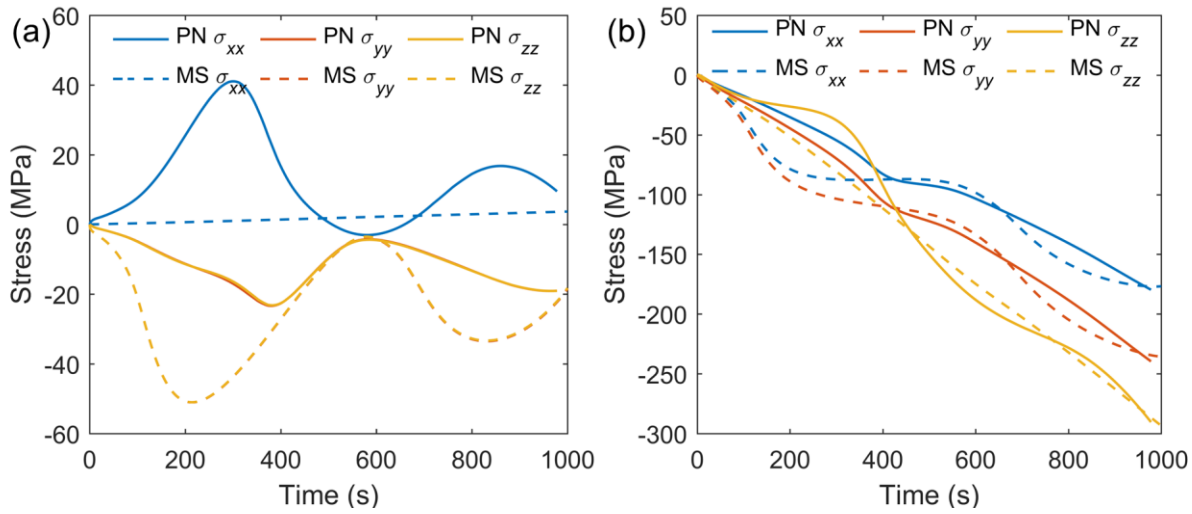

Figure 4.12. Comparison of stress from the direct three-dimensional particle network model (shown in solid lines, PN) and from the multi-scale model (shown in dash lines, MS) at (a) Point E and (b) Point F.

We also note that the two models agree better at Point F than at Point E. As there is no constraint for the electrode expansion along the *x* direction, the particle interaction stress σ_{ij}^{i} is much smaller at Point E than at Point F, which can be seen in Table 4.4. Thus, the stress at Point E depends more on the concentration in the particle. The multiscale model captures the intra-particle concentration gradient-induced stress σ_{ij}^{c} but does not address any asymmetrical inter-particle concentration distribution. In contrast, the stress at Point F can be predicted well using our multiscale model except for the times when phase transition induces inter-particle concentration gradient.

4.6 Conclusions

We have developed two models, a multi-scale model and a direct three-dimensional particle network model, to fully couples mechanics and electrochemistry consistently at both micro and continuum scales.

The pseudo-2D model based on porous electrode theory is widely used in the field of electrochemistry due to its efficiency and predicting capability without the need to directly model detailed particle configurations. The multi-scale model developed in this work offers similar advantage. The electrochemical part of the multiscale model is consistent with the pseudo-2D model with several important revisions. First, we extend the solid diffusion equation using the OCP curve and its derived thermodynamic factor to account for the phase transition effect. This revision is important since the phase transition can lead to large concentration gradient inside the particle, which further results in large concentration gradient induced-stress. Second, we include the effect of stress on the electrochemical reaction kinetics in addition to the stress effect on solid diffusion, which fully couples electrochemical and mechanical behaviors. The mechanical stress in the particle is described by the superposition of concentration gradient-induced stress and particle interaction stress. The concentration gradient-induced stress is given by the solid concentration profile while the particle interaction stress is captured by the continuum scale stress. The detailed information such as local contact stress concentration can be recovered by performing a RVE calculation of a representative particle structure with the continuum scale stress at the boundary loads.

In this chapter we considered uniform particle size as an example to demonstrate the multiscale model. One can readily consider a distribution of particle sizes along the electrode thickness by taking $r_p = r_p(x)$ instead of a constant r_p, or extend to three dimensional distribution. One can also address locally mixed particle sizes, e.g. using a mixture of two sizes of particles for the electrode, by considering two representative particles. The equations for each particle are the same as shown in this work, except that the homogenization should be taken over the two particles to connect particle scale quantities such as stress and intercalation current

density to the continuum scale equations. We expect that such a mixed particle system will demonstrate rich behaviors. For instance, smaller particles may intercalate and swell faster than larger particles in the same region. This will change the stress state of surrounding neighbors in a manner different than uniform simultaneous swelling of particles with the same size. In this work we considered particles to be spherical, which is a reasonable representation of the shape of many active material particles. It is possible to engineer particles into other geometries such as disc or rod shapes. In such cases, one can consider ellipsoidal particles and use the orientation distribution function to describe their orientations. A distinct effect is that if the orientation distribution is not random, the active material will exhibit anisotropic reaction rates and interactions in the electrode.

The three-dimensional particle network model directly models the particle network explicitly using fully coupled electrochemical-mechanical equations. This model can be applied to arbitrary particle geometries and networks, but is associated with high computational cost. Using the three-dimensional particle network model as a benchmark, we validate the accuracy of the multi-scale model. The comparison shows that the two models agree well in both the electrochemical behaviors and the local stress distribution, which demonstrates the capability of the multiscale model in predicting coupled electrochemical-mechanical behaviors. Deviation from the three-dimensional particle network model occurs only when the concentration in the particle is highly different from spherical symmetry. In other words, the multiscale model can be applied to all situations where the standard pseudo-2D electrochemical model is applicable.

We envision that the multi-scale model can be used to address various coupled mechanical-electrochemical problems at continuum scale such as cracking in-between particles, delamination of the electrode from the current collector, and evaluation of the impact of fracture

and other defects on battery performance. The three-dimensional particle network model allows studying coupled processes related to particle network details, such as particle shape and size distribution on battery performance, intra-particle fracture in inhomogeneous environment, and deboning of individual particles from the network.

Chapter 5 Design of Lithium-Ion Batteries Using Artificial Neural Networks

5.1 Introduction

Lithium-ion batteries have been widely used in various applications, ranging from consumer electronics to electric vehicles. To satisfy the ever-growing demands for higher energy and power capability, durability and safety of batteries, the design of lithium-ion batteries has become essential to avoid any unexpected loss of performance. Battery design based on experiments is time-consuming and expensive. In contrast, simulation-based design is not only more efficient, but also provides deeper insights into the mechanisms governing the battery performance.

Serving as a crucial step for simulation-based design, battery modeling has attracted a growing interest. The majority of current battery models are based on the pseudo two-dimensional (P2D) electrochemical model, which is based on the porous electrode theory [65]. The P2D model have been used to optimize the cathode and anode thickness, porosity, particle size and many other important electrode parameters [79-81].

The lithium-ion battery is inherently a multi-physical system. A representative example showing its multi-physical nature is the interplay between electrochemical and thermal behaviors. Heat generated by electrochemical reactions alters the temperature distribution of the electrode, which successively affects the electrochemical processes. Note that many properties of battery components, such as the electrolyte diffusivity and conductivity, are strongly related to temperature [82]. Thus, an accurate simulation often requires a thermal model to be coupled with

the P2D model. In order to appropriately address the thermal effect, researchers have contributed in thermal property characterization [83], heat generation rate measurement [84] and thermo-electrochemical coupled modeling [85-87].

Despite the significant progress in the thermo-electrochemical coupled modeling of lithium-ion batteries, there remains a large gap between modeling and simulation-based design. The computational cost can be prohibitively expensive if a fully coupled thermo-electrochemical model is directly applied for battery design. In simulation-based battery design, thousands of simulations are often required to determine the optimal design variables. Moreover, the complex non-linear nature of the battery model may result in convergence issues under some sets of design variables. Besides, sensitivity analysis of the design variables is also difficult to perform due to the very high computational cost. Without sensitivity analysis the possible reduction of design space through eliminating insensitive design variables becomes inapplicable.

Recently, artificial neural networks (ANN, also termed as neural networks when there is no ambiguity) has been shown to solve complex non-linear problems. A notable example is the application of deep neural networks in the state-of-the-art artificial intelligence of Go [88]. Loosely analogous to biological neuron systems, ANN is a computational model that consists of a large collection of connected artificial neurons. The neurons and their connections can be trained with data to represent the relations between inputs and outputs. Compared with the physical modeling, ANN has advantages in predicting the output without the knowledge of the exact analytic information of the modeled system. Another major benefit of ANN is its computational efficiency, which enables its deployment in real time applications. ANN has been extensively used in computer sciences, finance, engineering and many other fields. In the battery field the neural network approach has been explored for state of charge estimations [89, 90].

However, ANN has not received enough attention for battery design applications. Considering the potential of ANN in handling highly nonlinear complex problems with significant computational cost, we propose an approach to combine the strengths of physical modeling and ANN.

The objective of this chapter is to present a method of applying the neural network in simulation-based battery design. Using the simulation results from the electrochemical-thermal model as training data, we obtained two neural networks with satisfied accuracy. The first neural network, acted as a classifier, is used to predict whether a set of input variables is physically feasible. The second neural network is used to calculate the specific energy and specific power for any given set of input variables. These two trained neural networks are used to perform very large scale Monte Carlo simulations, which are computationally too expensive to be achievable using the finite element method (FEM). The analysis of Monte Carlo simulation results provides many important insights on the battery design. In this work, we firstly demonstrate that this neural network can be used to generate the Ragone plot, which is an important characteristic curve for electrochemical devices. Secondly, global sensitivity analysis based on the Monte Carlo simulation results provides a sensitivity ranking of the input variables on specific energy and specific power. This ranking is helpful to identify the limiting process inside the battery, thus reduce the design space. The sensitivity analysis can also contributes to understand the influence of input inaccuracy on the outputs, thus determining the acceptable inaccuracy range for each input parameter. Finally, we characterize the battery performance with respect to most sensitive parameters, and generate a design map to satisfy the requirements of both specific energy and specific power.

5.2 Methodology

The first step to construct a neural network is to determine the inputs and outputs. In this work, we are particularly interested in design variables that can be controlled in battery manufacturing. As the two most important battery performance indicators, specific energy and specific power are selected as outputs. Once the input variables are determined, we samples representative sets of variables using the design of experiments (DOE) algorithms. Using the sampled variables as inputs, a thermo-electrochemical finite element model is run to give specific energy and specific power. The inputs and associated outputs are utilized to train the neural network. In order to validate the neural network, predictions from the finite element simulation and neural network are compared. Once the artificial neural network is constructed with satisfied accuracy, Monte Carlo simulations are performed for further analysis, such as the global sensitivity analysis and optimization.

5.2.1 Electrochemical and Thermal Modeling

We use the P2D model, as listed in Table 5.1, to resolve the solid concentration in the particle domain (the coordinate along particle radius is denoted as r), and the electrolyte concentration, electrolyte potential and solid potential in the electrode domain (the coordinate along electrode thickness is denoted as x). We denote the thickness of the negative electrode as L_n, the thickness of the separator as L_s, and the thickness of the positive electrode as L. The negative electrode, the separator and the positive electrode occupy the regions of $0 \le x \le L_n$, $L_n \le x \le L_n + L_s$, and $L_n + L_s \le x \le L_n + L_s + L$, respectively.

Table 5.1. Governing equations and boundary conditions of the electrochemical model

Domain	Governing Equations	Boundary and Initial Conditions
Particle	$\frac{\partial c_s}{\partial t} = \frac{D_s}{r^2}\frac{\partial}{\partial r}\left(r^2 \frac{\partial c_s}{\partial r}\right)$	$r=0: \frac{\partial c_s}{\partial r}=0;\ r=r_p: D_s \frac{\partial c_s}{\partial r} = -\frac{i}{F}$ $t=0: c_s = c_{s0}$
Electrode	$\frac{\partial}{\partial x}\left(\sigma_s^{eff} \frac{\partial \Phi_s}{\partial x}\right) - a_s i = 0$	$x=0: \Phi_s = 0;\ x=L_n: \frac{\partial \Phi_s}{\partial x}=0;$ $x=L_n+L_s: \frac{\partial \Phi_s}{\partial x}=0;\ x=L_n+L_s+L: \sigma_s^{eff}\frac{\partial \Phi_s}{\partial x} = -i_{app}.$
	$\frac{\partial}{\partial x}\left(\kappa_e^{eff} \frac{\partial \Phi_e}{\partial x} + \kappa_D^{eff} \frac{\partial \ln c_e}{\partial x}\right) + a_s i = 0$ where $\kappa_D^{eff} = -\frac{2RT\kappa_e^{eff}}{F}\left(1+\frac{d\ln f_{\pm}}{d\ln c_e}\right)(1-t_+)$	$x=0: \frac{\partial \Phi_e}{\partial x}=0;\ x=L_n+L_s+L: \frac{\partial \Phi_e}{\partial x}=0.$
	$\varepsilon_e \frac{\partial c_e}{\partial t} = \frac{\partial}{\partial x}\left(D_e^{eff} \frac{\partial c_e}{\partial x}\right) + \frac{(1-t_+)}{F} a_s i$	$x=0: \frac{\partial c_e}{\partial x}=0; x=L_n+L_s+L: \frac{\partial c_e}{\partial x}=0.$ $t=0: c_e = c_0$

In Table 5.1, c_s is the lithium concentration in the solid (mol L^{-1}), D_s is the lithium diffusivity in the solid (m^2 s^{-1}), r_p is particle radius (m), F is the Faraday constant (C mol^{-1}), i is the intercalation current per unit area (A m^{-2}), c_{s0} is the initial lithium concentration in the solid (mol L^{-1}), σ_s^{eff} is the effective solid conductivity (S m^{-1}), Φ_s is the potential in the solid (V), a_s is the active surface area per unit electrode volume (m^{-3}), i_{app} is the applied current density to the electrode (A m^{-2}) with the sign defined as $i_{app} > 0$ for discharge, κ_e^{eff} is the effective electrolyte conductivity (S m^{-1}), Φ_e is the potential in the electrolyte (V), R is the gas constant (J K^{-1} mol^{-1}), T is temperature (K), $f_{\pm}$ is the electrolyte activity coefficient, t_+ is the lithium ion transference number, ε_e is the electrolyte volume fraction, c_e is the lithium concentration in the electrolyte (mol L^{-1}), D_e^{eff} is the effective electrolyte diffusivity (m^2 s^{-1}) and c_0 is the initial lithium concentration in the electrolyte (mol L^{-1}).

The intercalation current density, i (A m^{-2}), is zero in the separator region. In the negative and positive electrode regions the current density is given by the Butler-Volmer equation,

$$i = i_0\left(\exp\left(\frac{\beta F\eta}{RT}\right) - \exp\left(-\frac{(1-\beta)F\eta}{RT}\right)\right), \tag{5-1}$$

where i_0 is the exchange current density (A m^{-2}), β is the anodic charge transfer coefficient, and η is the over-potential (V) defined as

$$\eta = \Phi_s - \Phi_e - U(c_{s,\text{surf}}), \tag{5-2}$$

where U is the open circuit potential (V) which depends on the lithium concentration at the particle surface, $c_{s,\text{surf}}$ (mol L^{-1}). The exchange current density is given by

$$i_0 = Fkc_{s,\text{surf}}^{1-\beta}c_e^{\beta}\left(c_{s,\max} - c_{s,\text{surf}}\right)^{\beta}, \tag{5-3}$$

where k is the reaction rate constant (m$^{1+3\beta}$ mol$^{-\beta}$ s^{-1}) and $c_{s,\max}$ is the maximum lithium concentration in the particle (mol L^{-1}). The reaction rate constant k is assumed to follow an Arrhenius temperature-dependent relation,

$$k = k_0\exp\left[\frac{E_{\text{act},k}}{R}\left(\frac{1}{T_0} - \frac{1}{T}\right)\right], \tag{5-4}$$

where $E_{\text{act},k}$ is the activation energy (kJ mol^{-1}) for k, and the subscript 0 denotes values at the reference state.

In Table 5.1, the active surface area per unit electrode volume (m^{-1}) is given by $a_s = 3\varepsilon / r_p$, where ε is the solid volume fraction. The effective solid conductivity, effective electrolyte diffusivity and effective electrolyte conductivity are given as

$$\sigma_s^{eff} = \sigma_s\frac{\varepsilon}{\tau}, \quad D_e^{eff} = D_e\frac{\varepsilon_e}{\tau_e}, \quad \kappa_e^{eff} = \kappa_e\frac{\varepsilon_e}{\tau_e}, \tag{5-5}$$

where σ_s is the solid bulk conductivity (S m^{-1}), τ is the solid tortuosity, D_e and κ_e are the bulk electrolyte diffusivity (m^2 s^{-1}) and conductivity (S m^{-1}), ε_e is the electrolyte volume fraction and τ_e is the electrolyte tortuosity. The tortuosity of the solid and the electrolyte are given by the Bruggeman relation,

$$\tau = \varepsilon^{1-\alpha}, \quad \tau_e = \varepsilon_e^{1-\alpha}, \tag{5-6}$$

where α is the Bruggeman constant. Typically, α is set as 1.5 in battery simulations. However, recent reports [91-93] reveal that α may have different values. In this work, we will investigate the effect of α on battery performance. The electrolyte bulk conductivity and diffusivity are functions of temperature and concentration, which are adopted from Ref. [82].

As the reaction constant, the electrolyte diffusivity and conductivity depend on temperature, accurate modeling requires a full coupling of thermal and electrochemical behaviors. The temperature of the electrode is governed by

$$\rho C_p \frac{\partial T}{\partial t} = K \frac{\partial^2 T}{\partial x^2} + q, \tag{5-7}$$

where ρ is the density (kg m^{-3}), C_p is the specific heat capacity (J kg^{-1} K^{-1}), K is the thermal conductivity (W m^{-1} K^{-1}), and the heat generation rate q (W m^{-3}) is given by

$$q = a_s i\left(\Phi_s - \Phi_e - U\right) + a_s i T \frac{\partial U}{\partial T} + \sigma_s^{eff}\left(\frac{\partial \Phi_s}{\partial x}\right)^2 + \kappa_e^{eff}\left(\frac{\partial \Phi_e}{\partial x}\right)^2 + \kappa_D^{eff}\left(\frac{\partial \ln c_e}{\partial x}\right)\left(\frac{\partial \Phi_e}{\partial x}\right). \tag{5-8}$$

The thermal boundary condition is given by

$$\begin{aligned} K\frac{\partial T}{\partial x} &= h(T - T_0) \ \text{ at } x = 0, \\ -K\frac{\partial T}{\partial x} &= h(T - T_0) \ \text{ at } x = L_n + L_s + L, \end{aligned} \tag{5-9}$$

where T_0 is the environmental temperature (K) as well as the initial temperature of the cell setting at 25°C, and h is the heat convection coefficient (W m^{-2} K^{-1}). We implemented the thermo-electrochemical model using the finite element software package COMSOL

5.2.2 Inputs

The first step in design optimization is to determine the appropriate input variables and their ranges. In this work, our focus lies on the variables that are controllable during battery manufacturing. Specifically, this work is focused on the positive electrode. The inherent properties, such as diffusivity and conductivity, are constants for a given material. The positive electrode thickness, positive solid phase volume fraction, positive Bruggeman constant and positive active material particle radius and C-rate are chosen as the input variables.

Among all the design variables, the electrode thickness, solid phase volume fraction and particle radius are easy to control in battery manufacturing. The initial electrolyte concentration is another important and tunable variable. Generally, this variable is set as 1 mol L^{-1}, where the maximum conductivity can be reached [94]. However, this concentration may lead to local electrolyte dry-up, which may decrease available energy or even accelerate capacity degradation. This effect has been found in both simulations and experiments [95], highlighting the benefits of high initial concentration. In this work, we prescribe three levels of initial electrolyte concentrations to explore the effect of initial electrolyte concentration.

The Bruggeman constant is not a directly controllable variable. Physically, the tortuosity of two electrodes can be different even when the volume fraction is the same. The Bruggeman constant can be regarded as a variable characterizing the electrode microstructure. In addition, while most prior studies assume that this constant is 1.5, we are interested in whether this assumption has a major influence on the simulation results.

The applied C-rate, although an operational variable rather than a design variable, is also selected as an input variable. The primary reason is that the battery performance is usually evaluated at several C-rates. Thus, the neural network should provide the capability to adjust the C-rate. The applied C-rate can be related to the current density by

$$i_{app} = \text{C-rate} \times L\varepsilon Q_p \ , \tag{5-10}$$

where Q_p is the volumetric capacity of the positive electrode active material.

Table 5.2 lists the 6 design variables and their ranges. After determining the design variables, 900 sets of design-of-experiment variables are generated based on the Latin hypercube design (LHD) algorithm and the face centered composite design (FCCD) algorithm [96].

Table 5.2. Design variables and their ranges

Variable	Symbol (Unit)	Range
Positive electrode thickness	L (μm)	50~130
Positive solid phase volume fraction	ε	0.5~0.8
Positive Bruggeman constant	α	1.5~2.0
Positive active material particle radius	r_p (μm)	3 ~ 12
Electrolyte Li^+ concentration	c_0 (mol L^{-1})	0.8, 1, 1.2
Applied C-rate	C-rate (h^{-1})	C/2, 1C, 3C

In this work, the positive electrode is $Li_xNi_{1/3}Co_{1/3}Mn_{1/3}O_2$ (NCM) and the negative electrode is Li_xC_6. The capacity ratio of the negative electrode over the positive electrode, R_{np}, is kept at a constant of 1.05. A ratio slightly larger than 1 is chosen in order to ensure the full utilization of the more expensive positive electrode active material, as well as to avoid overlithiation and lithium plating.

$$R_{np} = \frac{Q_n L_n \varepsilon_n}{Q_p L \varepsilon} = 1.05, \tag{5-11}$$

where Q_n is the volumetric capacity of the negative electrode active material and ε_n is the volume fraction of the negative electrode active material. Given L and ε, the thickness and solid volume fraction of the negative electrode are given as

$$L_n = L/1.15, \quad \varepsilon_n = \varepsilon/1.086. \tag{5-12}$$

Table 5.3 lists the parameters for the electrochemical-thermal model.

Table 5.3. Input parameters for the coupled electrochemical-thermal model

Parameters (Unit)	Positive electrode	Negative electrode	Separator	Entire cell
Dimensional & microstructural parameters				
Thickness (μm)	L	L/1.15	20	–
Solid phase volume fraction	ε	ε/1.086	0.61	–
Bruggeman constant	α	α	2.6	–
Particle radius (μm)	r_p	8	–	
Cell projected area, A (m^2)	–	–	–	0.01
Thermodynamic parameters				
Volumetric capacity, Q_p, Q_n (A h m^{-3})	561.5	736.4		
Open circuit voltage, U (V)	Ref. [97]	Ref. [98]		
Entropy coefficient, $\partial U/\partial T$ (V K^{-1})	Ref. [99]	Ref. [98]		
Transport parameters				
Solid diffusivity, D_s (m^2 s^{-1})	1×10^{-13}	1×10^{-13}	–	–
Solid electrical conductivity, σ_s (S m^{-1})	0.1	100	–	–
Electrolyte diffusivity, D_e (m^2 s^{-1})	Function of T and c_e, cited from Ref. [82]			
Electrolyte conductivity, κ_e (S m^{-1})	Function of T and c_e, cited from Ref. [82]			
Mean molar activity, $1+\frac{d\ln f_{\pm}}{d\ln c_e}$	Function of T and c_e, cited from Ref. [82]			
Kinetic parameters				
Reaction rate constant at 25°C, k_0 ($m^{2.5}$ $mol^{-0.5}$ s^{-1})	6.15×10^{-11}	6.15×10^{-11}	–	–
Reaction activation energy, $E_{act,k}$ (kJ mol^{-1})	30	30	–	–
Anodic charge transfer coefficient, β	0.5	0.5	–	–
Thermal parameters				
Specific heat capacity, C_p (J kg^{-1} K^{-1})	900	1437	1978	–
Thermal conductivity, K (W m^{-1} K^{-1})	5	5	1	–
Heat convection coefficient, h (W m^{-2} K^{-1})	–	–	–	5

5.2.3 Outputs

The objective functions of the simulation-based design involve specific energy and specific power, which are defined as

$$E = \frac{\int_0^{t_d} IVdt}{m} \; ; \tag{5-13}$$

$$P = \frac{\int_0^{t_d} IVdt}{mt_d} \; , \tag{5-14}$$

where $I = i_{app} A$ is the applied discharge current, A is the cell projected area given in Table 5.3, V is the voltage profile given by the finite element simulation, t_d is the discharge time when V hits the low voltage threshold of 2.5 V, and m is the cell mass.

The cell mass is the sum of the current collectors, separator and electrodes,

$$m = A\left(\rho_{\mathrm{Al}} d_{\mathrm{Al}} + \sum_{i \in \mathrm{pos}} \rho_i \varepsilon_i d_{\mathrm{pos}} + \sum_{i \in \mathrm{sep}} \rho_i \varepsilon_i d_{\mathrm{sep}} + \sum_{i \in \mathrm{neg}} \rho_i \varepsilon_i d_{\mathrm{neg}} + \rho_{\mathrm{Cu}} d_{\mathrm{Cu}} \right), \tag{5-15}$$

where ρ is the density, d is the thickness and ε is the volume fraction. As the positive electrode consists of active particles, electrolyte, binder and additives, the mass of the positive electrode is the sum of those phases. The summation also applies for the separator and the negative electrode. The parameters needed in Eq. (5-15) are listed in Table 5.4.

Table 5.4. Density, volume fraction and thickness of the components inside the battery

	Density	Volume fraction	Thickness
Al current collector	2707 kg m^{-3}	1	25 μm
Positive electrode			
Active particle (NCM)	4210 kg m^{-3}	ε	
Binder and additive	1800 kg m^{-3}	0.1	L
Electrolyte	1324 kg m^{-3}	1-0.1- ε	
Separator			
PP	855 kg m^{-3}	0.61	20 μm
Electrolyte	1324 kg m^{-3}	0.39	
Negative electrode			
Active particle (LiC_6)	2260 kg m^{-3}	ε/1.086	
Binder and additive	1800 kg m^{-3}	0.1	L/1.15
Electrolyte	1324 kg m^{-3}	1-0.1- ε/1.086	
Cu current collector	8954 kg m^{-3}	1	25 μm

5.2.4 Neural Network Construction

The simulation results from the electrochemical and thermal modeling provide the training data to construct neural network that correlate the inputs and outputs. Physically, some sets of inputs may lead to "abnormal" outputs, such as significantly low specific energy because of local depletion of electrolyte, which prevents lithium transport. The "abnormal" results occur when the combination of input parameters are outside of the range for sustaining intercalation or deintercalation. The accuracy of neural network in calculating outputs will be diminished if the training data contain those "abnormal" results since they cause a sharp discontinuity of system behavior. Our solution to this problem is to introduce another neural network, which acts as a *classifier* to judge whether a set of inputs is normal or abnormal. The *calculator* neural network performs calculation only for inputs which are classified by the *classifier* neural network as normal. Thus, the *classifier* neural network is trained using the whole sets of inputs, while the *calculator* neural network is trained using only normal sets of inputs.

The *classifier* and *calculator* neural networks are both constructed using the MATLAB Neural Network Toolbox. As shown in Figure 5.1(a), the input vector is six-dimensional

consisting of the six input variables, while the output is a value ranging from 0 to 1. The value 0 represents abnormal while the value 1 represents normal. The hidden layer between the input and the output consists of 10 neurons, which has been proven enough for our applications. The symbol "*w*" represents weight and "*b*" represents bias. The transfer function in the hidden layer is the sigmoid function while the transfer function in the output layer is the softmax function. Figure 5.1(b) shows the schematic of the *calculator* artificial neural network. Similar to Figure 5.1(a), the input vector is six-dimensional consisting of the six input variables, while the output vector is two-dimensional consisting of specific energy and specific power. The hidden layer between the input and the output consists of 10 neurons with the sigmoid transfer function. The output layer has a linear transfer function. The training data for this neural network come from the FEM simulation results classified as normal by the *classifier* neural network.

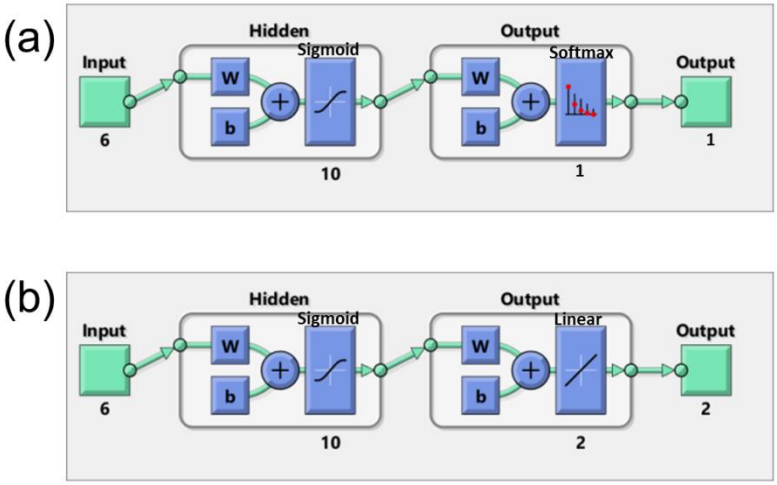

Figure 5.1. (a) Schematic of the *classifier* neural network. (b) Schematic of the *calculator* neural network.

With the trained neural networks, we performed 10000 sets of Monte Carlo simulations, which are computationally prohibitive for the finite element method. These simulations provide the global sensitivity of each input on the output. The details can be found in section 3.3. The sensitivity analysis results help to narrow down the battery design space by eliminating the

insensitive design variables. In the refined design space, the neural networks generate a design map relating sensitive design variables with specific energy and specific power. The details of battery performance optimization can be found in Section 5.3.4.

5.3 Results and Discussion

5.3.1 Classifier Neural Network

Figure 5.2(a) shows the specific energy and specific power obtained from FEM simulations of the electrochemical-thermal model with the 900 sets of input variables. Each dot represents a set of input variables, and the color illustrates the C-rate. What stands out in Figure 5.2(a) is that tens of simulations deliver negligible specific energy. Closer investigation reveals that those simulations abruptly terminate when the electrolyte concentration in the positive electrode drops below than 1 mol m^{-3}. This is understandable because electrolyte concentration cannot further decrease to negative during the simulation of discharge. The depletion of electrolyte brings physical implications. The dry up of electrolyte can lead to the loss of electrochemical activity in local regions, which may further grow because of the particle interaction effect [100]. Consequently, we are interested in avoiding input variables that may result in the depletion of electrolyte. In the following text, the simulation that results in very low electrolyte concentration (<10 mol m^{-3}) at the final instant is termed as abnormal. Figure 5.2(b) shows the classified normal and abnormal simulations. Note that some abnormal simulations may still give considerable specific energy, as those simulations proceed to discharge until reaching a very low final electrolyte concentration.

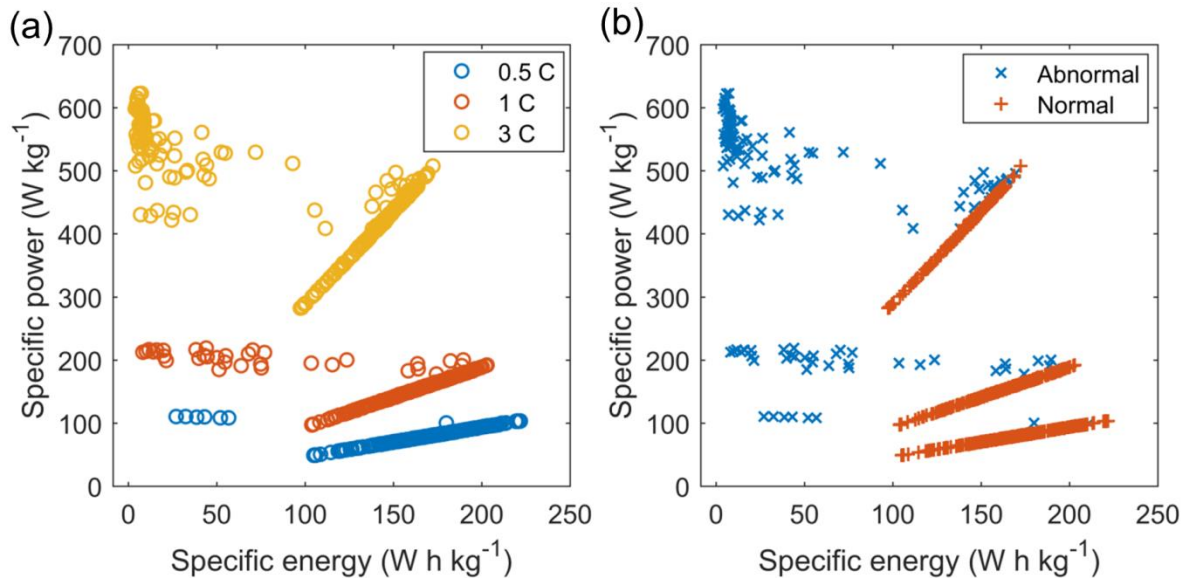

Figure 5.2. Specific power with respect to specific energy from finite element simulations of the electrochemical-thermal model. (a) The color of the dot represents the applied C-rate. (b) The color and symbol represents the normal or abnormal simulations.

Then we look at using the *classifier* neural network to predict abnormal simulations, which can be regarded as a typical classifier problem in machine learning. The abnormal cases in Figure 5.2(a) are tagged as Class 0, while the remaining normal cases are tagged as Class 1. The 900 sets of input variables and their resulting classes are used to train a neural network-based classifier. The confusion matrix in Figure 5.3(a) visualizes the performance of this neural network. The target class represents the actual class, while the output class represents the class predicted by the neural network. Of the 900 cases, the neural network correctly predicts 760 cases of Class 1 (among 764 cases) and 132 cases of Class 0 (among 136 cases). The false positive rate is 2.9% and the false negative rate is 0.5%. The accuracy of each target class and output class can be found in the gray grid. Overall, the accuracy of the trained neural network is (760+132)/900 = 99.1% as shown in the blue grid.

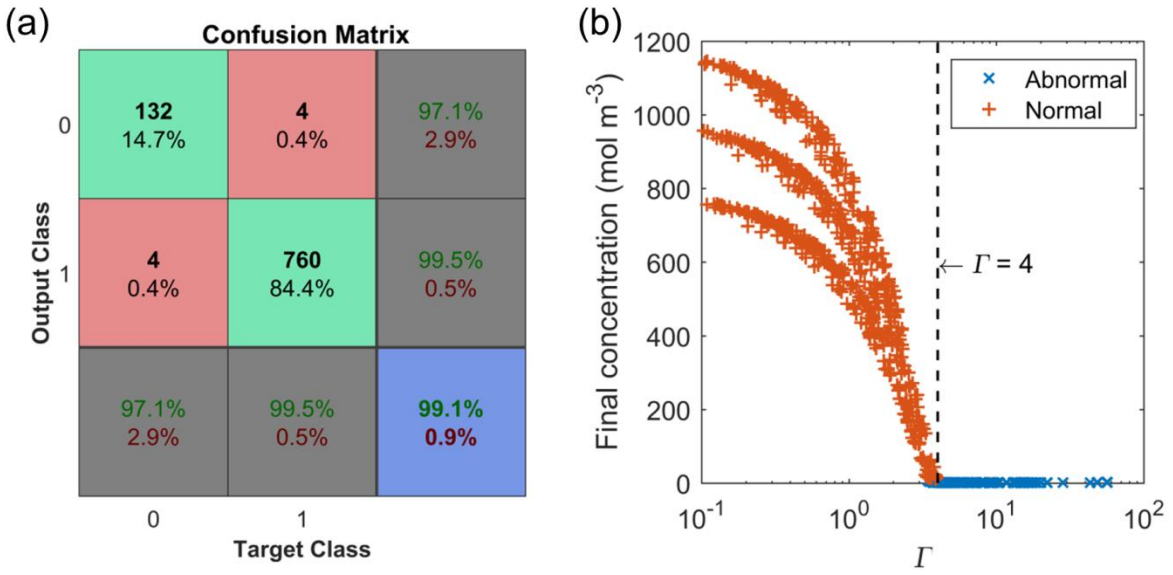

Figure 5.3. (a) Confusion matrix of neural network-based classifier. (b) Relation between Γ and the minimum electrolyte concentration of positive electrode at the end of discharge.

The results from the *classifier* neural network motivate us to think whether there exists a physical characteristic number to separate the normal and abnormal cases. Physically, the electrolyte lithium concentration in the positive electrode decreases due to the intercalation of lithium ions into positive electrode active particles. Meanwhile, lithium ions diffuse across the separator to replenish the consumed lithium ions. Thus, a non-dimensional characteristic number can be used to compare the two effects,

$$\Gamma = \frac{i_{app}/F}{D_e^{eff} c_0 / L} = \frac{i_{app} L}{F D_e^{eff} c_0}, \tag{5-16}$$

where i_{app}/F can be regarded as the lithium consumption rate required by the applied current and $D_e^{eff} c_0 / L$ can be regarded as the electrolyte supply rate due to diffusion. As shown in Figure 5.3(b), $\Gamma = 4$ serves as a satisfying threshold to determine whether a simulation is abnormal or normal. The input variables yielding $\Gamma > 4$ generally result in very low final electrolyte concentration, and thus abnormal simulations. This is a rather remarkable outcome as Γ can be calculated without running the computationally expensive simulation.

In order to further evaluate the performance of the characteristic number and the neural network, we conducted 11 more simulations. Note that the 11 simulations are not included in the previous 900 simulations. In Figure 5.4(a), the threshold of $\Gamma = 4$ successfully separates the normal and abnormal cases. The prediction from the neural network is a value ranging from 0 to 1, while the value of 0.5 can be used as the threshold in Figure 5.4(b). The results in Figure 5.4 show that both the characteristic number and the neural network work well in telling whether a simulation is normal or abnormal. It is interesting to further compare the two approaches. First, we note that Γ calculated in Eq. (5-16) can only represent the initial state. However, significant temperature increase in cold environment leads to salient change in electrolyte diffusivity, making Γ not representative of the whole discharging course. This thermal effect may diminish the usefulness of Γ. Second, although this work only considers the depletion of electrolyte as the sole reason for abnormal simulations, other factors may become important under different ranges of inputs. For example, the slow solid diffusion may lead to over-lithiation or over-delithiation for large particles with low diffusivity. In this regard, various characteristic numbers should be proposed to describe the different limiting processes. In contrast, the neural network approach provides a unified framework to classify the abnormal simulations.

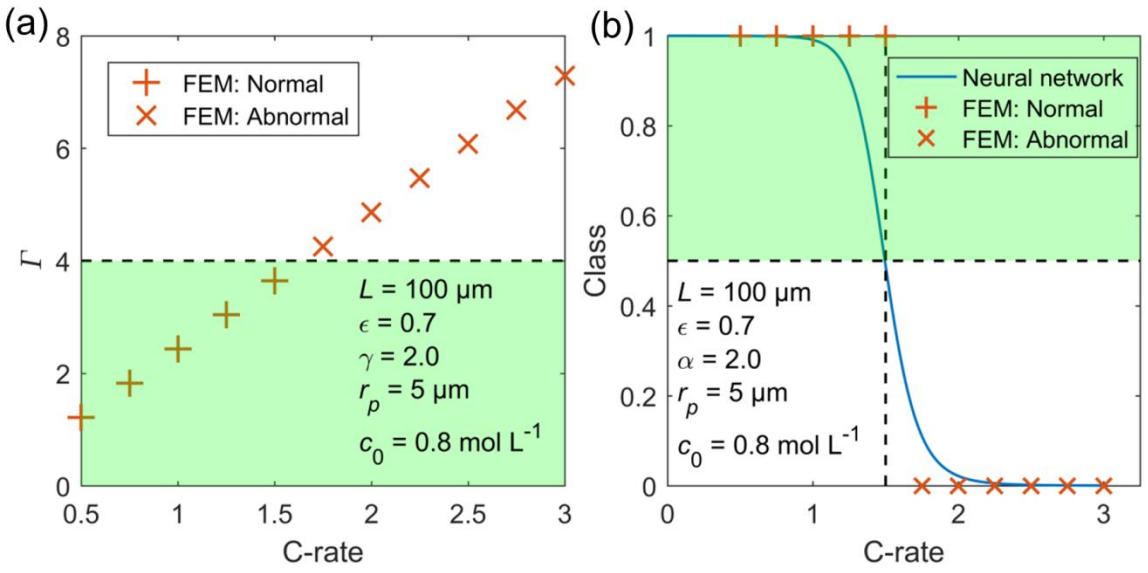

Figure 5.4. Comparison between electrochemical-thermal simulations based on the finite element method (FEM) and (a) non-dimensional characteristic number, (b) neural network-based classifier. The green region denotes the normal area. Five of the design variables are kept constant as shown in the figure, while the C-rate changes from 0.5 C to 3 C.

5.3.2 Calculator Neural Network

This section is focused on the calculation of specific energy and specific power using the neural network. The construction of the *calculator* neural network can be found in section 5.2.4.

To validate the constructed neural network, we compare the Ragone plots from the neural network and finite element simulations. Providing the relation between specific energy and specific power, Ragone plot has been widely used to characterize the performance of energy storage devices [101, 102]. As shown in Figure 5.5, the Ragone plots from the neural network agree well with the finite element simulations, meanwhile the computational cost is greatly reduced. Note that the input variables for this validation are out of the training dataset. Each FEM dot in Figure 5.5 takes about 6 minutes of computation, thus the FEM simulations can only be performed at several discrete C-rates due to the computational cost. The orange dots in Figure 5.5 take a total of 3 hours of computation. In contrast, it takes less than 1 second for the *calculator* neural network to generate the entire continuous curve. This dramatic acceleration of

calculation by several orders of magnitude highlights the great value of neural network in battery design applications.

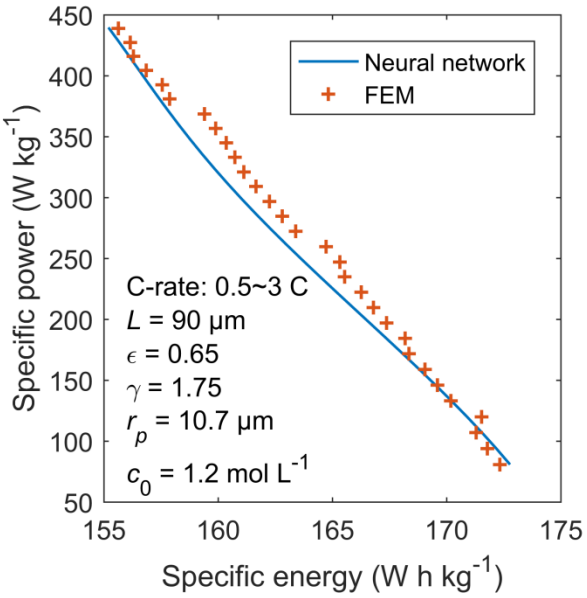

Figure 5.5. Ragone plots from neural network calculations and electrochemical-thermal simulations based on the finite element method (FEM). Each FEM dot represents a finite element simulation. Five of the design variables are kept constant as shown in the figure, while the C-rate changes from 0.5 C to 3 C.

5.3.3 Global Sensitivity Analysis

Given a generic model $Y = f(X_1, X_2, \cdots X_k)$, sensitivity analysis provides a systematic approach to quantify the influence of input X_i on the output Y. Two main categories of sensitivity analysis have been proposed in the literature. The local sensitivity analysis is based on the derivative $\partial Y / \partial X_i$. Although having the attraction of being computationally efficient, this approach can only provide information at specific points where the derivative is calculated. Thus, the derivative-based local sensitive analysis is unwarranted when the model inputs are highly uncertain or when the model is non-linear in nature. In contrast, global sensitivity analysis can provide comprehensive information over the whole input range even when the model is

nonlinear [103]. Based on the variation decomposition principle [103, 104], the first order global sensitivity is defined as

$$S_i = \frac{V[E(Y \mid X_i)]}{V(Y)}, \tag{5-17}$$

where $E(Y \mid X_i)$ is the conditional expectation over each X_i, and $V(\cdot)$ stands for variance. Intuitively, $E(Y \mid X_i)$ can be calculated by cutting the input domain into X_i slices and averaging Y over each slice. If this conditional expectation has a large variation across X_i, then this factor is regarded as important. The first order sensitivity essentially represents the fraction of output variance that can be explained by considering the input X_i alone [105]. Notably, global sensitivity analysis can also be used to explore the possible interaction effect among inputs. More details can be found in Ref. [106].

Figure 5.6 shows the first order sensitivity of the six input variables on specific energy and specific power. The electrode thickness and porosity are the dominant factors affecting specific energy. In contrast, the applied current density is the decisive factor on specific power. The salient effect of C-rate on specific power can also be found in Figure 5.2. Another observation from Figure 5.6 is that the initial electrolyte concentration, the Bruggeman constant and the particle radius have minor influence on both specific energy and specific power. Thus, we keep these factors as constant in the following optimization section.

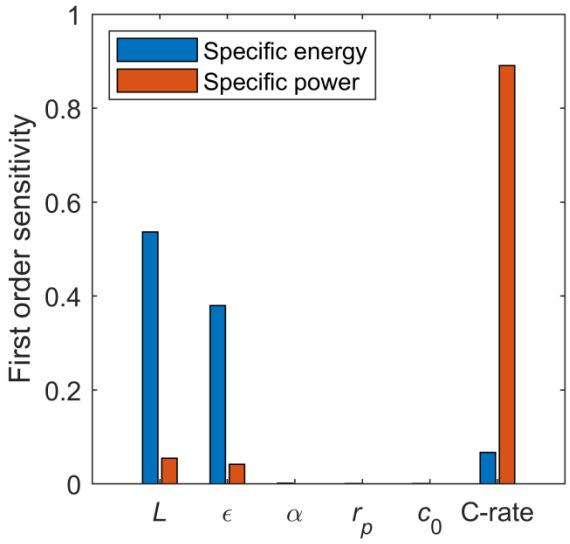

Figure 5.6. First order sensitivity of the six input variables on specific energy and specific power.

5.3.4 Optimization

Another application of the constructed neural networks is to optimize the battery design. As the initial electrolyte concentration, the Bruggeman constant and the particle radius have negligible influence on specific energy and specific power, we focus on the optimization of the electrode thickness and the solid volume fraction in this section.

As the practical application often requires a specific current density instead of C-rate, we prescribe a constant current density of 60 A m^{-2} in the optimization. The C-rate can be calculated from the applied current density using Eq. (5-10).

The first step is to distinguish the infeasible design regions, where the simulations may be abnormal. Using the *classifier* neural network developed in 5.3.1, the input is judged as infeasible when the predicted class value is lower than 0.5. As a result, the infeasible region is shown black in Figure 5.7.

Using the *calculator* neural network, the specific energy and specific power with respect to the electrode thickness and the solid volume fraction are shown in Figure 5.7. Thick electrode

and high volume fraction of active materials lead to high specific energy at the cost of low specific power. These results coincide with current battery design principles: the energy-type batteries (used for high-energy applications, such as pure electric vehicles) usually have thick and dense electrodes, while the power-type batteries (used for high-power applications, such as hybrid electric vehicles) are associated with thin and porous electrodes. The contours of Figure 5.7(a) and (b) can be combined to fulfill both requirements of specific energy and specific power. As shown in Figure 5.7(c), the green area denotes the feasible region where the specific energy is larger than 160 W h kg^{-1} and the specific power is larger than 300 W kg^{-1}.

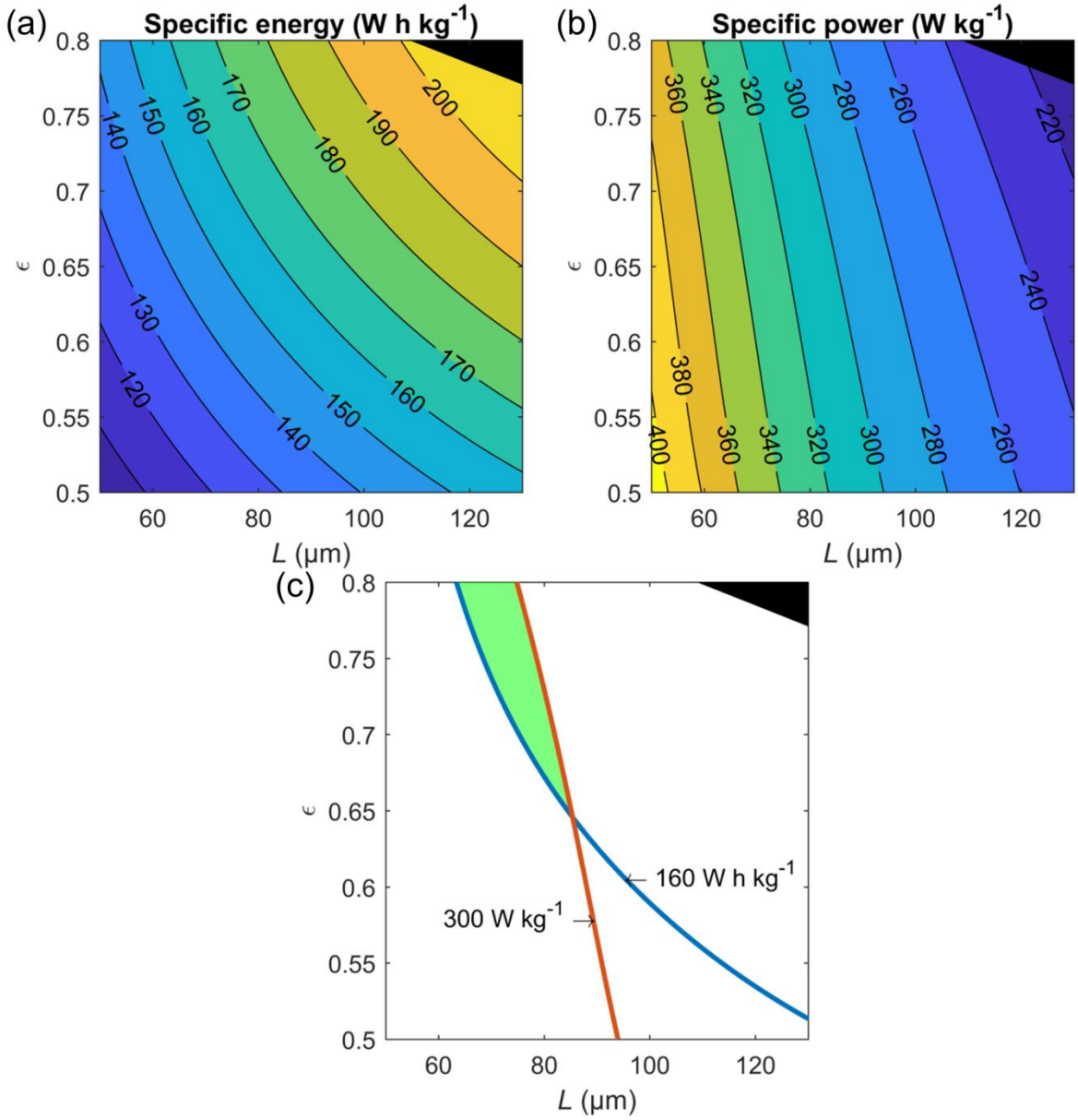

Figure 5.7. Design map generated with neural network. (a) Specific energy contour with respect to the positive electrode thickness and the positive electrode solid volume fraction. (b) Specific power contour with respect to the positive electrode thickness and the positive electrode solid volume fraction. (c) Application of the contours to determine the design area. The green region denotes the feasible region satisfying both requirements of specific energy and specific power. In all figures, the black region denotes the infeasible region where the Class predicted by the *classifier* neural network is less than 0.5. Other inputs to the neural network are $i_{app} = 60\ \mathrm{A\,m^{-2}}$, $\alpha = 1.5$, $r_p = 5\ \mu\mathrm{m}$, $c_0 = 1\ \mathrm{mol\,L^{-1}}$.

5.4 Conclusions

The high computational cost of coupled electrochemical-thermal model has prevented its utilization in the simulation-based battery design. In this work, we demonstrated that neural networks are highly valuable for battery design, which reduce the computational burden by several orders of magnitude. Two neural networks have been constructed, trained and validated using the data from finite element simulations. The first neural network, the *classifier*, was used to predict whether a set of input variables is physically feasible. The second neural network, the *calculator*, was used to calculate specific energy and specific power. Comparison between the neural networks and finite element simulations demonstrated that both the two neural networks achieved satisfying accuracy.

Using the neural networks, many computationally expensive analyses can be performed with negligible computational cost. As an example, a continuous Ragone plot was generated, which was in good agreement with the discrete Ragone plot from finite element simulations. Moreover, we performed global sensitivity analysis to rank the sensitivity of input variables on specific energy and specific power. We found that the applied C-rate is the dominant factor affecting specific power, while the electrode thickness and porosity are most significant input variables for specific energy. Based on the finding, we obtained contours that characterize the specific energy and specific power with respect to the most important variables. Finally, a design map was generated to fulfill the requirements of both specific energy and specific power. With high computational efficiency, the developed neural networks can potentially be extended to other battery applications such as advanced battery management systems for real time control.

Chapter 6 Conclusions and Future Work

This dissertation is focused on the mechanical and electrochemical modeling of lithium-ion batteries ranging from particle scale to electrode scale. The developed mathematical models are further used to optimize the design of active particles and electrodes.

Many electrode materials for lithium-ion battery applications are composed of secondary particles. Such an active material particle is not a solid particle, but consists of many fine primary particles. Chapter 2 presents a coupled mechanical and electrochemical model to predict the intercalation-induced stress in a secondary particle with an agglomerate structure. In this model the electrochemical and transport processes are accounted for at both the secondary and primary particle levels. For mechanical analysis the secondary particle is treated as a continuum with stress calculated through lithium concentration and elastic deformation. With this model we revealed several important factors that affect stresses in secondary particles. Our simulations show that a stronger dependence of the open circuit potential of the active material on lithium-ion concentration reduces the stress level. A larger magnitude of over-potential at the surface of a secondary particle causes larger stresses. A larger primary particle size helps to reduce the stresses in the secondary particle as long as the secondary particle is a continuum containing many primary particles. Finally, a comparison between a porous secondary particle and a solid particle of the same size shows that the stress level in a porous secondary particle is much smaller.

Active particles with a core–shell structure exhibit superior physical, electrochemical, and mechanical properties over their single-component counterparts in lithium-ion battery electrodes. Modeling plays an important role in providing insights into the design and utilization of this structure. In Chapter 3, a physically rigorous model is developed to describe the diffusion and stress inside the core–shell structure based on a generalized chemical potential. Including both chemical and mechanical effects, the generalized chemical potential governs the diffusion in both the shell and the core. The stress is calculated using the lithium concentration profile. Simulations reveal that a lithium concentration jump forming at the core–shell interface, which is only possible to capture by modeling the shell as electrochemically active. In sharp contrast to a single-component particle, a tensile radial stress develops at the core–shell interface during delithiation, while a tensile tangential stress develops in the shell during lithiation. The core–shell interface is prone to debonding for particles with a thick shell, while shell fracture is more likely to occur for particles with a large core and a relatively thin shell. A design map of the core and shell sizes is shown by considering both shell fracture and shell debonding.

As an inherent multiscale structure, a continuum scale battery electrode is composed of many microscale particles. Currently it is generally assumed that each particle is isolated while the stress in a particle only affects solid diffusion. The lack of mechanical interaction between particles and effect of stress on the electrochemical reaction rate makes mechanics and electrochemistry uncoupled at the continuum scale: an applied continuum scale stress in the electrode has no effect on the spatial distribution of electrochemical reaction in the electrode and vice versa. Chapter 4 first presents a multiscale model that couples mechanics and electrochemistry consistently at the microscopic and continuum scales. The microscopic particle stress is a superposition of the intra-particle concentration gradient-induced stress and the

particle interaction stress, with the latter being related to the continuum scale stress through a representative volume element. The electrochemical charge transfer kinetics is generalized with the stress effect. Diffusion in a particle is described by a chemical potential that includes stress and phase transition. In a parallel effort, we develop a direct three-dimensional particle network model, which consists of realistic active material particles. Unlike the multiscale model, there is no scale separation and homogenization in the particle network model: all particles are modeled explicitly with fully coupled three-dimensional mechanical-electrochemical equations and the finite element method. The results from the particle network model are accurate and can serve as a standard, but the size of particle network that can be calculated is limited due to high computational cost. Comparison of results from the multiscale model and from the particle network model shows that the multiscale model gives good, satisfying accuracy while reducing the computational cost dramatically in comparison to the three-dimensional particle network model. The multiscale model is a power tool to address various coupled problems in the electrode, from inter-particle crack growth to electrode structure design for high performance and long cycle life.

Simulation-based battery design encounters the difficulty of high computational cost. Chapter 5 presents a systematic approach based on the artificial neural network to reduce the computational burden of battery design by several orders-of-magnitude. Two neural networks are constructed using the finite element simulation results from a thermo-electrochemical model. The first neural network serves as a classifier to predict whether a set of input variables is physically feasible. The second neural network yields specific energy and specific power. Both neural networks are validated using extra finite element simulations out of the training data. With a global sensitivity analysis using the neural network, we quantify the effect of input variables on

specific energy and specific power by evaluating large combinations of input variables, which is computationally prohibitive for finite element simulations. Among all parameters, the applied C-rate has the largest influence on specific power, while the electrode thickness and porosity are the dominant factors affecting specific energy. Based on this finding, we generate a design map that fulfills the requirements of both specific energy and specific power. In particular, we highlight the value of neural network in handling the non-linear, complex and computationally expensive problem of battery design and optimization.

In this dissertation, the modeled active materials (e.g. $LiNi_{1/3}Co_{1/3}Mn_{1/3}O_2$ in Chapter 2 and $LiMn_2O_4$ in Chapter 4) undergo intercalation-type reactions and exhibit small elastic deformation. However, many promising active materials experience conversion-type reactions, and show very significant volume deformation. A typical example is that silicon, which has a theoretical capacity as high as 4200 Ah kg^{-1}, suffers from the 300% volume expansion during lithiation. Such large deformation induces very large stress and leads to fast fading after cycling. In such conversion-type electrode materials, mechanics plays an even more important role. The coupling of plasticity, fracture mechanics and electrochemistry is essential to understand the degradation behaviors of those materials.

Another direction extended from current research is to model the dendrite growth of lithium metal anode with consideration of mechanical stress. Previous modeling reports suggest that the usage of stiff solid electrolyte can prevent the unstable dendrite growth through the mechanical effect. The lithium metal is soft and easy to yield, thus the effects of plasticity must be carefully considered.

Appendices

Appendix A. Solid Diffusion with Mechanical Stress

In this work, we follow the modeling framework of [107] to consider the coupled stress and diffusion in solids. The solid is assumed to consist of a lattice network, which undergoes mechanical deformation and stress. Three species (lithium, host material and vacancy) occupy the lattice sites, and their total number is conserved. The host material, i.e. Mn_2O_4 in this work, is considered immobile, while the lithium and vacancy can exchange lattice sites with each other. The lithium diffusion process is in nature a process that lithium gradually occupies the vacancy sites, i.e. $\mathbf{N}_{\mathrm{Li}-\Theta}+\mathbf{N}_{\Theta}=\mathbf{0}$, where $\mathbf{N}_{\mathrm{Li}-\Theta}$ is the lithium flux and $\mathbf{N}_{\Theta}$ is the vacancy flux. Here we use the subscript 'Θ' to denote vacancy and the substrate '$\mathrm{Li}-\Theta$' to denote lithium ion while highlighting the existence of vacancy.

As the lithiation induced volume change in $LiMn_2O_4$ is small, we consider the deformation as infinitesimal. Thus, the solid lithium concentration described using the Lagrangian coordinate system is the same as that using the Euler coordinate system. The convective lithium flux in solid due to lattice expansion is also assumed as zero (see Eq. (18) in [107]).

The lithium diffusional flux is governed by the gradient of chemical potential,

$$\mathbf{N}_{\mathrm{Li}-\Theta}=-\mathbf{N}_{\Theta}=-L\nabla\left(\mu_{\mathrm{Li}-\Theta}-\mu_{\Theta}\right), \tag{A1}$$

where the coefficient L can be determined using the Stefan-Maxwell equation. After some algebraic manipulations, the flux is given by [107]

$$\mathbf{N}_{\mathrm{Li}-\Theta} = -\frac{D_0}{RT} c_{s,max} \left(\frac{c_s}{c_{s,max}} \right) \left(1 - \frac{c_s}{c_{s,max}} \right) \nabla \left(\mu_{\mathrm{Li}-\Theta} - \mu_{\Theta} \right). \tag{A2}$$

The chemical potential is given by

$$\begin{aligned} \mu_{\mathrm{Li}\text{-}\Theta} &= \mu^0_{\mathrm{Li}\text{-}\Theta} + RT \ln a_{\mathrm{Li}\text{-}\Theta} - \Omega_{\mathrm{Li}\text{-}\Theta} \sigma_h, \\ \mu_{\Theta} &= \mu^0_{\Theta} + RT \ln a_{\Theta} - \Omega_{\Theta} \sigma_h, \end{aligned} \tag{A3}$$

where μ_i^0 represents the standard state chemical potential of phase i, a_i is the activity of phase i, Ω_i is the partial molar volume of phase i and σ_h is the hydrostatic stress experienced by the lattice network. The chemical potential of lithium in active particles used in Eq. (4-11), μ, is rigorously defined as

$$\mu = \mu_{\mathrm{Li}-\Theta} - \mu_{\Theta}. \tag{A4}$$

Thus,

$$\nabla \mu = \nabla \left(\mu_{\mathrm{Li}-\Theta} - \mu_{\Theta} \right) = RT \nabla \left(\ln a_{\mathrm{Li}\text{-}\Theta} - \ln a_{\Theta} \right) - \Omega \nabla \sigma_h, \tag{A5}$$

where $\Omega = \Omega_{\mathrm{Li}\text{-}\Theta} - \Omega_{\Theta}$ is the partial molar volume of lithium in the solid.

The activity can be related to the measured open circuit potential, E_{ref}. E_{ref} is usually measured as the open circuit potential of a $LiMn_2O_4$-Li half-cell under equilibrium conditions, where the solid lithium concentration and electrolyte lithium concentration are both uniform, and there is no mechanical stress. The overall reaction of the half-cell is

$$\mathrm{Li}\text{-}\Theta \leftrightarrow \mathrm{Li} + \Theta. \tag{A6}$$

Thus, E_{ref} can be obtained by the Nernst equation as

$$E_{ref} = E^0_{ref} + \frac{RT}{F} \ln \left(\frac{a_{\Theta}}{a_{\mathrm{Li}\text{-}\Theta}} \right), \tag{A7}$$

where $E_{ref}^{0} = \left(\mu_{\mathrm{Li}}^{0} + \mu_{\Theta}^{0} - \mu_{\mathrm{Li\text{-}}\Theta}^{0}\right)/F$ and μ_{Li}^{0} is the chemical potential of pure lithium metal. E_{ref}^{0} is constant because μ_{Li}^{0}, μ_{Θ}^{0} and $\mu_{\mathrm{Li\text{-}}\Theta}^{0}$ are all constant. Thus,

$$RT\nabla\left(\ln a_{\mathrm{Li\text{-}}\Theta} - \ln a_{\Theta}\right) = -F\nabla E_{ref} = \frac{-FK}{c_{s,max}}\nabla c_s, \tag{A8}$$

where $K = \partial E_{ref}/\partial x_{Li}$. Combining Eqs. (A2) (A5) and (A8), we have

$$\mathbf{N}_{\mathrm{Li}-\Theta} = \frac{D_0}{RT}\left(\frac{c_s}{c_{s,max}}\right)\left(1-\frac{c_s}{c_{s,max}}\right)\left(FK\nabla c_s + \Omega c_{s,max}\nabla\sigma_h\right). \tag{A9}$$

This equation is the same as Eq. (4-17) or Eq. (4-39), where $\mathbf{N}_s$ is $\mathbf{N}_{\mathrm{Li}-\Theta}$.

Appendix B. Charge Transfer Kinetics with Mechanical Stress

The lithium intercalation or deintercalation reaction can be written as

$$\text{Li-}\Theta \leftrightarrow \text{Li}^+ + \text{e}^- + \Theta \tag{B1}$$

where Li^+ represents the lithium ion in the electrolyte, e^- represents the electron, Θ represents the intercalation site in the electrode solid, and $\text{Li-}\Theta$ represents the lithium in the electrode solid.

The forward and backward reaction rates, $r_{\rightarrow}$ and $r_{\leftarrow}$, are given by the transition state theory,

$$\begin{aligned} r_{\rightarrow} &= r_0 \exp\left(-\frac{\mu_{TS} - \mu_{\text{Li-}\Theta}}{RT}\right), \\ r_{\leftarrow} &= r_0 \exp\left(-\frac{\mu_{TS} - (\mu_{\text{Li}^+} + \mu_{\text{e}^-} + \mu_{\Theta})}{RT}\right). \end{aligned} \tag{B2}$$

Here r_0 is a rate constant, μ_i represents the chemical potential of phase i and 'TS' stands for the transition state. The expressions of the reactant chemical potentials can be written as

$$\begin{aligned} \mu_{\text{Li-}\Theta} &= \mu^0_{\text{Li-}\Theta} + RT \ln a_{\text{Li-}\Theta}, \\ \mu_{\Theta} &= \mu^0_{\Theta} + RT \ln a_{\Theta}, \\ \mu_{\text{Li}^+} &= \mu^0_{\text{Li}^+} + RT \ln a_{\text{Li}^+} + F\phi_e, \\ \mu_{\text{e}^-} &= -F\phi_s, \end{aligned} \tag{B3}$$

where a_i is the activity of phase i, ϕ_e is the electric potential of electrolyte near the interface, and ϕ_s is the electric potential of solid near the interface. Note that ϕ_e and ϕ_s should be defined with respect to the same reference point, say the current collector of the negative electrode. If so,

ϕ_s is equivalent to Φ_s used in Eq. (4-22) while ϕ_e is different from Φ_e but their relation will be given later. The transition state chemical potential is given by

$$\mu_{TS} = \mu_{TS}^0 + (1-\beta)F(\phi_e - \phi_s), \tag{B4}$$

where β is the cathodic symmetry factor, which represents the fraction of applied potential in promoting the cathodic reaction, i.e. the backward reaction in Eq. (B2).

With Eqs. (B3) and (B4), the forward and backward reaction rates are given by

$$\begin{aligned} r_{\rightarrow} &= r_0 \exp\left(-\frac{\mu_{TS}^0 - \mu_{\text{Li-}\Theta}^0}{RT}\right) a_{\text{Li-}\Theta} \exp\left(-\frac{(1-\beta)F(\phi_e - \phi_s)}{RT}\right), \\ r_{\leftarrow} &= r_0 \exp\left(-\frac{\mu_{TS}^0 - \mu_{\Theta}^0 - \mu_{\text{Li}^+}^0}{RT}\right) a_{\text{Li}^+} a_{\Theta} \exp\left(\frac{\beta F(\phi_e - \phi_s)}{RT}\right). \end{aligned} \tag{B5}$$

The anodic and cathodic reaction rate constants are defined as

$$k_a = r_0 \exp\left(-\frac{\mu_{TS}^0 - \mu_{\text{Li-}\Theta}^0}{RT}\right), k_c = r_0 \exp\left(-\frac{\mu_{TS}^0 - \mu_{\Theta}^0 - \mu_{\text{Li}^+}^0}{RT}\right). \tag{B6}$$

Then, the net reaction rate is

$$\begin{aligned} r &= r_{\rightarrow} - r_{\leftarrow} \\ &= k_a a_{\text{Li-}\Theta} \exp\left(\frac{(1-\beta)F(\phi_s - \phi_e)}{RT}\right) - k_c a_{\text{Li}^+} a_{\Theta} \exp\left(-\frac{\beta F(\phi_s - \phi_e)}{RT}\right). \end{aligned} \tag{B7}$$

A typical method to simplify Eq. (B7) is to introduce the equilibrium potential,

$$\left(\phi_s - \phi_e\right)_{\text{eq}} = U = \frac{RT}{F}\ln\left(\frac{k_c}{k_a}\right) + \frac{RT}{F}\ln\left(\frac{a_{\text{Li}^+} a_{\Theta}}{a_{\text{Li-}\Theta}}\right), \tag{B8}$$

which results in zero net reaction rate. This gives

$$U = \frac{\mu_{\Theta} + \mu_{\text{Li}^+}^0 + RT\ln a_{\text{Li}^+} - \mu_{\text{Li-}\Theta}}{F}. \tag{B9}$$

Note that U depends on both the electrolyte lithium concentration and the solid lithium concentration, which differs from the E_{ref} in Eq. (4-22), which only depends on the solid lithium concentration.

The overpotential is defined as

$$\eta = \phi_s - \phi_e - U. \tag{B10}$$

Then, the charge transfer current can be given as

$$i = rF = i_0 \left[\exp\left(\frac{(1-\beta)F\eta}{RT} \right) - \exp\left(-\frac{\beta F\eta}{RT} \right) \right], \tag{B11}$$

where the exchange current density is given by

$$i_0 = F\left(k_a a_{\text{Li-}\Theta}\right)^{\beta} \left(k_c a_{\text{Li}^+} a_{\Theta}\right)^{1-\beta}. \tag{B12}$$

Next, we should establish a relation between ϕ_e and Φ_e, and another relation between U and E_{ref}. At the point of interest that has a "real" electrolyte potential of ϕ_e, we put a lithium metal reference electrode, and measure the potential difference between this reference electrode with respect to the chosen fixed point. The measurement potential under equilibrium is Φ_e. The reaction at this reference electrode is given as

$$\text{Li} \leftrightarrow \text{Li}^+ + \text{e}^-. \tag{B13}$$

The equilibrium condition of reaction gives

$$\mu_{\text{Li}}^0 = \mu_{\text{Li}^+}^0 + RT \ln a_{\text{Li}^+} + F\phi_e - F\Phi_e, \tag{B14}$$

where μ_{Li}^0 is the chemical potential of pure lithium metal. Thus,

$$\Phi_e = \phi_e + \frac{\mu_{\text{Li}^+}^0 + RT \ln a_{\text{Li}^+} - \mu_{\text{Li}}^0}{F}. \tag{B15}$$

E_{ref} is usually measured as the open circuit potential of a half-cell under equilibrium conditions with lithium metal as the negative electrode, where the solid lithium concentration and electrolyte lithium concentration are both uniform. The overall reaction of the half-cell is

$$\mathrm{Li}-\Theta \leftrightarrow \mathrm{Li}^{+}+\Theta. \tag{B16}$$

Thus, E_{ref} can be given by the Nernst equation as

$$E_{ref}=\frac{\mu_{\mathrm{Li}}^{0}+\mu_{\Theta}-\mu_{\mathrm{Li}\text{-}\Theta}}{F}. \tag{B17}$$

Note that no electrolyte lithium concentration appears in Eq. (B17). Combining Eqs. (B9), (B15) and (B17), the over- potential in Eq. (B10) can be re-written as

$$\eta=\Phi_s-\Phi_e-E_{ref}, \tag{B18}$$

which is what used in this work.

Now, we consider the influence of mechanical stress on the charge transfer kinetics. The mechanical stress has no effect on the chemical potential of electrolyte lithium ions and electrons, but adds additional terms in $\mu_{\mathrm{Li}\text{-}\Theta}$ and μ_{Θ},

$$\begin{aligned}\mu_{\mathrm{Li}\text{-}\Theta}&=\mu_{\mathrm{Li}\text{-}\Theta}^{0}+RT\ln a_{\mathrm{Li}\text{-}\Theta}-\Omega_{\mathrm{Li}\text{-}\Theta}\sigma_h,\\ \mu_{\Theta}&=\mu_{\Theta}^{0}+RT\ln a_{\Theta}-\Omega_{\Theta}\sigma_h,\end{aligned} \tag{B19}$$

where Ω_i is the partial molar volume of phase i and σ_h is the hydrostatic stress.

The transition state energy is given by

$$\mu_{TS}=\mu_{TS}^{0}+(1-\beta)F(\phi_e-\phi_s)+\beta_m(-\Omega_{\mathrm{Li}\text{-}\Theta}\sigma_h)+(1-\beta_m)(-\Omega_{\Theta}\sigma_h), \tag{B20}$$

where β_m is the mechanically cathodic symmetry factor. The forward and backward reaction rates are then given by

$$
\begin{aligned}
r_{\rightarrow} &= r_0 \exp\left(-\frac{\mu_{TS}^0 - \mu_{\text{Li-}\Theta}^0}{RT}\right) a_{\text{Li-}\Theta} \exp\left(-\frac{(1-\beta)F(\phi_e - \phi_s)}{RT}\right) \exp\left(-\frac{(1-\beta_m)\Omega\sigma_h}{RT}\right), \\
r_{\leftarrow} &= r_0 \exp\left(-\frac{\mu_{TS}^0 - \mu_{\Theta}^0 - \mu_{\text{Li}^+}^0}{RT}\right) a_{\text{Li}^+} a_{\Theta} \exp\left(\frac{\beta F(\phi_e - \phi_s)}{RT}\right) \exp\left(\frac{\beta_m \Omega\sigma_h}{RT}\right),
\end{aligned}
\tag{B21}
$$

where $\Omega = \Omega_{\text{Li-}\Theta} - \Omega_{\Theta}$ is the partial molar volume of lithium in the solid.

Thus, the net reaction rate is

$$
\begin{aligned}
r &= r_{\rightarrow} - r_{\leftarrow} \\
&= k_a a_{\text{Li-}\Theta} \exp\left(\frac{(1-\beta)F(\phi_s - \phi_e)}{RT} - \frac{(1-\beta_m)\Omega\sigma_h}{RT}\right) - k_c a_{\text{Li}^+} a_{\Theta} \exp\left(-\frac{\beta F(\phi_s - \phi_e)}{RT} + \frac{\beta_m \Omega\sigma_h}{RT}\right),
\end{aligned}
\tag{B22}
$$

Similarly, we introduce the equilibrium potential with the influence of mechanical stress as

$$
(\phi_s - \phi_e)_{\text{eq}} = U_m = \frac{RT}{F}\ln\left(\frac{k_c}{k_a}\right) + \frac{RT}{F}\ln\left(\frac{a_{\text{Li}^+} a_{\Theta}}{a_{\text{Li-}\Theta}}\right) + \frac{\Omega\sigma_h}{F},
\tag{B23}
$$

and the revised overpotential as

$$
\eta_m = \phi_s - \phi_e - U_m,
\tag{B24}
$$

then the charge transfer current is given by

$$
i = rF = i_0 \exp\left(\frac{(\beta_m - \beta)\Omega\sigma_h}{RT}\right)\left[\exp\left(\frac{(1-\beta)F\eta_m}{RT}\right) - \exp\left(-\frac{\beta F\eta_m}{RT}\right)\right].
\tag{B25}
$$

Following the same procedure to remove the dependence of equilibrium potential on electrolyte lithium concentration, we can get

$$
\eta_m = \Phi_s - \Phi_e - E_{ref} - \frac{\Omega\sigma_h}{F}.
\tag{B26}
$$

Note that the exchange current density given by Eq. (B12) depends on activity instead of concentration. Rigorously speaking, the activity of solid phase can be derived and fitted from the

measured E_{ref} (see more in [108-111]). In this work, we utilize the common approximation in the porous electrode model to replace the activity with concentration, which gives

$$i_0 = F\left(k_a c_{\text{Li-}\Theta}\right)^{\beta}\left(k_c c_{\text{Li}^+} c_{\Theta}\right)^{1-\beta} = Fkc_{s,surf}^{\beta} c_e^{1-\beta}\left(c_{s,max} - c_{s,surf}\right)^{1-\beta} \tag{B27}$$

Appendix C. Determination of Elastic Modulus and Expansion Coefficient

As derived in [112], the homogenized elastic tensor using the asymptotic homogenization method is

$$C_{ijmn}^{H} = \frac{1}{|Y|}\int_{Y} C_{ijkl}(\mathbf{y})\left(I_{kl}^{mn} - \frac{\partial \chi_k^{mn}}{\partial y_l} \right) dY, \tag{C1}$$

where Y denotes a periodic RVE structure whose volume is denoted as $|Y|$, $\mathbf{y}$ is the coordinate system in the RVE (note that here we use y_1, y_2, y_3 instead of x, y, z to denote the components of the RVE coordinate system), $C_{ijkl}(\mathbf{y})$ is either the elastic modulus of particles or zero depending on the location $\mathbf{y}$, $I_{kl}^{mn} = \delta_{mk}\delta_{nl}$ with δ_{ij} being Kronecker delta, χ_k^{mn} is the characteristic displacement field tensor, and $dY = dy_1 dy_2 dy_3$. The asymptotic homogenization method has developed an approach to calculate χ_k^{mn}, and then the homogenized elastic modulus using Eq. (C1).

χ_k^{mn} is a third-order tensor with the symmetry of $\chi_k^{mn} = \chi_k^{nm}$, and is given by

$$\frac{\partial}{\partial y_j}\left[C_{ijkl}(\mathbf{y})\left(I_{kl}^{mn} - \frac{\partial \chi_k^{mn}}{\partial y_l} \right) \right] = 0. \tag{C2}$$

The periodic structure gives the following periodic boundary conditions

$$\begin{aligned} \chi_k^{mn}(0, y_2, y_3) &= \chi_k^{mn}(y_1^0, y_2, y_3), \\ \chi_k^{mn}(y_1, 0, y_3) &= \chi_k^{mn}(y_1, y_2^0, y_3), \\ \chi_k^{mn}(y_1, y_2, 0) &= \chi_k^{mn}(y_1, y_2, y_3^0), \end{aligned} \tag{C3}$$

where y_1^0, y_2^0, y_3^0 are the length of RVE along the y_1, y_2, y_3 axes and $y_1 \in \left[0, y_1^0\right]$, $y_2 \in \left[0, y_2^0\right]$, and $y_3 \in \left[0, y_3^0\right]$. We also need to impose a fixed constraint at one point to eliminate the singularity, which can be given as

$$\chi_k^{mn}(0,0,0) = 0. \tag{C4}$$

The calculated results for the continuum scale mechanical properties are

$$\begin{aligned} &C_{1111}^H = C_{2222}^H = C_{3333}^H = 2.43 \text{ GPa}, \\ &C_{1122}^H = C_{2211}^H = C_{1133}^H = C_{3311}^H = C_{2233}^H = C_{3322}^H = 0.374 \text{ GPa}, \\ &C_{1212}^H = C_{2323}^H = C_{1313}^H = 0.80 \text{ GPa}, \end{aligned} \tag{C5}$$

and other elastic components are zero. Using the matrix expression, the elastic modulus can be written as

$$\mathbf{C}^H = \begin{bmatrix} 2.43 & 0.374 & 0.374 & & & \\ 0.374 & 2.43 & 0.374 & & & \\ 0.374 & 0.374 & 2.43 & & & \\ & & & 0.80 & & \\ & & & & 0.80 & \\ & & & & & 0.80 \end{bmatrix} \text{GPa}. \tag{C6}$$

The calculated results show that the homogenized elastic modulus has only three independent components, $E^H = 2.33 \text{ GPa}, \nu^H = 0.13, G^H = 0.80 \text{ GPa}$. See more at [113].

If we treat the concentration in analogy as temperature, the determination of homogenized Ω^H is equivalent to the determination of homogenized thermal expansion coefficient α_{ij}^H. As given in [114], α_{ij}^H is given by

$$\alpha_{ij}^H = S_{ijpq}^H \frac{1}{|Y|} \int_Y C_{pqkl}(\mathbf{y}) \left(\alpha_{kl}(\mathbf{y}) - \frac{\partial \varphi_k}{\partial y_l} \right) dY, \tag{C7}$$

where S_{ijkl}^{H} is the homogenized compliance tensor, which is the inverse of C_{ijkl}^{H}. The thermal expansion coefficient of the particle is isotropic as $\alpha_{11}=\alpha_{22}=\alpha_{33}=\Omega, \alpha_{ij}=0 (i \neq j)$, and the thermal expansion of the pore is always 0. The characteristic displacement φ_k in Eq. (C7) is determined by

$$\frac{\partial}{\partial y_j}\left[C_{ijkl}(\mathbf{y})\left(\alpha_{kl}(\mathbf{y})-\frac{\partial \varphi_k}{\partial y_l}\right)\right]=0. \tag{C8}$$

The calculated result is $\alpha_{ij}^{H}=\alpha_{ij}$. Thus, $\Omega^{H}=\Omega$.

Bibliography

[1] H. Mendoza, S.A. Roberts, V.E. Brunini, A.M. Grillet, Electrochim Acta, 190 (2016) 1-15.
[2] S.A. Roberts, V.E. Brunini, K.N. Long, A.M. Grillet, J Electrochem Soc, 161 (2014) F3052-F3059.
[3] X. Zhang, W. Shyy, A. Marie Sastry, J Electrochem Soc, 154 (2007) A910-A916.
[4] R. Deshpande, Y.T. Cheng, M.W. Verbrugge, J Power Sources, 195 (2010) 5081-5088.
[5] R.T. Purkayastha, R.M. McMeeking, Comput Mech, 50 (2012) 209-227.
[6] R. Purkayastha, R. McMeeking, Computational Materials Science, 80 (2013) 2-14.
[7] T.K. Bhandakkar, H.J. Gao, Int J Solids Struct, 48 (2011) 2304-2309.
[8] T.K. Bhandakkar, H.J. Gao, Int J Solids Struct, 47 (2010) 1424-1434.
[9] K.J. Zhao, M. Pharr, J.J. Vlassak, Z.G. Suo, J Appl Phys, 108 (2010).
[10] K.J. Zhao, M. Pharr, Q. Wan, W.L. Wang, E. Kaxiras, J.J. Vlassak, Z.G. Suo, J Electrochem Soc, 159 (2012) A238-A243.
[11] K.J. Zhao, M. Pharr, J.J. Vlassak, Z.G. Suo, J Appl Phys, 109 (2011).
[12] Z. Jia, W.K. Liu, J Electrochem Soc, 163 (2016) A940-A946.
[13] C. Monroe, J. Newman, J Electrochem Soc, 152 (2005) A396-A404.
[14] S. Kim, S.J. Choi, K. Zhao, H. Yang, G. Gobbi, S. Zhang, J. Li, Nature Communications, 7 (2016) 10146.
[15] J. Christensen, J Electrochem Soc, 157 (2010) A366-A380.
[16] H. Wang, Y.-i. Jang, B. Huang, D.R. Sadoway, Y.-m. Chiang, J Electrochem Soc, 146 (1999) 473-480.
[17] D. Abraham, D. Dees, J. Knuth, E. Reynolds, ARGONNE National Laboratory (ANL-05/21), (2005) 196.
[18] K. Takahashi, V. Srinivasan, J Electrochem Soc, 162 (2015) A635-A645.
[19] T. Waldmann, S. Gorse, T. Samtleben, G. Schneider, V. Knoblauch, M. Wohlfahrt-Mehrens, J Electrochem Soc, 161 (2014) A1742-A1747.
[20] J. Christensen, J. Newman, J Electrochem Soc, 153 (2006) A1019-A1030.
[21] X. Zhang, W. Shyy, A. Marie Sastry, J Electrochem Soc, 154 (2007) A910-A916.
[22] B. Rieger, S.V. Erhard, K. Rumpf, A. Jossen, J Electrochem Soc, 163 (2016) A1566-A1575.
[23] Y. Dai, L. Cai, R.E. White, Journal of Power Sources, 247 (2014) 365-376.
[24] J. Park, W. Lu, A.M. Sastry, J Electrochem Soc, 158 (2011) A201-A206.
[25] S. Dargaville, T.W. Farrell, J Electrochem Soc, 157 (2010) A830-A840.
[26] J. Huang, H. Ge, Z. Li, J. Zhang, J Electrochem Soc, 161 (2014) E3202-E3215.
[27] S. Lueth, U.S. Sauter, W.G. Bessler, J Electrochem Soc, 163 (2016) A210-A222.
[28] M. Doyle, J Electrochem Soc, 140 (1993) 1526-1533.
[29] T.F.D. Fuller, Marc. Newman, John., J Electrochem Soc, 141 (1994) 1-10.

[30] J. Huang, Z. Li, J. Zhang, S. Song, Z. Lou, N. Wu, J Electrochem Soc, 162 (2015) A585-A595.
[31] A.P. Roberts, E.J. Garboczi, Journal of the American Ceramic Society, 83 (2000) 3041-3048.
[32] V. Srinivasan, J. Newman, J Electrochem Soc, 151 (2004) A1517-A1529.
[33] T.R. Tanim, C.D. Rahn, C.-Y. Wang, Journal of Dynamic Systems, Measurement, and Control, 137 (2014) 011005-011001-011005-011011.
[34] S.W. Han, "Transport and Kinetic Phenomena Linked to Power Performance of Lithium-Ion Batteries", Ph.D. dissertation, University of Michigan, 2014.
[35] X.K. Lin, J. Park, L. Liu, Y. Lee, A.M. Sastry, W. Lu, J Electrochem Soc, 160 (2013) A1701-A1710.
[36] S. Han, J. Park, W. Lu, A.M. Sastry, Journal of Power Sources, 240 (2013) 155-167.
[37] Y. Qi, L.G. Hector, C. James, K.J. Kim, J Electrochem Soc, 161 (2014) F3010-F3018.
[38] N.A. Zacharias, D.R. Nevers, C. Skelton, K. Knackstedt, D.E. Stephenson, D.R. Wheeler, J Electrochem Soc, 160 (2013) A306-A311.
[39] L. Su, Y. Jing, Z. Zhou, Nanoscale, 3 (2011) 3967-3683.
[40] Y.K. Sun, Z. Chen, H.J. Noh, D.J. Lee, H.G. Jung, Y. Ren, S. Wang, C.S. Yoon, S.T. Myung, K. Amine, Nat Mater, 11 (2012) 942-947.
[41] Y.K. Sun, S.T. Myung, M.H. Kim, J. Prakash, K. Amine, J Am Chem Soc, 127 (2005) 13411-13418.
[42] S.H. Ng, J. Wang, D. Wexler, S.Y. Chew, H.K. Liu, J Phys Chem C, 111 (2007) 11131-11138.
[43] P. Gao, J. Fu, J. Yang, R. Lv, J. Wang, Y. Nuli, X. Tang, Phys Chem Chem Phys, 11 (2009) 11101-11105.
[44] I. Laresgoiti, S. Kabitz, M. Ecker, D.U. Sauer, Journal of Power Sources, 300 (2015) 112-122.
[45] F. Hao, D.N. Fang, J Electrochem Soc, 160 (2013) A595-A600.
[46] H. Kim, J. Cho, Nano Lett, 8 (2008) 3688-3691.
[47] B. Wu, W. Lu, J Electrochem Soc, 163 (2016) A3131-A3139.
[48] Y.K. Sun, S.T. Myung, H.S. Shin, Y.C. Bae, C.S. Yoon, J Phys Chem B, 110 (2006) 6810-6815.
[49] R.D. Deshpande, D.M. Bernardi, J Electrochem Soc, 164 (2017) A461-A474.
[50] K.J. Zhao, M. Pharr, L. Hartle, J.J. Vlassak, Z.G. Suo, Journal of Power Sources, 218 (2012) 6-14.
[51] C.V. Di Leo, E. Rejovitzky, L. Anand, Int J Solids Struct, 67-68 (2015) 283-296.
[52] K. Takahashi, K. Higa, S. Mair, M. Chintapalli, N. Balsara, V. Srinivasan, J Electrochem Soc, 163 (2016) A385-A395.
[53] E. Bohn, T. Eckl, M. Kamlah, R. McMeeking, J Electrochem Soc, 160 (2013) A1638-A1652.
[54] Z.W. Cui, F. Gao, J.M. Qu, J Mech Phys Solids, 60 (2012) 1280-1295.
[55] Y.F. Gao, M. Cho, M. Zhou, J Mech Phys Solids, 61 (2013) 579-596.
[56] T.H. Wan, F. Ciucci, Continuum Level Transport and Electro-Chemo-Mechanics Coupling—Solid Oxide Fuel Cells and Lithium Ion Batteries, in: Electro-Chemo-Mechanics of Solids, 2017, pp. 161-189.
[57] K.J. Zhao, M. Pharr, S.Q. Cai, J.J. Vlassak, Z.G. Suo, J Am Ceram Soc, 94 (2011) S226-S235.

[58] M. Guo, G. Sikha, R.E. White, J Electrochem Soc, 158 (2011) A122.
[59] X.H. Xiong, D. Ding, Z.X. Wang, B. Huang, H.J. Guo, X.H. Li, J Solid State Electr, 18 (2014) 2619-2624.
[60] C. Julien, A. Mauger, K. Zaghib, H. Groult, Materials, 9 (2016) 595.
[61] J.M. Lim, T. Hwang, D. Kim, M.S. Park, K. Cho, M. Cho, Sci Rep, 7 (2017) 39669.
[62] M.S. Whittingham, Chem Rev, 104 (2004) 4271-4301.
[63] Y. Wei, J. Zheng, S. Cui, X. Song, Y. Su, W. Deng, Z. Wu, X. Wang, W. Wang, M. Rao, Y. Lin, C. Wang, K. Amine, F. Pan, J Am Chem Soc, 137 (2015) 8364-8367.
[64] H. Sun, K. Zhao, The Journal of Physical Chemistry C, 121 (2017) 6002-6010.
[65] M. Doyle, T.F. Fuller, J. Newman, J Electrochem Soc, 140 (1993) 1526-1533.
[66] J. Christensen, J. Newman, J Solid State Electr, 10 (2006) 293-319.
[67] B. Wu, W. Lu, J Phys Chem C, 121 (2017) 19022–19030.
[68] H. Liu, M. Wolf, K. Karki, Y.-S. Yu, E.A. Stach, J. Cabana, K.W. Chapman, P.J. Chupas, Nano Letters, 17 (2017) 3452-3457.
[69] R. Hill, Journal of the Mechanics and Physics of Solids, 13 (1965) 213-222.
[70] Y. Benveniste, Mechanics of Materials, 6 (1987) 147-157.
[71] T. Mori, K. Tanaka, Acta Metallurgica, 21 (1973) 571-574.
[72] A.P. Roberts, E.J. Garboczi, J Am Ceram Soc, 83 (2000) 3041-3048.
[73] K. Terada, M. Kurumatani, T. Ushida, N. Kikuchi, Comput Mech, 46 (2010) 269-285.
[74] S.S. Vel, A.J. Goupee, Comp Mater Sci, 48 (2010) 22-38.
[75] J.S. Newman, Electrochemical systems, 2nd ed., Prentice Hall, Englewood Cliffs, N.J., 1991.
[76] Y. Dai, L. Cai, R.E. White, J Power Sources, 247 (2014) 365-376.
[77] P.K. Leung, C. Moreno, I. Masters, S. Hazra, B. Conde, M.R. Mohamed, R.J. Dashwood, R. Bhagat, J Power Sources, 271 (2014) 82-86.
[78] B. Rieger, S. Schlueter, S.V. Erhard, A. Jossena, J Electrochem Soc, 163 (2016) A1595-A1606.
[79] N.S. Xue, W.B. Du, A. Gupta, W. Shyy, A.M. Sastry, J.R.R.A. Martins, J Electrochem Soc, 160 (2013) A1071-A1078.
[80] S. De, P.W.C. Northrop, V. Ramadesigan, V.R. Subramanian, Journal of Power Sources, 227 (2013) 161-170.
[81] V. Ramadesigan, R.N. Methekar, F. Latinwo, R.D. Braatz, V.R. Subramanian, J Electrochem Soc, 157 (2010) A1328-A1334.
[82] L.O. Valoen, J.N. Reimers, J Electrochem Soc, 152 (2005) A882-A891.
[83] J.B. Zhang, B. Wu, Z. Li, J. Huang, J Power Sources, 259 (2014) 106-116.
[84] J.B. Zhang, J. Huang, Z. Li, B. Wu, Z.H. Nie, Y. Sun, F.Q. An, N.N. Wu, J Therm Anal Calorim, 117 (2014) 447-461.
[85] W.B. Gu, C.Y. Wang, J Electrochem Soc, 147 (2000) 2910-2922.
[86] L. Liu, J. Park, X.K. Lin, A.M. Sastry, W. Lu, J Power Sources, 268 (2014) 482-490.
[87] B. Wu, Z. Li, J.B. Zhang, J Electrochem Soc, 162 (2015) A181-A191.
[88] D. Silver, A. Huang, C.J. Maddison, A. Guez, L. Sifre, G. van den Driessche, J. Schrittwieser, I. Antonoglou, V. Panneershelvam, M. Lanctot, S. Dieleman, D. Grewe, J. Nham, N. Kalchbrenner, I. Sutskever, T. Lillicrap, M. Leach, K. Kavukcuoglu, T. Graepel, D. Hassabis, Nature, 529 (2016) 484-489.
[89] S. Piller, M. Perrin, A. Jossen, Journal of Power Sources, 96 (2001) 113-120.
[90] T. Weigert, Q. Tian, K. Lian, Journal of Power Sources, 196 (2011) 4061-4066.

[91] T. DuBeshter, P.K. Sinha, A. Sakars, G.W. Fly, J. Jorne, J Electrochem Soc, 161 (2014) A599-A605.
[92] W.B. Du, N.S. Xue, W. Shyy, J.R.R.A. Martins, J Electrochem Soc, 161 (2014) E3086-E3096.
[93] I.V. Thorat, D.E. Stephenson, N.A. Zacharias, K. Zaghib, J.N. Harb, D.R. Wheeler, Journal of Power Sources, 188 (2009) 592-600.
[94] Y. Yamada, A. Yamada, J Electrochem Soc, 162 (2015) A2406-A2423.
[95] J. Mao, W. Tiedemann, J. Newman, Journal of Power Sources, 271 (2014) 444-454.
[96] R.H. Myers, D.C. Montgomery, C.M. Anderson-Cook, Response Surface Methodology: Process and Product Optimization Using Designed Experiments, Wiley and Sons Inc., New York, 1995.
[97] N. Yabuuchi, Y. Makimura, T. Ohzuku, J Electrochem Soc, 154 (2007) A314-A321.
[98] Y.F. Reynier, R. Yazami, B. Fultz, J Electrochem Soc, 151 (2004) A422-A426.
[99] W. Lu, I. Belharouak, D. Vissers, K. Amine, J Electrochem Soc, 153 (2006) A2147-A2151.
[100] B. Wu, W. Lu, J Power Sources, 360 (2017) 360-372.
[101] T. Christen, M.W. Carlen, Journal of Power Sources, 91 (2000) 210-216.
[102] D.V. Ragone, in: Mid-Year Meeting of the Society of Automotive Engineers, Detroit, MI, 1968.
[103] A. Saltelli, M. Ratto, T. Andres, F. Campolongo, J. Cariboni, D. Gatelli, M. Saisana, S. Tarantola, Global Sensitivity Analysis. The Primer, John Wiley & Sons, 2008.
[104] I.M. Sobol, Math Comput Simulat, 55 (2001) 271-280.
[105] W.B. Du, A. Gupta, X.C. Zhang, A.M. Sastry, W. Shyy, Int J Heat Mass Tran, 53 (2010) 3552-3561.
[106] F. Cannavo, Comput Geosci-Uk, 44 (2012) 52-59.
[107] D.R. Baker, M.W. Verbrugge, A.F. Bower, Journal of Solid State Electrochemistry, 20 (2016) 163-181.
[108] A.M. Colclasure, R.J. Kee, Electrochimica Acta, 55 (2010) 8960-8973.
[109] A. Latz, J. Zausch, Electrochimica Acta, 110 (2013) 358-362.
[110] Q. Zhang, Q.Z. Guo, R.E. White, J Electrochem Soc, 153 (2006) A301-A309.
[111] D.K. Karthikeyan, G. Sikha, R.E. White, Journal of Power Sources, 185 (2008) 1398-1407.
[112] J. Pinho-da-Cruz, J.A. Oliveira, F. Teixeira-Dias, Computational Materials Science, 45 (2009) 1073-1080.
[113] R. Penta, A. Gerisch, Comput Vis Sci, 17 (2015) 185-201.
[114] Y.M. Shabana, N. Noda, Int J Solids Struct, 45 (2008) 3494-3506.